All Theses and Dissertations (ETDs)

Spring 3-26-2014

Submicron-resolution Photoacoustic Microscopy of Endogenous Light-absorbing Biomolecules

Chi Zhang
Washington University in St. Louis

Follow this and additional works at: https://openscholarship.wustl.edu/etd

Part of the Biomedical Engineering and Bioengineering Commons

WASHINGTON UNIVERSITY IN ST. LOUIS

School of Engineering and Applied Science

Department of Biomedical Engineering

Thesis Examination Committee:
Lihong V. Wang, Chair
Gregory Lanza
Jin-Moo Lee
James Miller
Jung-Tsung Shen

Submicron-resolution Photoacoustic Microscopy of Endogenous Light-absorbing Biomolecules

by

Chi Zhang

A dissertation presented to the Graduate School of Arts and Sciences
of Washington University in partial fulfillment of the
requirements for the degree of
Doctor of Philosophy

May 2014

Saint Louis, Missouri

www.manaraa.com

Contents

List of Figures

List of Abbreviations

1D	One dimensional
2D	Two dimensional
3D	Three dimensional
CNR	Contrast-to-noise ratio
DR	Deconvolution reconstruction
ESF	Edge spread function
FAPT	Fluorescent-assisted photoacoustic thermometry
FFT	Fast Fourier transformation
FWHM	Full width at half maximum
H&E	Hematoxylin and eosin
IFFT	Inverse fast Fourier transformation
MAP	Maximum-amplitude projection
NA	Numerical aperture
OR-PAM	Optical-resolution photoacoustic microscopy
PA	Photoacoustic
PAI	Photoacoustic imaging
PAM	Photoacoustic microscopy
PSF	Point spread function
R^2	Coefficient of determination
SNR	Signal-to-noise ratio
SPAM	Sectioning photoacoustic microscopy
SW-PAM	Subwavelength-resolution photoacoustic microscopy
UV	Ultraviolet

Acknowledgments

I gratefully acknowledge the guidance, inspiration, and support from my research advisor, Dr. Lihong Wang. I also thank him for helping me establish a high ethical standard and a positive attitude throughout my Ph.D. study. This dissertation is based on the teamwork of many lab members and collaborators. I appreciate the contributions, hard work, and inspiring discussions from them, especially from Dr. Konstantin Maslov.

I would like to extend my appreciation to everyone who has helped me at Washington University. No virtue is trivial. I cherish them.

<div align="right">Chi Zhang</div>

Washington University in St. Louis
May 2014

Dedicated to my family

ABSTRACT OF THE DISSERTATION

Submicron-resolution Photoacoustic Microscopy of Endogenous Light-absorbing Biomolecules

by

Chi Zhang

Doctor of Philosophy in Biomedical Engineering

Washington University in St. Louis, 2014

Professor Lihong V. Wang, Chair

Photoacoustic imaging in biomedicine has the unique advantage of probing endogenous light absorbers at various length scales with a 100% relative sensitivity. Among the several modalities of photoacoustic imaging, optical-resolution photoacoustic microscopy (OR-PAM) can achieve high spatial resolution, on the order of optical wavelength, at <1 mm depth in biological tissue (the optical ballistic regime). OR-PAM has been applied successfully to structural and functional imaging of blood vasculature and red blood cells *in vivo*. Any molecules which absorb sufficient light at certain wavelengths can potentially be imaged by PAM. Compared with pure optical imaging, which typically targets fluorescent markers, label-free PAM avoids the major concerns that the fluorescent labeling probes may disturb the function of biomolecules and may have an insufficient density. This dissertation aims to advance label-free OR-PAM to the subcellular scale.

The first part of this dissertation describes the technological advancement of PAM yielding high spatial resolution in 3D. The lateral resolution was improved by using optical objectives with high numerical apertures for optical focusing. The axial resolution was improved by using broadband ultrasonic transducers for ultrasound detection. We achieved 220 nm lateral resolution in

transmission mode, 0.43 μm lateral resolution in reflection mode, 7.6 μm axial resolution in normal tissue, and 5.8 μm axial resolution with silicone oil immersion/injection. The achieved lateral resolution and axial resolution were the finest reported at the time. With high-resolution in 3D, PAM was demonstrated to resolve cellular and subcellular structures *in vivo*, such as red blood cells and melanosomes in melanoma cells. Compared with previous PAM systems, our high-resolution PAM could resolve capillaries in mouse ears more clearly. As an example application, we demonstrated intracellular temperature imaging, assisted by fluorescence signal detection, with sub-degree temperature resolution and sub-micron lateral resolution.

The second part of this dissertation describes the exploration of endogenous light-absorbing biomolecules for PAM. We demonstrated cytochromes and myoglobin as new absorption contrasts for PAM and identified the corresponding optimal wavelengths for imaging. Fixed fibroblasts on slides and mouse ear sections were imaged by PAM at 422 nm and 250 nm wavelengths to reveal cytoplasms and nuclei, respectively, as confirmed by standard hematoxylin and eosin (H&E) histology. By imaging a blood-perfused mouse heart at 532 nm down to 150 μm in depth, we derived the myocardial sheet thickness and the cleavage height from an undehydrated heart for the first time. The findings promote PAM at new wavelengths and open up new possibilities for characterizing biological tissue. Of particular interest, dual-wavelength PAM around 250 nm and 420 nm wavelengths is analogous to H&E histology.

The last part of this dissertation describes the development of sectioning photoacoustic microscopy (SPAM), based on the advancement in spatial resolution and new contrasts for PAM, with applications in brain histology. Label-free SPAM, assisted by a microtome, acquires serial distortion-

free images of a specimen on the surface. By exciting cell nuclei at 266 nm wavelength with high resolution, SPAM could pinpoint cell nuclei sensitively and specifically in the mouse brain section, as confirmed by H&E histology. SPAM was demonstrated to generate high-resolution 3D images, highlighting cell nuclei, of formalin-fixed paraffin-embedded mouse brains without tissue staining or clearing. SPAM can potentially serve as a high-throughput and minimal-artifact substitute for histology, probe many other biomolecules and cells, and become a universal tool for animal or human whole-organ microscopy, with diverse applications in life sciences.

x

Chapter 1

Introduction

1.1   Photoacoustic Imaging

In 1880, Bell found that heat converted from light absorption by matter results in a pressure rise propagating as acoustic waves, known as the photoacoustic effect [1]. Based on this effect, photoacoustic imaging (PAI), which forms images of optical absorption from the detected acoustic waves, has been developing quickly during the past few decades. PAI in biomedicine has the unique advantage of probing endogenous light absorbers at various length scales with a 100% relative sensitivity [2, 3]. For example, by probing hemoglobin, a major light-absorbing molecule in biological tissue, PAI has been demonstrated to image red blood cells and blood vasculature *in vivo*, as well as the associated functional parameters, such as hemoglobin oxygen saturation, flow speed, and metabolic rate of oxygen [4-7].

PAI has various modalities for applications at different depths in biological tissue. By focusing light to selectively excite biomolecules, PAI can achieve high spatial resolution, on the order of optical wavelength, at <1 mm depth (the optical ballistic regime). This modality of PAI is referred to as optical-resolution photoacoustic microscopy (OR-PAM) [8]. Also, in the optical diffusive regime up to a few centimeters deep, PAI can be realized by either scanning a focused ultrasonic transducer or using an array of ultrasonic transducers for detection, while the spatial resolution is on the order of acoustic wavelength due to low acoustic scattering. The former is referred to as acoustic-resolution photoacoustic microscopy [9], and the latter is referred to as photoacoustic computed tomography (see Appendix) [10-12]. In general, for all the modalities, the ratio of the imaging depth to the best spatial resolution is roughly a constant of 200, making PAI a high-resolution imaging technique across a length scale from organelles to organs [2].

Label-free PAI has demonstrated broad biomedical applications by imaging hemoglobin, melanin, DNA & RNA in nuclei, lipids, water, etc. [4, 13-15] over an optical wavelength range from middle-ultraviolet (UV) to near-infrared. This list is still expanding with the ongoing exploration of endogenous absorption. In fact, any molecules which absorb sufficient light at certain wavelengths can potentially be imaged by PAI. Compared with pure optical imaging, which typically targets fluorescent markers, label-free PAI avoids the major concerns that the fluorescent labeling probes may disturb the function of biomolecules and may have an insufficient density. Moreover, PAI can also take advantage of the growing pool of fluorescent probes and extend fluorescence imaging techniques to a much greater depth [16, 17].

1.2 Motivation

This work aims to advance label-free OR-PAM to the subcellular scale. First, we want to refine the technology in order to achieve high spatial resolution in 3D (Chapter 2). The lateral resolution can be improved by using a high numerical aperture (NA) optical objective for optical focusing. The axial resolution can be improved by using a broadband ultrasonic transducer for ultrasound detection. Second, with sufficient resolution, we want to explore more light-absorbing biomolecules for PAM and identify the corresponding optimal wavelengths for imaging (Chapter 3). This effort will broaden the potential biomedical applications of multi-wavelength PAM. Last, we want to demonstrate the potential of label-free PAM for high-throughput histology by imaging biomolecules of interest at selected wavelengths with subcellular resolution (Chapter 4).

Chapter 2

High-resolution 3D Photoacoustic Microscopy

This chapter describes the technical development of PAM for high resolution in 3D. The achieved lateral resolution and axial resolution were the finest reported at the time. Parts of this chapter have been published in Optics Letters, Journal of Biomedical Optics, and Applied Physics Letters [18-22].

2.1   Subwavelength-resolution Photoacoustic Microscopy in Transmission Mode

Background   PAM holds great potential for label-free imaging of melanoma and vasculature because nonfluorescent melanin and hemoglobin are major sources of endogenous absorption in biological tissue in the visible and near-infrared spectral range. Melanoma, arising from melanocytes, is the most deadly skin cancer [23]. The diagnosis of melanoma is based on inaccurate visual inspection and invasive biopsy. By providing *in vivo*, noninvasive, and high-resolution imaging, PAM promises to diagnose melanoma in the early stage, which is the key to successful treatment. Moreover, as a hallmark of cancer, tumor angiogenesis is currently imaged either *ex vivo* by microscopic methods at high resolution or *in vivo* by clinical methods at low resolution [24]. With high endogenous contrast, PAM can identify angiogenic vessels *in vivo*.

In OR-PAM, the NA of the optical objective is the key—the tighter the optical focus, the finer the image resolution. The first OR-PAM system reached a resolution of 5 μm [8]. Here, by using a water-immersion optical objective with a 1.23 NA, which is close to the ultimate limit, we have finally approached the highest diffraction-limited optical resolution and achieved subwavelength-resolution PAM (SW-PAM) with 220 nm resolution at 532 nm wavelength.

3
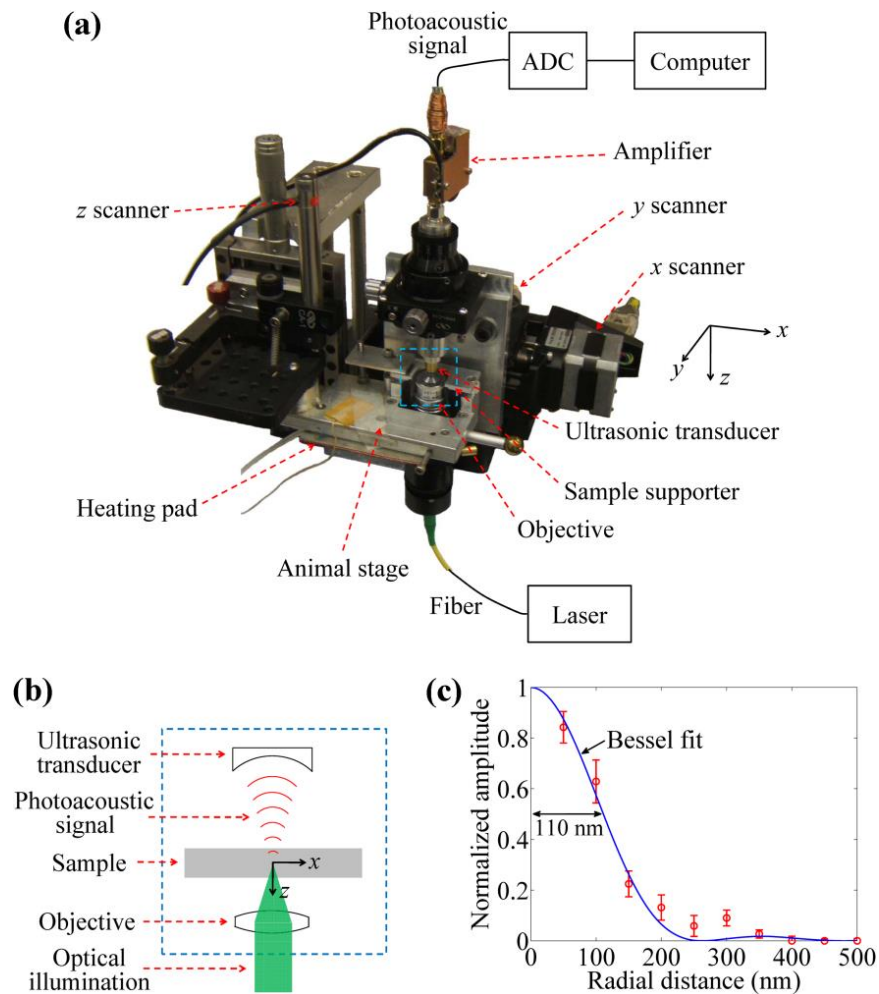
Figure 2.1 Subwavelength-resolution photoacoustic microscopy (SW-PAM). (a) Schematic diagram. (b) Close-up diagram showing the confocal structure of the optical objective and the ultrasonic transducer. (c) Point spread function of the system to measure the transverse spatial resolution. Red circle: the averaged pixel value. Blue line: the theoretical Bessel-form function.

Methods   In SW-PAM (Fig. 2.1), a Nd:YVO4 laser generated pulses with a 532 nm wavelength (λ) and a 1.5 ns duration. The pulses were coupled to a single-mode optical fiber, which was connected to the optical objective with a 1.23 NA. The sample was irradiated by the laser pulse focused by the objective, and the ultrasonic transducer (with a central frequency of 40 MHz and an NA of 0.5) detected the resulting time-resolved photoacoustic wave in transmission mode. The typical pulse energy was 10 nJ for slide samples and 60 nJ for mouse ears. The signals were then

4

amplified and digitized at a sampling rate of 1 GHz. The objective and the transducer mechanically scanned in raster mode in the x-y plane with a scanning speed of 2 mm/s and a step size of 125 nm, which was controlled by a separate computer. After scanning, a maximum-amplitude projection (MAP) image was obtained by projecting the maximum amplitude of each time-resolved signal onto the *x-y* scanning plane.

In order to measure the lateral resolution of SW-PAM, gold nanospheres with a diameter of 15 nm were imaged. A typical sphere was chosen, and the averaged pixel value was calculated with respect to the distance from the sphere center [Fig. 2.1(c)]. Then the data was fitted by the theoretical Bessel-form function [25]. The system resolution, given by the full width at half maximum (FWHM) of the Bessel-form point spread function (PSF), is 220 ± 20 nm (mean ± standard error), agreeing well with the theoretical value $0.51\lambda/\text{NA} \approx 221$ nm.

Results   To validate SW-PAM with wide-field optical microscopy, we imaged *ex vivo* melanoma cells and red blood cells. The PAM images have a dark background while the optical microscopy images have a bright background. The bright (white) dots in the PAM image of melanoma cells are melanosomes—organelles containing melanin [Fig. 2.2(a), left]. However, the melanosomes appear dark in the optical microscopy image [Fig. 2.2(a), middle] because their absorption attenuated the light transmission. The contrast between melanosomes and other areas in the PAM image [(54.5±0.4):1] is much higher than that in the optical microscopy image [(0.79±0.04):1] because PAM is sensitive to only absorption, but optical microscopy shows both absorption and scattering (the latter is relatively close between melanosomes and other areas). The average contrast-to-noise ratios (CNRs) for melanosomes are 49 dB and 25 dB in the PAM and optical microscopy images, respectively. The holes with few white dots inside the cells (PAM image) are nuclei, which is proved by staining them with 4',6-diamidino-2-phenylindole and taking a fluorescence optical microscopy image [Fig. 2.2(a), right]. The nuclei are difficult to identify in the optical microscopy image due to the low contrast. Here the melanoma cells have irregular shapes because they were grown on glass. For typical red blood cells [Fig. 2.2(b)], the contrast disparity between PAM and optical microscopy can also be observed, although we could not find the same cells under the two microscopes.

5
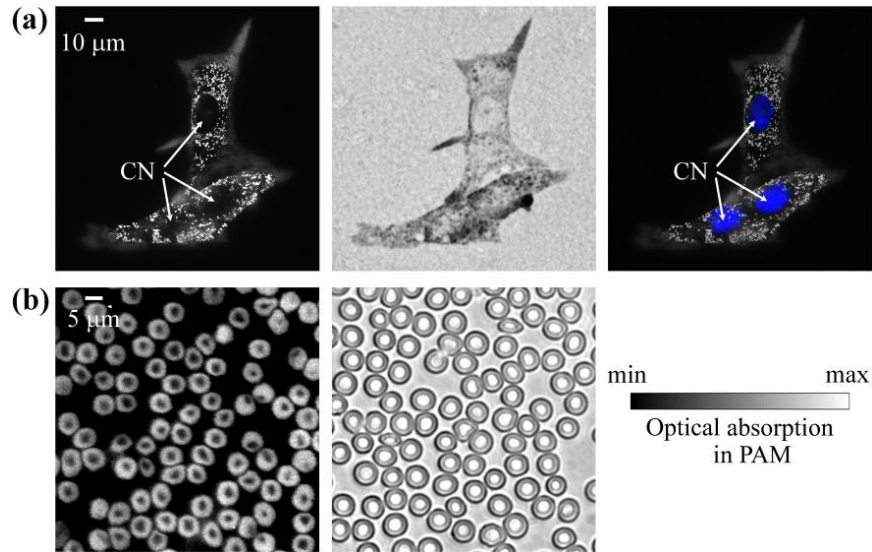
Figure 2.2 *Ex vivo* images of cells. (a) Melanoma cells grown on a cover glass and fixed. From left to right: PAM image, optical microscopy image (0.55 NA), and a composite of the PAM image and the fluorescence image of the stained nuclei (blue). In the PAM images the strong signals come mainly from melanin, and the white dots are melanosomes. CN: cell nucleus. (b) PAM and optical microscopy (1.0 NA) images of red blood cells. The strong signals in the PAM image come mainly from hemoglobin.

Then we imaged mouse ears *in vivo* with SW-PAM. All experimental animal procedures were carried out in conformity with the laboratory animal protocol approved by the Animal Studies Committee of Washington University in St. Louis. The melanin distribution in the ear (depilated) of a black mouse (Harlan Co., C57BL/6NHsd, 25 g, male) is shown in Fig. 2.3. Melanin synthesis occurs in melanosomes of melanocytes, and most melanocytes reside in the basal layer of the epidermis, whose thickness is about 10 μm in this case [26]. Thus, we acquired two images focusing at ~10 μm and ~30 μm deep, respectively. In the shallower layer [Fig. 2.3(a)], the single melanosomes can be clearly identified. In the deeper layer [Fig. 2.3(b)], most melanosomes are out of focus but more skin structures are shown, such as the sebaceous glands. Within this depth range we did not find an obvious decrease in resolution due to scattering. The signals from the deeper layer are weaker, but Fig. 2.3(b) appears to have higher contrast since it is scaled to the full color range. The optical microscopy image of the ear, although not shown here, has extremely low contrast. These results suggest potential applications of PAM in quantifying melanin distribution *in vivo*, which is important

for detecting melanoma as well as determining individualized radiant exposure in dermatological laser therapies [27].
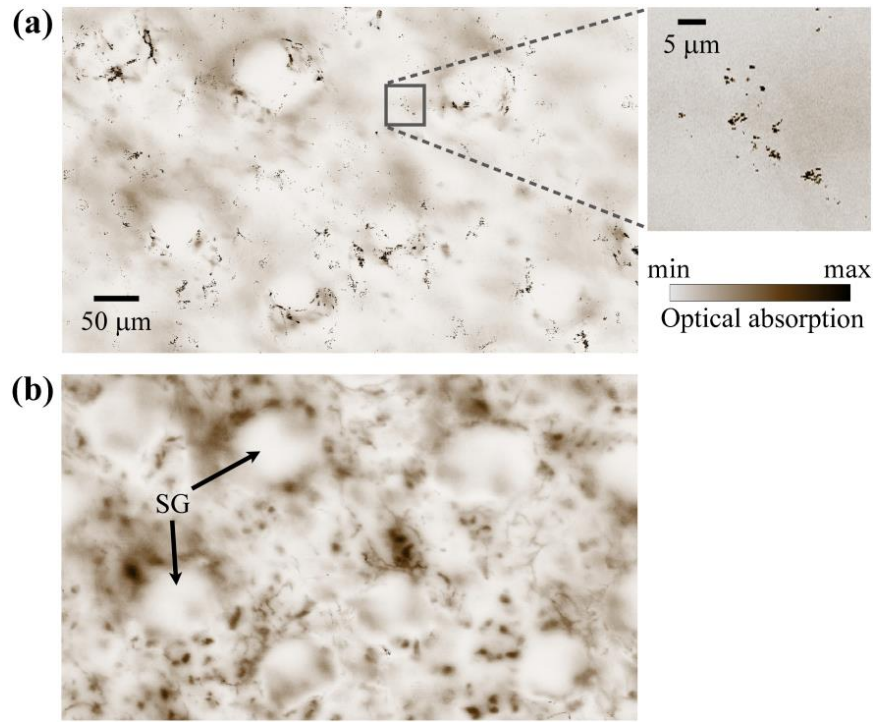
Figure 2.3 PAM images of a black mouse ear, showing the distribution of melanin. (a) Image focusing at ~10 μm deep (the close-up image indicates melanosomes). (b) Image focusing at ~30 μm deep. SG: sebaceous gland.

The ear of a nude mouse (Harlan Co., Hsd:Athymic Nude-Foxn1nu, 30 g, male) was also imaged *in vivo*. Here, we used an objective with a 0.60 NA (providing 400 nm resolution) instead because the thick layer of vessels required an extended focal zone. Since nude mice do not have much melanin in their skin, all the blood vessels, including capillaries, are shown with little background signals [Fig. 2.4(a)]. In some areas, we can see motionless red blood cells with the characteristic donut shape [Fig. 2.4(b)]. Because individual red blood cells can be imaged *in vivo*, SW-PAM can potentially be used to count red blood cells as an *in vivo* flow cytometer, measure blood flow velocity in capillaries, and monitor sickle cell disease.
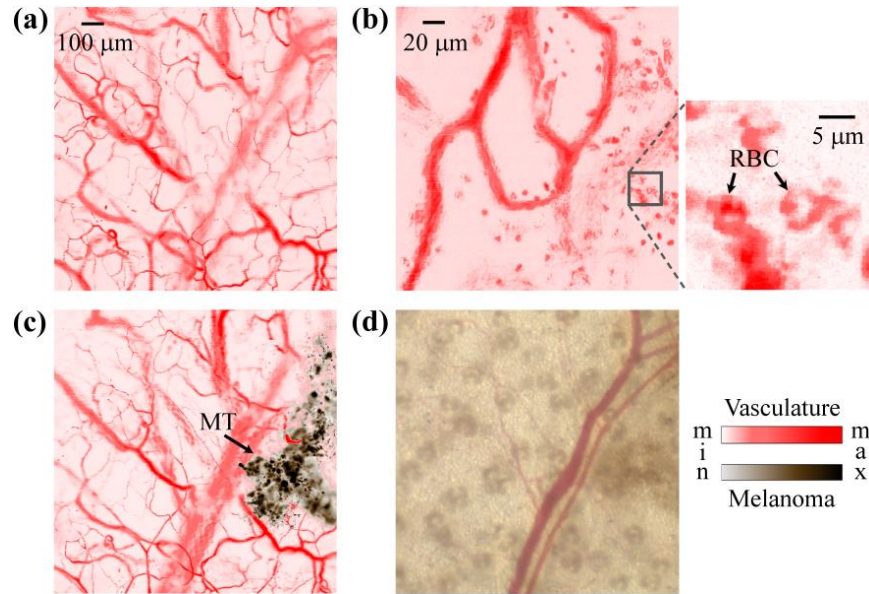
Figure 2.4 Monitoring of melanoma growing on a nude mouse ear. (a) PAM image of blood vessels in the ear acquired before injection of melanoma cells. (b) PAM image where *in vivo* red blood cells (RBCs) can be identified (the close-up image indicates the biconcave structure of RBCs). (c) PAM image of blood vessels and melanoma taken 4 days after injecting melanoma cells. The melanoma is extracted by taking the difference of the two PAM images [(a) and (c)] and is plotted in gray. MT: melanoma tumor. (d) Optical microscopy image (0.057 NA) of the same area in (a) and (c).

The same ear was imaged again, as shown in Fig. 2.4(c), 4 days after inoculation with 10 µL of suspension containing 1 million B16 melanoma cells. The melanoma generated stronger photoacoustic signals than the vessels and was easily identified. The vasculature and melanoma have contrasts of (12±1):1 (33 dB CNR) and (17±1):1 (36 dB CNR), respectively. If the laser wavelength is changed to, for example, 650 nm, we can further increase the contrast difference between vasculature and melanoma. In the wide-field optical microscopy image [Fig. 2.4(d)], the melanoma is obscure, with a contrast of (0.27±0.02):1 (21 dB CNR). Therefore, PAM has superior potential to detect melanoma in the early stage.

Discussion   As shown by the results in Figs. 2.2–2.4, SW-PAM can resolve structures as small as subcellular organelles for both *ex vivo* and *in vivo* imaging. Additionally, by simply replacing the optical objective, our system can work with scalable imaging resolutions. Since the thickness of tissues that can be imaged is limited by the transmission-mode configuration, we want to extend

www.manaraa.com

SW-PAM to reflection mode (see section 2.2) for applications in more anatomical sites. As a result, SW-PAM along with the scaled-up macroscopy—deep-penetrating photoacoustic tomography—may bridge microscopic research and clinical practice, especially for melanoma detection, vasculature visualization, reporter gene imaging [28], and sentinel lymph node mapping [29].

2.2   Submicron-resolution Photoacoustic Microscopy in Reflection Mode

Background   Resolution has always been a key factor and a research interest for PAM. The lateral resolution of the optical-resolution PAM (OR-PAM) is determined by the light wavelength (λ) and the numerical aperture of the optical objective—exactly speaking, by the formula 0.51λ / NA. We have achieved a lateral resolution of 220 nm for the transmission-mode OR-PAM (see section 2.1) by using a 1.23 NA optical objective at 532 nm wavelength. However, the transmission-mode configuration limits its applications to thin biological tissues, such as a mouse ear. While the reflection-mode configuration is not similarly limited, its implementation is more complicated, making it extremely difficult to realize a large NA in both optical illumination (for high resolution) and ultrasonic detection (for high sensitivity). Before this work, in the visible light range, the highest resolution reported for reflection-mode OR-PAM was ~2 μm with a 0.13 optical NA [30].

The existing design of the reflection-mode OR-PAM mainly falls into four categories, as shown in Fig. 2.5. First, an optical-acoustic combiner can be used to redirect the ultrasonic waves [Fig. 2.5(a)] [30]. However, the optical-acoustic combiner is too big to fit into the typically very small working distance of a large-NA objective. Moreover, under high-resolution conditions, it is difficult to precisely correct the optical distortion introduced by the acoustic lens and the 45° split between prisms. Second, a thin piece of glass can be used as the optical-acoustic splitter [Fig. 2.5(b)] [31]. But for a large-NA objective, even low refractive index glass (Magnesium Fluoride) will introduce non-ignorable distortion to the optical focusing. Third, a ring-shaped focused ultrasonic transducer can be used to detect the ultrasonic waves [Fig. 2.5(c)] [13]. To fabricate such a transducer, a flat active-surface is first made and then deformed to be spherical for the focusing, so the acoustic NA is limited to ~0.5. If the optical objective has a 0.5 NA, it is impossible to make a central hole in the

9

transducer that is big enough for the light to pass through. Last, it is possible to place a commercially-available focused transducer off axis [Fig. 2.5(d)] [32]. However, with a large optical NA, the NA of the transducer is very limited, and so is the detection sensitivity. Another issue with this design is the degradation of axial resolution (e.g., 2 times degradation with 60° off axis). Therefore, we need a new design for the submicron-resolution PAM.
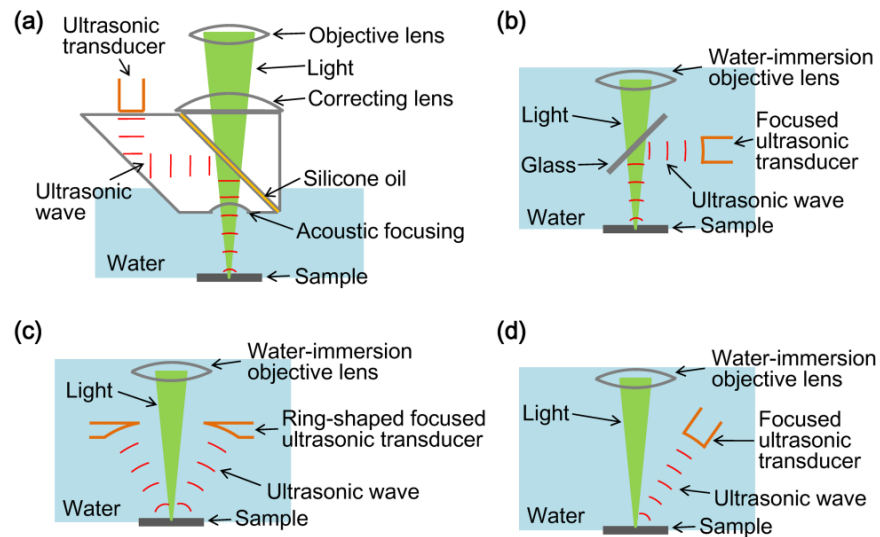
Figure 2.5 Major forms of reflection-mode OR-PAM. (a) An optical-acoustic combiner is used to transmit light and reflect sound. (b) A thin piece of optically transparent glass is used to reflect sound. (c) The ultrasonic waves are received by a ring-shaped focused ultrasonic transducer, which has a central hole to deliver light. (d) The focused ultrasonic transducer is placed off axis to prevent blocking the light.

Methods We implemented the reflection-mode submicron-resolution PAM by using a customized parabolic mirror (Ultrasonic S-Lab, LLC) to focus and redirect the ultrasonic waves, as shown in Fig. 2.6. With the parabolic mirror (1.3 mm focal length, 60° apex angle of conical hole, made of stainless steel), sufficient photoacoustic signals (0.26π solid angle, roughly equivalent to the solid angle of a 0.5 NA transducer) were collected for good sensitivity while the optical focusing is unaffected. The optical objective (BD Plan Apo SL50, Mitutoyo) has an NA of 0.47. A customized meniscus lens (Biomedical-Optics LLC) with two spherical surfaces, both centered at the objective focus, was used to couple the light from air into water. So the effective NA of the objective is 0.47 × 1.33 ≈ 0.63. Although a water-immersion objective might be more convenient, we did not find a

10

commercially available one with sufficient working distance (>7 mm). The photoacoustic signals were received by a flat ultrasonic transducer (53 MHz central frequency, 94% bandwidth, 4.5 mm diameter of active area) customized by ourselves. Besides the photoacoustic signals collimated by the parabolic mirror, those directly propagating to the ultrasonic transducer were also received. But they arrived earlier in time, and they destructively interfered on the transducer surface. So these early and weak signals were easily differentiated from the focused signals.
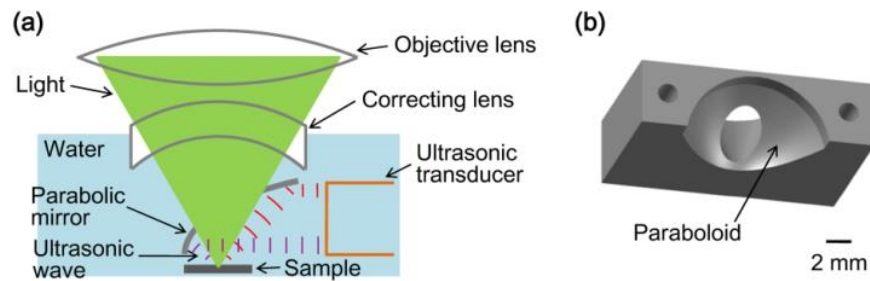
Figure 2.6 Reflection-mode submicron-resolution PAM. (a) Schematic of the core system. Acoustic focusing is achieved by the parabolic mirror, which has a central conical hole for light delivery. (b) 3D model of the parabolic mirror.

The complete system is described in detail as follows. A Nd:YVO4 laser (SPOT 100-200-532, Elforlight) was triggered by a computer to generate laser pulses with a 532 nm wavelength and a 1.5 ns duration. The laser pulses were coupled to a single-mode optical fiber, which was then connected to a collimator to generate a parallel beam as the input of the optical objective. The laser illumination and ultrasonic detection was explained previously (Fig. 2.6). The photoacoustic signals detected by the ultrasonic transducer were amplified, digitized at 1 GS/s (PCI-5152, National Instruments), and recorded into a computer. 2D raster scanning (PLS-85, MICOS) of the objective and the transducer while the time-domain photoacoustic signals were digitized enabled three-dimensional 3D imaging. Here, the 3D images may be shown as 2D MAP images projected along the depth direction.

www.manaraa.com
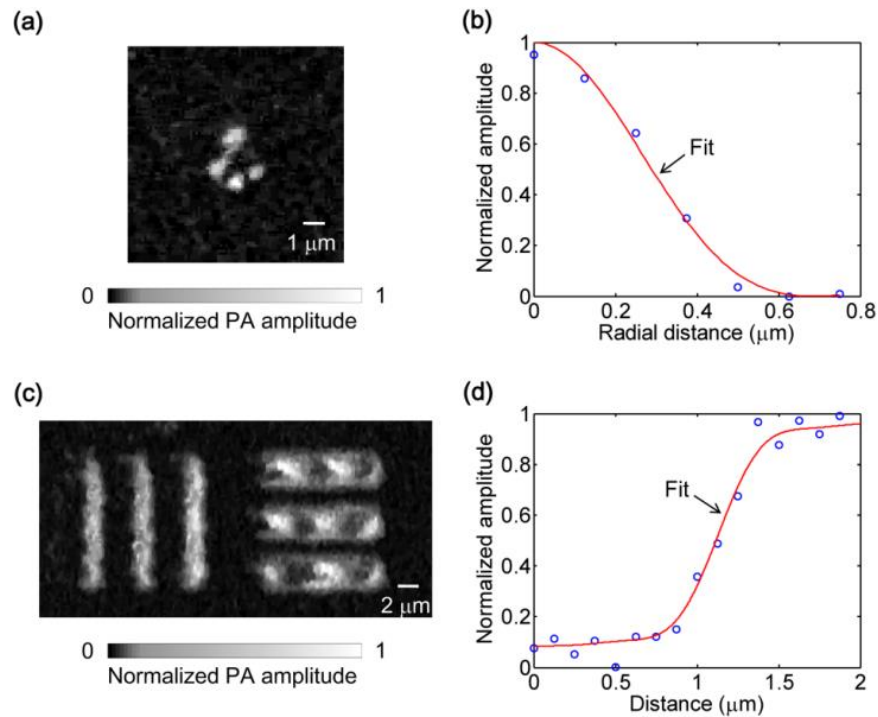
Figure 2.7 Measuring the lateral resolution of the submicron-resolution PAM. (a) PAM image of four gold nano-spheres of 50 nm in diameter each. (b) By fitting the point spread function centered at each nano-sphere, the lateral resolution is quantified as 0.58 ± 0.04 μm. Blue circle: experimental measurement. Red line: theoretical fit. (c) PAM image of an Air Force resolution test chart. (d) By fitting the edge spread function given by the bars, the lateral resolution is quantified as 0.50 ± 0.08 μm. Blue circle: experimental measurement. Red line: theoretical fit.

Results   We measured the lateral resolution of the submicron-resolution PAM. Gold nano-spheres with a 50 nm diameter were imaged to measure the PSF of the system. Fig. 2.7(a) shows the image of four nano-spheres. Fig. 2.7(b) shows the mean photoacoustic amplitude of one nano-sphere averaged over the 2π polar angular range versus the radial distance from the sphere center. The experimental data were fitted with the theoretical PSF, a Bessel-form function. The lateral resolution, defined by the FWHM of the PSF, was quantified to be 0.58 ± 0.04 μm by fitting the data from six nano-spheres. Taking into account that one nano-sphere in the image might be in fact an aggregation of several nano-spheres, which would worsen the estimated resolution, we measured the edge spread function (ESF) as a further validation. An Air Force resolution test chart was imaged, as shown in Fig. 2(c). The photoacoustic amplitude values along a line crossing the edge of a bar were fitted by the theoretical ESF [Fig. 2(d)], which could be calculated by integrating the 2D

PSF. In this way, the lateral resolution was quantified as 0.50 ± 0.08 μm by fitting the data from 16 edges. Therefore, we claim that the submicron-resolution PAM has a lateral resolution of ~0.5 μm. The theoretical lateral resolution is 0.51λ / NA ≈ 0.43 μm. The experimentally measured resolution is slightly worse, likely due to the imperfect air-water coupling [Fig. 2.6(a)].
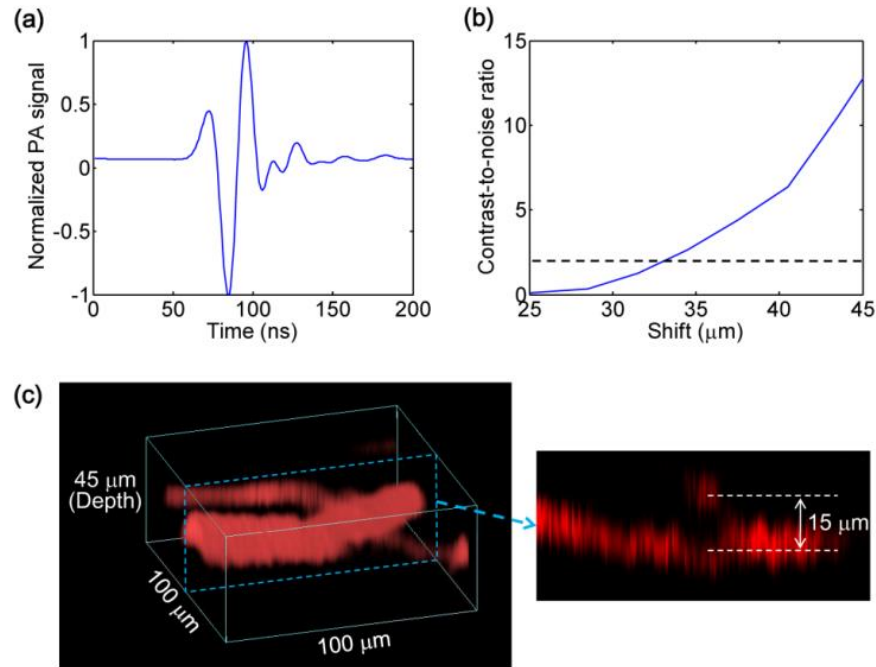
Figure 2.8 **Measurement of the axial resolution of the submicron-resolution PAM. (a) The A-line photoacoustic signal of a black tape. (b) When summing two A-line signals [shown in (a)] with a >33 μm shift, the CNR of the envelope is greater than 2. Dashed line: CNR = 2. (c)** *In vivo* **3D mouse ear image showing two crossed blood vessels (left panel) and a 2D cross-sectional image (right). By deconvolving the** *in vivo* **data with the impulse response shown in (a), the axial resolution is better than 15 μm.**

We also measured the axial resolution of the submicron-resolution PAM. The A-line photoacoustic signal of a black tape is shown in Fig. 2.8(a). As a conservative estimation, the axial resolution could be calculated by numerically shifting and summing two A-line signals and checking whether the two peaks could be differentiated (CNR greater than 2) in the envelope [Fig. 2.8(b)] [33]. In this way, the axial resolution was quantified as 33 μm, agreeing with the 50 MHz bandwidth of the transducer. However, when the signal-to-noise ratio (SNR) is sufficiently high, the axial resolution can be further improved by deconvolving the experimental A-line data with the system impulse response

13

[34], for which Fig. 2.8(a) can be used as the estimation. Fig. 2.8(c) shows the *in vivo* 3D image of a mouse ear (Hsd:Athymic Nude-Foxn1[nu], Harlan Co.) after using the Wiener deconvolution (~30 dB SNR here). Two blood vessels with a 15 μm distance in the depth direction were resolved. Therefore, with sufficient SNR (>12 dB as estimated by simulation), the axial resolution of the submicron-resolution PAM is better than 15 μm.

We tested the penetration depth of the submicron-resolution PAM by imaging a human hair inserted obliquely into chicken leg tissue *ex vivo*. Fig. 2.9(a) shows the B-scan image (fused from 3 B-scan images acquired by focusing at different depths: 0.04, 0.1, and 0.3 mm). The hair was imaged clearly with an SNR of ≥6 dB down to 0.42 mm beneath the tissue surface [Fig. 2.9(b)]. Therefore, the submicron-resolution PAM can penetrate ~0.42 mm in soft tissue.
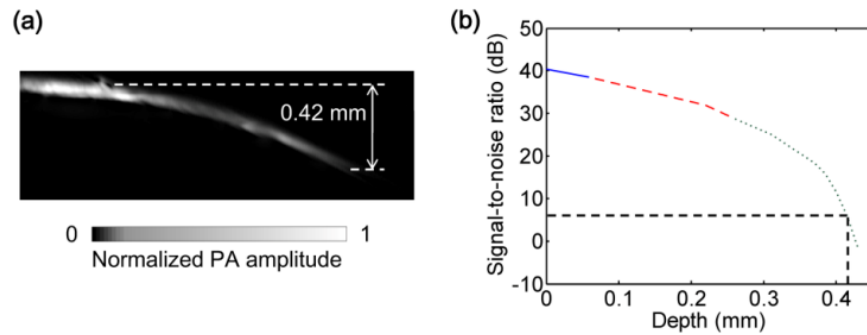
Figure 2.9 Measurement of the penetration depth of the submicron-resolution PAM. (a) A human hair inserted obliquely into chicken leg tissue is imaged clearly down to 0.42 mm beneath the tissue surface. (b) SNR of the hair versus imaging depth. Dashed lines indicate 6 dB SNR at 0.42 mm imaging depth. The data from the three focal depths 0.04, 0.1, and 0.3 mm are denoted by solid, dashed, and dotted line types.

The submicron-resolution PAM was compared with a 2.4 μm-resolution (calculated from the reported 2.6 μm resolution at 570 nm wavelength) PAM [30] by imaging a mouse ear (Hsd:Athymic Nude-Foxn1[nu], Harlan Co.) *in vivo*. Both systems used a 532 nm-wavelength laser. When imaging the ear, the submicron-resolution PAM used ~80 nJ pulse energy, and the 2.4 μm-resolution PAM used ~60 nJ pulse energy. Fig. 2.10(a) shows the image from the 2.4 μm-resolution PAM and the corresponding wide-field optical microscopy image (blood vessels had much lower contrast). The detailed comparison between the two PAM systems is shown in Fig. 2.10(b,c). As indicated by the

14

arrows, capillaries were resolved better by the submicron-resolution PAM. The capillaries appeared finer and richer in the submicron-resolution PAM image. But at the same time, some deeper vessels were out of focus because of the shorter focal zone (~1 µm).
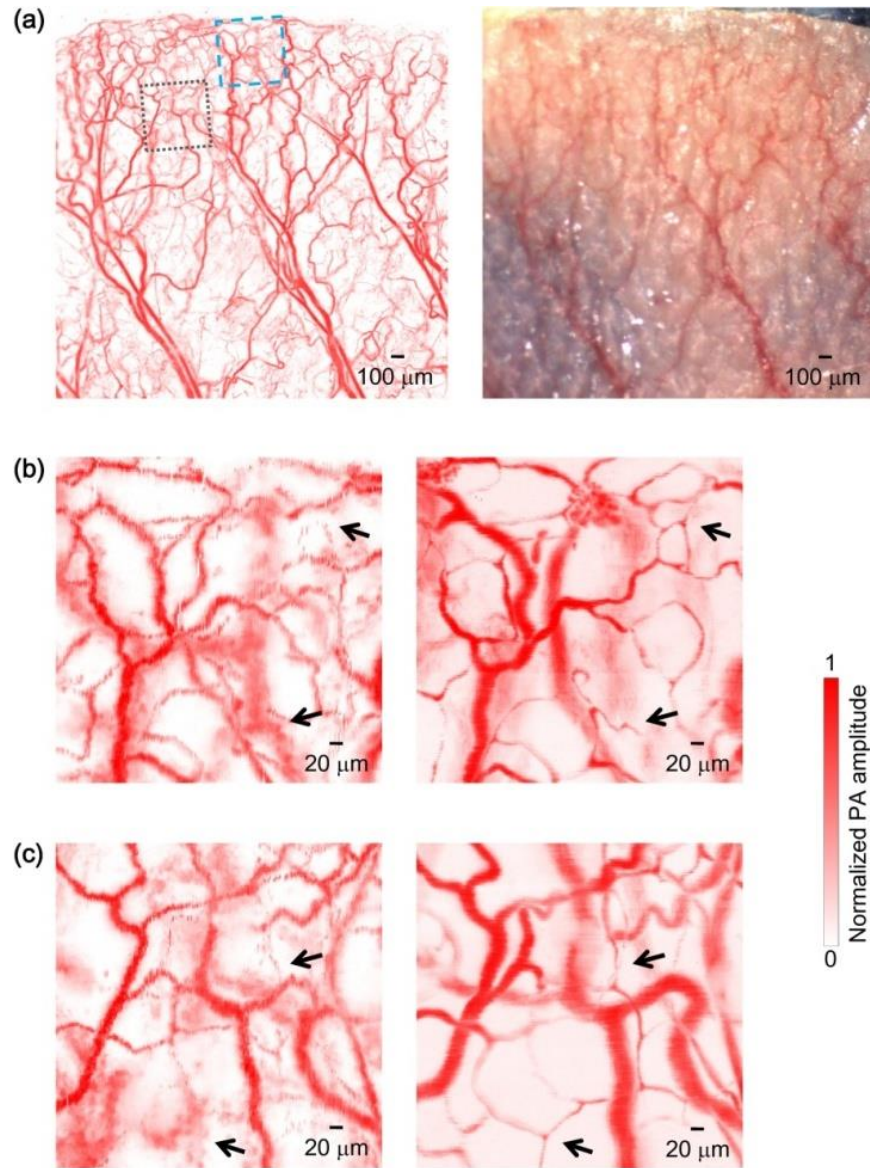
Figure 2.10 Comparing the submicron-resolution PAM with a 2.4 µm-resolution PAM by imaging a mouse ear *in vivo.* **(a) 2.4 µm-resolution PAM image of the mouse ear (left panel) and the corresponding wide-field optical microscopy image (right panel). (b) Close-up of the blue dashed square area in (a) (left) and the corresponding image from the submicron-resolution PAM (right). Selected differences of interest are indicated by arrows. (c) Close-up of the gray dotted square area in (a) (left) and the corresponding image from the submicron-resolution PAM (right). All PAM images are shown with the same color scale.**

15

Discussion   We have developed the submicron-resolution PAM in reflection mode. The 0.5 μm lateral resolution and the reflection-mode configuration suggest potential *in vivo* applications in high-resolution imaging, or even subcellular imaging, in anatomical sites up to ~0.42 mm in depth.

2.3   Micron Axial Resolution Achieved with a 125 MHz Ultrasonic Transducer

Background For OR-PAM, the axial resolution, provided by the time-resolved ultrasonic detection, can be estimated, if the impulse response of the ultrasonic transducer has a Gaussian envelope, as $0.88 \, c \, / \, B$ (see Theory section), where c is the speed of sound and B is the ultrasonic transducer bandwidth (approximately proportional to the central frequency). Increasing the bandwidth for better axial resolution will decrease the maximum imaging depth, because higher-frequency ultrasound attenuates faster in biological tissues. Before this work, ~15 μm axial resolution for depths up to 1.2 mm was reported, using the piezoelectric ultrasonic transducer with a 75 MHz central frequency and a 100 MHz bandwidth [35, 36]. Nevertheless, the axial resolution remains much lower than the lateral resolution in OR-PAM.

Besides piezoelectric ultrasonic transducers, optical sensors have been used for the ultrasonic detection, such as microring resonators [37] and Fabry-Perot sensors [38]. With broad bandwidth and low noise, microring resonators help achieve an axial resolution of 8 μm, which is the highest axial resolution achieved before this work. However, a microring resonator is unfocused, so, in spite of its high sensitivity to acoustic pressure, it generates images with lower quality than a focused piezoelectric transducer in a confocal arrangement [30]. Further, the 8 μm axial resolution has not been demonstrated in biological samples. Moreover, the microring resonator has not been commercialized yet, so it is not readily available to researchers.

We aim to improve the axial resolution of PAM. The first approach is to increase the bandwidth B. By using a commercial 125 MHz ultrasonic transducer (100 MHz bandwidth) for signal detection

16

and the Wiener deconvolution method for signal processing (broadening the effective bandwidth), the axial resolution has reached 7.6 μm, which was experimentally validated.

The second approach is to reduce the speed of sound c. Since an ultrasonic transducer detects the time-resolved signal, reducing the speed of sound would increase the time interval between two objects with a given spatial distance, thereby shortening the smallest resolvable distance between objects. Note that the time interval between two objects in the photoacoustic signal is determined by the speed of sound of the medium between them (ignoring acoustic scattering and reflection). In contrast, the speed of sound of the medium between the objects and the ultrasonic transducer determines the "time delay" to both signals from the two objects. Therefore, our method aims to reduce the speed of sound inside the imaging region of interest instead of the surrounding coupling medium (typically water or ultrasonic gel). This procedure can be realized by immersing the region of interest in a liquid that has a relatively low speed of sound. Our approach is analogous to the oil immersion used to increase the lateral resolution in optical microscopy [39]. In both cases, the acoustic or optical wavelength is decreased as the sound or light speed is lower in the immersion liquids.

The selection of immersion liquid is critical. With a lower speed of sound, the immersion liquid is expected to have a different acoustic impedance Z (= ϱc, where ϱ is the density) from that of the surrounding medium. The acoustic impedance mismatch will induce acoustic reflection at the interface, decreasing the detected signal amplitude and generating reverberation. In most biomedical applications of PAM, the acoustic impedances of the imaged soft tissues and the coupling water are about 1.6 MRayl and 1.5 MRayl, respectively, while the speeds of sound are approximately 1.5×10^3 m/s. To demonstrate the principle of our method, here we choose silicone oil (85421, Sigma-Aldrich) as the immersion liquid, whose speed of sound is about 1.1×10^3 m/s and acoustic impedance is about 1.1 MRayl. Thus the axial resolution is expected to be enhanced by ~1.4 times, while the acoustic impedance mismatch is relatively low (the amplitude reflection coefficient between the silicone oil and water is 0.16). Moreover, silicone oil is non-toxic and has been used in medical applications, such as in eye injection for managing complicated retinal detachments [40, 41] and in soft tissue injection for tissue augmentation [42, 43]. Without carrying out systematic

17

biological studies, we believe that silicone oil is a relatively simple and safe choice for injection into biological tissues to reduce the speed of sound.

Theory Here we derived the axial resolution of PAM. The impulse response $p(t)$ of the ultrasonic transducer is approximated as a Gaussian-modulated sinusoid [44]:

$$p(t) = Ae^{-\frac{(t-t_0)^2}{2\delta^2}} \cdot \cos(\omega_0 t + \varphi) ,\qquad (2.1)$$

where t is time, A is the amplitude of impulse response, ω_0 is the transducer central frequency, and t_0, δ, and φ are constants. The axial resolution R_a is given by the corresponding distance of the FWHM of the temporal Gaussian envelope:

$$R_a = 2\sqrt{2\ln 2}\,\delta \cdot c ,\qquad (2.2)$$

where c is the speed of sound.

The Fourier transformation of $p(t)$ is:

$$\hat{P}(\omega) = A\sqrt{\frac{\pi}{2}} \cdot \delta \cdot e^{-i\omega\left(t_0 - \frac{\varphi}{\omega_0}\right)} \cdot \left[e^{-\frac{(\omega-\omega_0)^2\delta^2}{2}} + e^{-\frac{(\omega+\omega_0)^2\delta^2}{2}} \right],\qquad (2.3)$$

where ω is the angular frequency. The acoustic -6 dB bandwidth B can be approximated by the FWHM of the Gaussian peak of $\left|\hat{P}(\omega)\right|$ at positive frequency:

$$B = \frac{2\sqrt{2\ln 2}}{\delta}\,(\text{rad/s})$$
$$= \frac{\sqrt{2\ln 2}}{\pi\delta}\,(\text{Hz}) \qquad . \quad (2.4)$$

Combining Eqs. (2.2) and (2.4) leads to:

$$R_a = \frac{4\ln 2}{\pi} \cdot \frac{c}{B} \approx 0.88\frac{c}{B} .\qquad (2.5)$$

Methods The experimental PAM system is shown in Fig. 2.11. A tunable OPO laser (NT242-SH, Ekspla) generated laser pulses (5 ns pulse width, 1 KHz pulse repetition rate) with 532 nm wavelength. The laser pulses were spatially filtered by a 50 μm pinhole and then focused by a 0.32 NA objective, providing ~0.8 μm lateral resolution. The laser pulse intensity was measured by a

18

photodiode (SM05PD1A, Thorlabs) to compensate for the intensity fluctuation. The photoacoustic waves excited by the focused laser pulse were detected by an ultrasonic transducer (125 MHz central frequency, 100 MHz bandwidth, 15 Pa noise equivalent pressure in the 100 MHz bandwidth; V2062, Olympus NDT) with a focusing acoustic lens (0.8 NA). The photoacoustic signals were amplified and digitized at 1 GS/s (PCI-5152, National Instruments). The sample was mounted on a scanning stage (PLS-85, MICOS). Both the laser and the scanning stage were triggered by a homemade controller, and the data acquisition card was triggered by the laser output for synchronization. Each time-resolved photoacoustic signal was converted to a 1D depth-resolved image, and the sample was mechanically scanned in 2D to generate a 3D image.
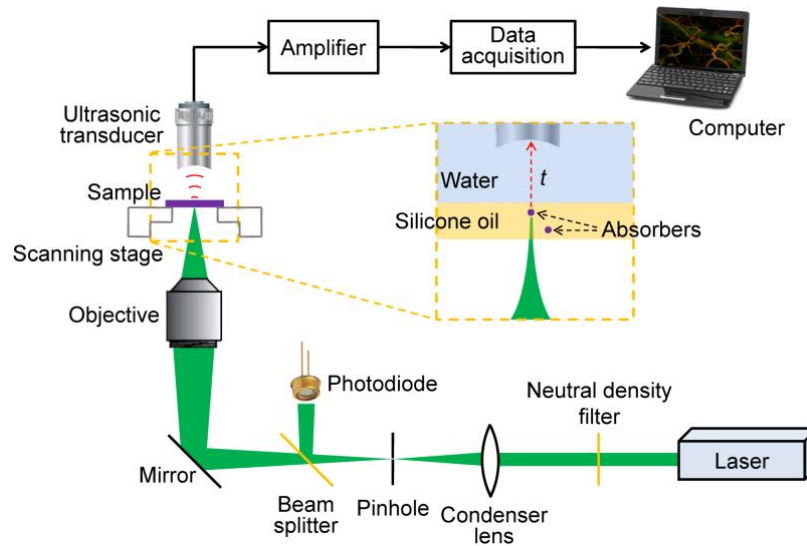
Figure 2.11 Schematic of the high-axial-resolution PAM system. The insert with a dashed line boundary shows the absorbers immersed in silicone oil and the ultrasonic transducer immersed in water. The acoustic flight time _t_ from the absorbers to the ultrasonic transducer can be converted to depth based on the speeds of sound in the two media.

To convert each photoacoustic signal to a depth-resolved image, the Hilbert transformation is normally used to extract the envelope of the short-pulsed photoacoustic signal. However, as shown in the literature, deconvolution methods can further improve the axial (depth) resolution [34]. Defining the photoacoustic signal from a point target to be the system impulse response, any photoacoustic signal can be approximately modeled as the convolution of the system impulse

19

response and the depth-resolved target function. Deconvolving the photoacoustic signal with the system impulse response exactly recovers the target function under perfect conditions (a linear and shift-invariant system with no noise). In other words, deconvolution recovers the attenuated frequency components of the signal and broadens the system bandwidth, thereby improving the axial resolution. In practice, however, deconvolution is very sensitive to noise, because the frequency components of the signal outside the system passband may be too weak to be recovered in the presence of noise. Therefore, the improvement of axial resolution by using deconvolution is limited, depending on the SNR. Here, the Wiener deconvolution method was used for imaging, and the results were compared with those using the Hilbert transformation method.

To reduce the speed of sound, we immersed the sample into silicone oil or injected silicone oil into the sample. The axial resolution is expected to be enhanced by ~1.4 times.

Results We designed a novel experiment to measure the axial resolution of the PAM system without silicone oil immersion. As shown in Fig. 2.12(a), the sample to be imaged consisted of two layers of red ink, one on the polymethylpentene (TPX) plastic (upper) and the other on the glass slide (lower). A small angle between the TPX plastic and the glass slide provided continuously variable distance between the two layers. The acoustic impedance of the TPX plastic is close to that of water, so the TPX plastic did not block the ultrasound to be received by the ultrasonic transducer placed on the top. The TPX plastic and the glass slide were coupled with ultrasound gel. A B-scan image of the sample calculated by the Hilbert transformation method is shown in Fig. 2.12(b). Note that the bottom layer of ink appears brighter in the image, because the light illuminates from the bottom. The CNR versus the distance between the two layers is shown in Fig. 2.12(c). The axial resolution, given by the distance with 6 dB CNR, is 12.9 μm. This is worse than the theoretical estimation given by the shift-and-sum definition (9.5 μm), likely because the top layer has a much weaker amplitude than the bottom layer and is therefore easier to be mixed into the bottom layer in the image.

As explained above, the Wiener deconvolution method can be used to improve the axial resolution. The B-scan image calculated by the deconvolution method is shown in Fig. 2.12(d). Both layers appear sharper than those in Fig. 2.12(b). The axial resolution is 7.6 μm [Fig. 2.12(e)], ~1.7 times

better than the result from the Hilbert transformation method. With higher SNR, we expect to achieve an even better axial resolution. Thus, the deconvolution method was used in the following imaging experiments.
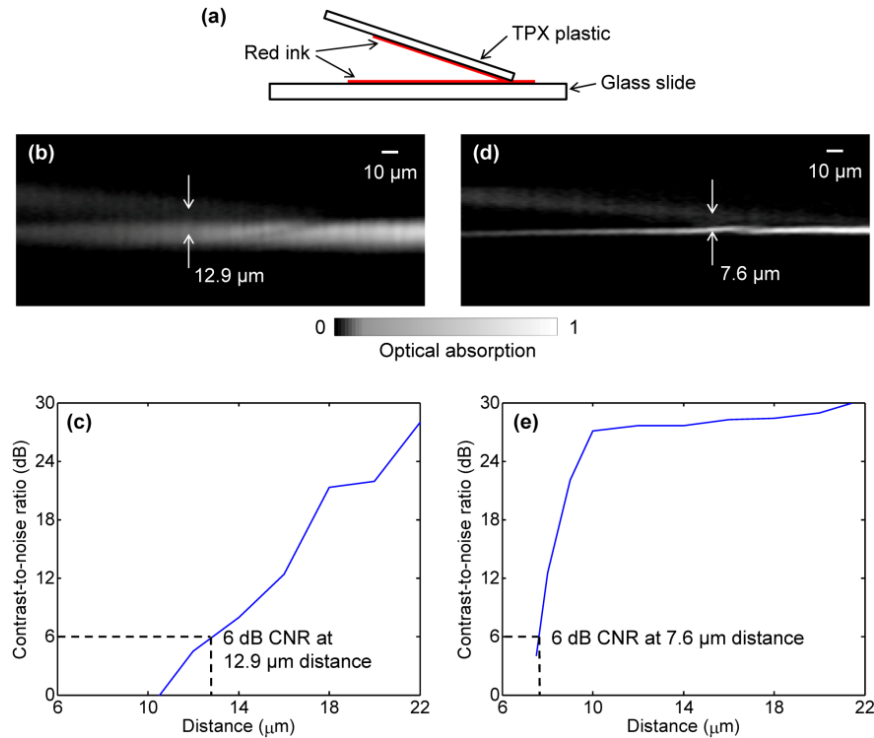
Figure 2.12 Experimentally measuring the axial resolution of PAM. (a) The sample to be imaged consists of two layers of red ink on polymethylpentene (TPX) plastic and glass slide, respectively. (b) The B-scan image of the sample calculated by the Hilbert transformation method. (c) The CNR versus the distance between the two layers of (b). The axial resolution is 12.9 μm by using the Hilbert transformation. (d) The B-scan image of the sample calculated by the deconvolution method. (e) The CNR versus the distance between the two layers of (d). The axial resolution is 7.6 μm by using the deconvolution.

We further demonstrated the axial resolution improvement by reducing speed of sound. As shown in Fig. 2.13(a), two layers of red ink for imaging were smeared on a polymethylpentene (TPX) plastic sheet (upper, matching well with water in acoustic impedance) and a glass slide (lower), respectively. The gap between the two layers was filled with either water or silicone oil for comparison, and the space between the two layers and the ultrasonic transducer was filled with water for coupling. B-scan images of the water-filled sample and the silicone-oil-filled sample are shown in Figs. 2.13(b) and

21

2.13(c), respectively. In both images, the vertical direction is plotted in the units of time. It can be seen that the bottom layer of ink, which was placed horizontally, appears oblique in Fig. 2.13(c). This is because that as the thickness of the silicone oil in the gap increases, the photoacoustic signal from the bottom layer takes longer to travel to the ultrasonic transducer due to the slower speed of sound in silicone oil compared with water. For the same reason, the two layers can be separated more clearly. The CNR versus the axial distance between the two layers of the water-filled sample and the silicone-oil-filled sample are shown in Figs. 2.13(d) and 2.13(e), respectively. The axial resolution, defined as the axial distance with 6 dB CNR, is 7.8 μm for the water-filled sample. The axial resolution is improved to 5.8 μm by silicone oil immersion, which is close to the theoretical prediction of 7.8 μm / 1.5 × 1.1 ≈ 5.7 μm.
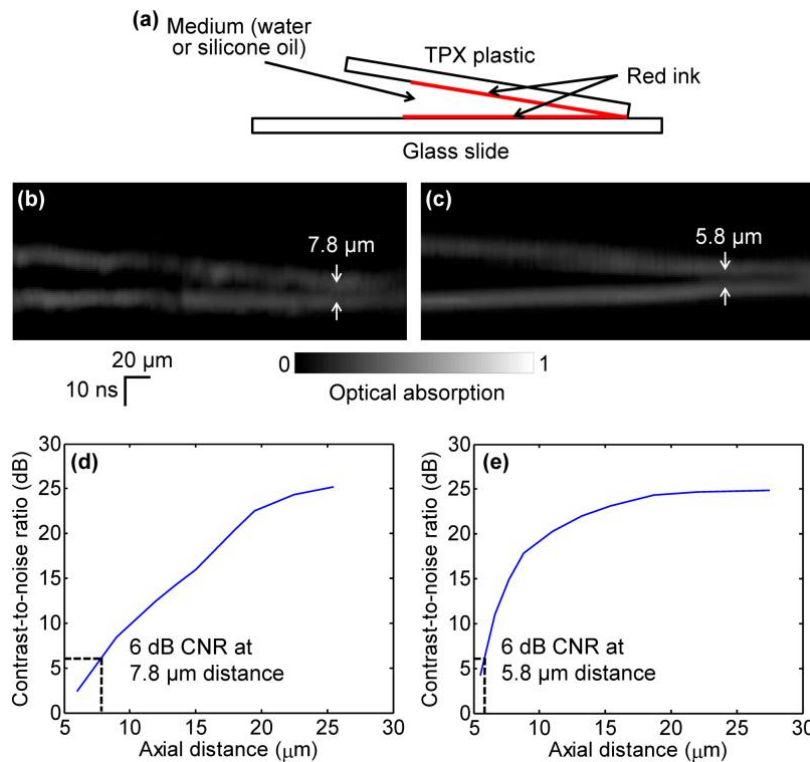
Figure 2.13 Axial resolution of PAM enhanced by silicone oil immersion. (a) Two layers of red ink are smeared on a polymethylpentene (TPX) plastic sheet (upper) and a glass slide (lower), respectively, for imaging. The gap between the two layers is filled with water or silicone oil. B-scan images of the water-filled sample (b) and the silicone-oil-filled sample (c). The CNR versus the axial distance between the two layers of the water-filled sample (d) and the silicone-oil-filled sample (e). The axial resolutions, defined as the axial distance with 6 dB CNR, are 7.8 μm for the water-filled sample and 5.8 μm for the silicone-oil-filled sample, respectively.

22

We measured the maximum imaging depths of PAM. To test the penetration capability from the acoustic side, we placed a piece of 1.2 mm-thick chicken tissue between the ink sample and the ultrasonic transducer, whose working distance is 1.2 mm. The system impulse responses, both without and with the 1.2 mm chicken tissue, are shown in Fig. 2.14(a). With the 1.2 mm chicken tissue in place, the SNR decreases by 11 dB, and the pulse width broadens by 36%. Thus the axial resolution degrades approximately 36% because of the faster attenuation of the high-frequency ultrasound in the 1.2 mm chicken tissue. To test the penetration capability from the optical side, a human hair was inserted obliquely into chicken tissue. As shown in Fig. 2.4(b), the hair was imaged clearly with an SNR of ≥6 dB up to 0.44 mm deep in the tissue (deeper penetration is possible by using a lower-NA optical objective). Therefore, the PAM system can penetrate up to 0.44 mm into soft tissue from the optical side, limited by the SNR, and penetrate up to 1.2 mm from the acoustic side, limited by the working distance.
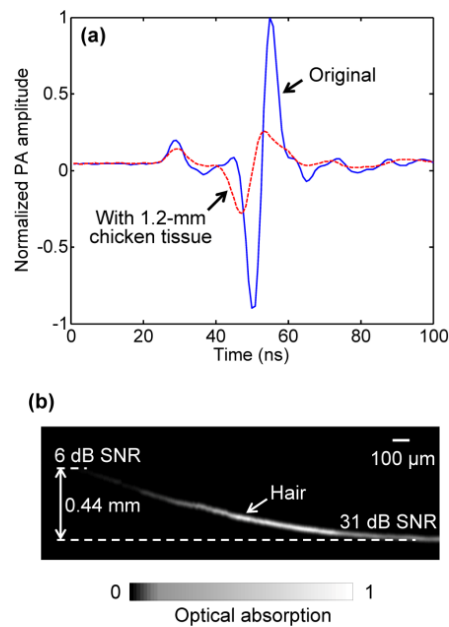
Figure 2.14 Measuring the maximum imaging depths of PAM from both the acoustic and optical sides. (a) System impulse responses without (blue solid line) and with (red dashed line) 1.2-mm chicken tissue on the acoustic side. (b) A human hair inserted obliquely into chicken tissue from the optical side is imaged clearly up to 0.44 mm in depth.

23
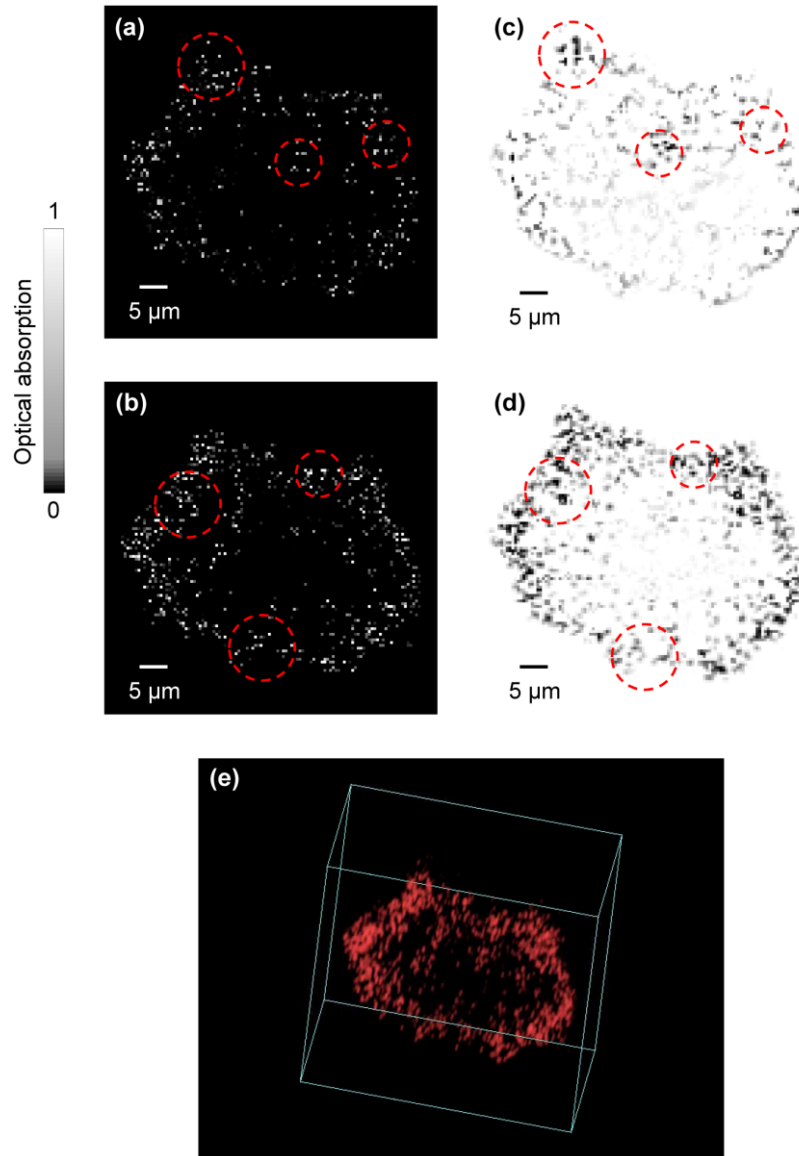
Figure 2.15 Imaging of a melanoma cell. Two cross sections (with 4 μm axial distance) of the cell are imaged by (a,b) PAM and (c,d) bright-field optical microscopy, respectively. Red dashed circles indicate features for comparison. (e) 3D PAM image. The cuboid size is 60 μm by 60 μm by 30 μm.

Melanoma cells fixed by formalin were imaged *ex vivo*. The cells were seeded onto a slide at a density of 30 mm^{-2}. Two cross sections of a cell with 4 μm axial distance are shown in Fig. 2.15(a,b). The bright dots in the PAM images are melanosomes, the organelles containing melanin. The PAM images were validated by bright-field optical microscopy (0.75 NA, 20X; FV1000, Olympus), as

24

shown in Fig. 2.15(c,d). The PAM image of the melanoma cell is rendered in 3D [Fig. 2.15(e)]. Here the melanosomes can be approximated as point targets, so bright-field optical microscopy can provide 3D images by depth scanning (not for planar targets) [25]. Note that PAM generates a 3D image without depth scanning. In Fig. 2.15(a–d), the features of interest are indicated by the red dashed circles. The circled features are similar between the PAM and bright-field images, but they do not appear in the adjacent section. However, the difference between the PAM and bright-field images can still be observed, because in practice it is very difficult to take PAM and bright-field images exactly at the same depth and with the same sectioning angle.

The high-axial-resolution PAM was compared with a PAM system [45] with a 50 MHz ultrasonic transducer (90% bandwidth) by imaging mouse ears *in vivo*. The difference in axial resolution was expected to be >2 times. Both systems worked in transmission mode for a fair comparison. Depth-encoded maximum-amplitude projection (MAP) images of an ear from the two systems are shown in Fig. 2.16(a,b). Some blood vessels in the two images appear different, because the light was not focused at exactly the same depth in the ear in the two experiments. The side-view MAP images, as shown in Fig. 2.16(c,d), demonstrate the improvement in axial resolution. The high-axial-resolution PAM system with the 125 MHz ultrasonic transducer resolves the blood vessels much more clearly.
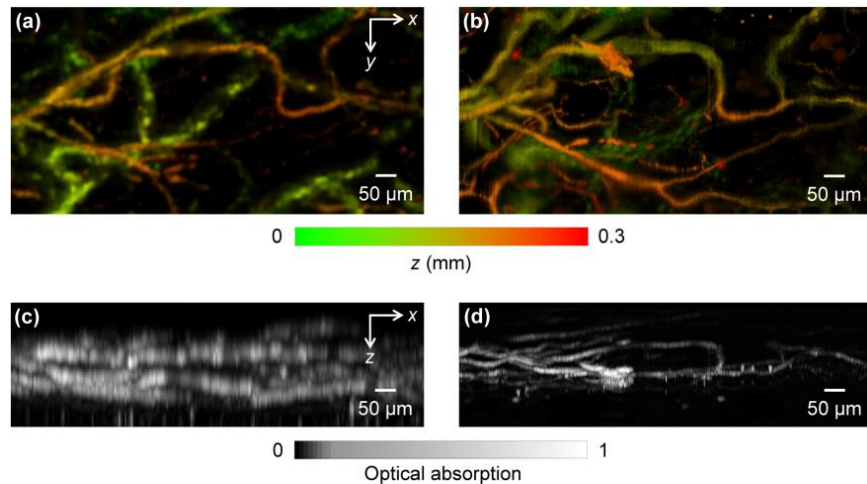
Figure 2.16 Comparison of *in vivo* PAM images of a mouse ear acquired with 50 MHz and 125 MHz ultrasonic transducers. Depth-encoded PAM images acquired with the (a) 50 MHz and (b) 125 MHz ultrasonic transducers. Side-view PAM images acquired with the (c) 50 MHz and (d) 125 MHz ultrasonic transducers.

25
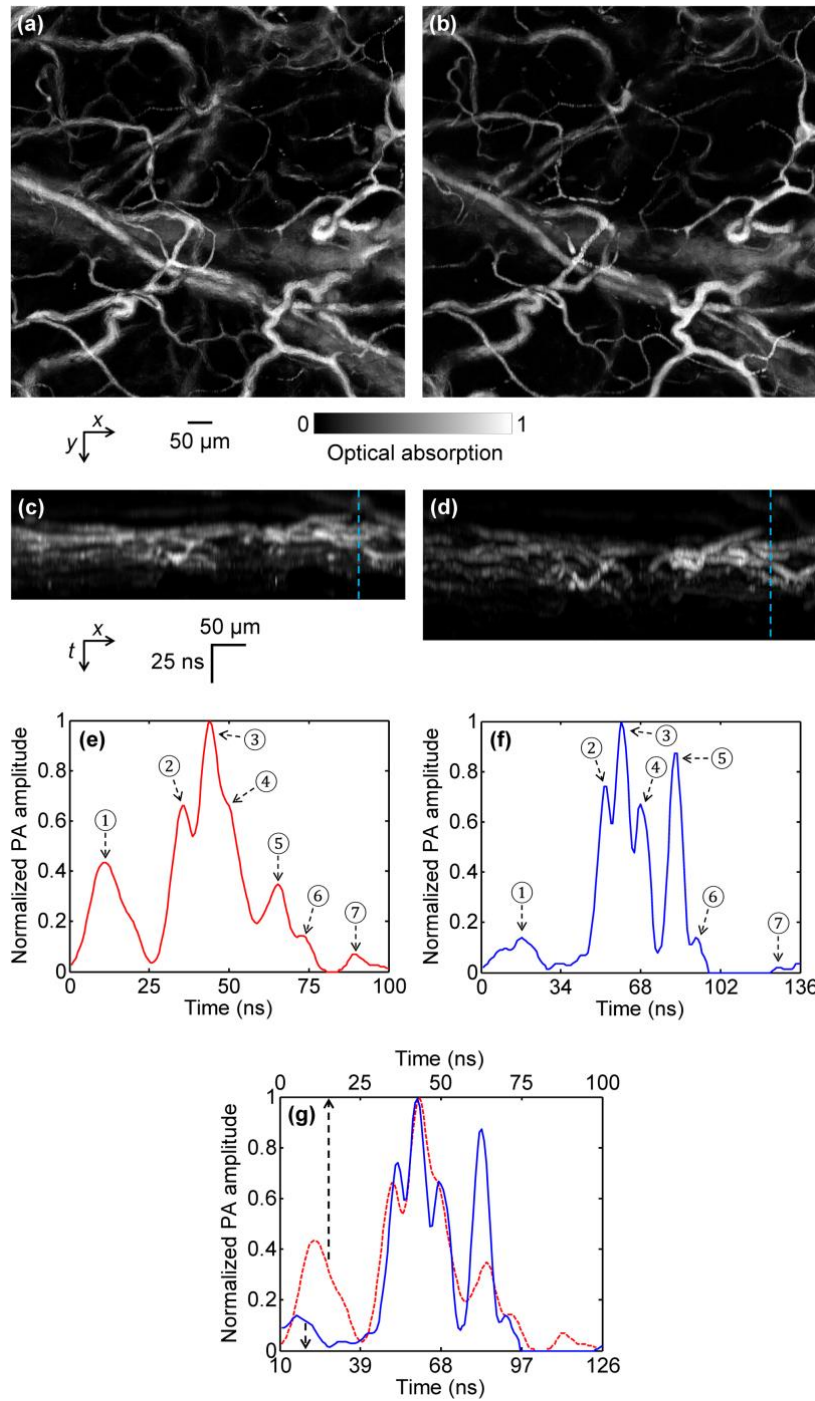
Figure 2.17 *In vivo* **PAM images of a mouse ear with silicone oil injection. Top-view PAM images before (a) and after (b) injection of silicone oil. Side-view PAM images before (c) and after (d) injection of silicone oil. (e) Normalized PA amplitude along the dashed line in (c). (f) Normalized PA amplitude along the dashed line in (d). Corresponding features in (e) and (f) are labeled with numbers. (g) Overlay of (e) and (f) with the corresponding time axes, as indicated by the arrows.**

We also showed potential biomedical applications of our method by injecting silicone oil into a mouse ear to enhance the axial resolution *in vivo*. Approximately 30 μL of silicone oil was injected into a nude mouse ear and allowed to diffuse for 30 min. The blood vessels in the silicone-oil-diffused area of the ear were imaged with the same laser intensity *in vivo* before and 30 min after injection, as shown in Figs. 2.17(a–d). The top-view maximum-amplitude-projection images are very similar before and after injection, but the side-view images demonstrate the improvement in axial resolution by injecting silicone oil. The amplitudes along the dashed profiles in Figs. 2.17(c) and 2.17(d) are shown in Figs. 2.17(e) and 2.17(f), respectively, with their overlay shown in Fig. 2.17(g), which further demonstrate that the blood vessels are resolved more clearly with silicone oil. In Fig. 2.17(g), the time scale of the profile from Fig. 2.17(f) has been adjusted to maximize the correlation coefficient between the two profiles (maximum at 0.82). Based on the ratio between the time scales of the two profiles, the average speed of sound was estimated to be $\sim 1.3 \times 10^3$ m/s in the post-injection mouse ear, an environment mixed with silicone oil and water. Due to the acoustic impedance mismatch between silicone oil and water, the CNR in post-injection images is about 2 dB lower than that in pre-injection images.

Discussion　　Detection sensitivity is a major concern when using a high-frequency ultrasonic transducer. In the *in vivo* mouse ear imaging experiment, the laser pulse energy was ~150 nJ. Assuming the optical focus was 80 μm beneath the skin surface, the surface laser fluence was 6.5 mJ/cm^2, well below the American National Standards Institute (ANSI) safety limit of 20 mJ/cm^2. So the 125 MHz ultrasonic transducer is suitable for *in vivo* blood vessel imaging. It can be calculated from the results in Fig. 2.14(a) that the attenuation coefficient of ultrasound in the chicken tissue is 92 dB/cm. For most soft tissues, the attenuation coefficient is nearly proportional to the acoustic frequency [46]. If the central frequency of the ultrasonic transducer is doubled, the acoustic penetration depth will decrease approximately 2 times. Therefore, challenges are expected if we want to further improve the axial resolution by simply using a higher-frequency ultrasonic transducer.

The deconvolution method used to improve the axial resolution has its limitations as well. Deconvolution should be applied to a linear and shift-invariant system. In PAM, as the laser intensity increases, the photoacoustic signal may become nonlinear with the laser intensity due to absorption saturation or nonlinear thermal expansion [47]. For oxyhemoglobin, the saturation

27

intensity has been reported to be $\sim 3\times 10^{12}$ W/m^2 [47]. With the nonlinear effects under such intensity, the deconvolution method may become invalid. In our *in vivo* experiments, the laser pulse energy is 150 nJ and the pulse width is 5 ns. If the optical focus is 80 μm beneath the skin surface and the extinction coefficient of the tissue is 100 cm^{-1}, light will attenuate $\sim 55\%$ at the optical focus according to Beer's law [48]. Then the intensity may exceed the saturation intensity within a ~ 7 μm depth range with the center at the optical focus. Moreover, the shift invariance holds accurately only within the focal zone of the ultrasonic transducer (~ 60 μm here) because the impulse response was measured at the acoustic focus. If a point target is far away from the acoustic focus in the depth direction, the received photoacoustic signal from the target will be quite different from the impulse response from the acoustic focus, causing errors in the deconvolution method. Taking Fig. 2.12(d) for example, the acoustic focus is approximately located at the bottom ink layer, which may be the major reason why the bottom layer appears thinner than the top layer in the deconvolved image. Here the top layer in Fig. 2.12(d) should still be located inside the acoustic focal zone, so the thickening of the top layer in the image may also indicate that either deconvolution starts to have error even within the acoustic focal zone or the acoustic focus is in fact slightly below the bottom layer. However, we can measure impulse responses at multiple axial positions and use time-variant-filtering inversion methods to ameliorate this problem [49, 50].

The acoustic lens for the ultrasonic transducer was made with a large NA of 0.8 in order to increase the solid angle of acoustic detection and thereby the SNR. Here, SNR is critical because the 125 MHz ultrasonic transducer has relatively low detection sensitivity, and high frequency ultrasound attenuates faster in biological tissue. The limitation associated with the high acoustic NA is the small depth of field (~ 60 μm), within which the acoustic amplitude degrades $< \sqrt{2}$ times compared with that at the focal point. Outside the acoustic focal zone, the SNR is weaker, and the axial resolution is lower. As shown by the results in Fig. 2.16(d), we could image blood vessels within a depth range of 150 μm, about 20 times the axial resolutions, with relatively good image quality.

Nonlinear effects in PAM can in fact be another mechanism to provide axial resolution other than the time-resolved ultrasonic detection. For example, two-photon-absorption induced PAM has been reported to achieve an optically-determined axial resolution of 45 μm [51]. Theoretically, even submicron axial resolution is possible with a high-NA optical objective. However, for this technique,

28

additional depth scanning is required as in two-photon microscopy, which dramatically slows down image acquisition. In addition, due to the inefficiency of two-photon absorption at the ANSI-limited laser intensity, the two-photon-absorption signal may be weak.

An axial resolution of 7.6 µm has been achieved for PAM in general cases. With silicone oil immersion, we have achieved a finest axial resolution of 5.8 µm, and with silicone oil injection, we improved the axial resolution in imaging mouse ears *in vivo*. The improved axial resolution benefits PAM in high-resolution 3D imaging. It is possible to further improve the axial resolution, at the cost of detection sensitivity, by using an immersion liquid with a lower speed of sound, such as fluorosilicone oil (7.6×10^2 m/s) or tallow (3.9×10^2 m/s). For biomedical applications, we will seek more low-speed biocompatible immersion liquids. The immersion method can potentially be used in other imaging modalities, such as photoacoustic computed tomography and ultrasound imaging.

2.4   Application in Intracellular Temperature Imaging

Background   Many cell events are accompanied by intracellular temperature change, such as cell division, nutrient metabolism, and gene expression [52-54]. Accurately measuring cellular temperature can, in turn, contribute to a deeper understanding of biochemical processes inside a cell. Although cellular thermometry has been realized at the single-cell level by employing tools such as micro- or nano-scale thermocouples [55, 56], fluorescence nanoparticles or nanogels [57, 58], and a photoacoustic thermometer [59], most of these techniques have treated a cell as a whole and measured its average temperature. Knowledge of the average cellular temperature is insufficient for exploring thermogenesis and thermal dynamics at the level of subcellular structures [53].

The difficulty of achieving intracellular temperature mapping lies in a fact that it requires measuring a physical quantity sensitive to local temperature changes but independent of the sensor's concentration and excitation strength. Only two fluorescence-based techniques have realized intracellular temperature mapping, utilizing fluorescence lifetime [60] and polarization anisotropy [61], respectively. Despite the high spatial (sub-micron) and temperature resolution ($\sim 0.5^\circ$C) they

29

have accomplished in cellular imaging experiments, both methods rely on custom-developed fluorescent biosensors, limiting their accessibility to only a few laboratories.

A major impetus towards the widespread application of fluorescence microscopy is the ongoing development of fluorescent probes, which display excellent selective labeling of cellular structures [62]. However, most commercially available fluorescent probes were not intended to be temperature sensitive. To expand the toolbox of intracellular temperature mapping technique and make it accessible to a much broader biological research community, here we present a method – fluorescent-assisted photoacoustic thermometry (FAPT), which integrates fluorescence microscopy with photoacoustic thermometry on one platform. FAPT features the unique capability of transforming a generic fluorescent probe into a concentration- and excitation-independent intracellular temperature sensor.

Theory   Upon absorbing a photon, a fluorophore's electron transits from the ground state to an excited state. The electron's energy is released primarily via two paths [63, 64]: radiative decay, *i.e.*, fluorescence, or non-radiative decay, *i.e.*, thermal dissipation. The possibility of an electron following either of these two decay approaches is described by the fluorophore's quantum yield η. After excitation, the emitted fluorescence intensity equals [64]

$$I_f = AF\mu_a\eta, \quad (2.6)$$

where A is a constant, F is optical fluence (J/cm^2), and μ_a is the absorption coefficient (cm^{-1}). μ_a is dependent on the fluorophore's concentration and its molecular absorption cross-section.

On the other hand, if the excitation light is a short pulse, the generated heat during non-radiative decay produces an ultrasonic wave via thermoelastic expansion. The detected photoacoustic amplitude is [64, 65]

$$P = BF\mu_a(1-\eta)\Gamma. \quad (2.7)$$

In Eq. (2.7), B is a constant, and Γ is the Grueneisen coefficient, which is temperature dependent by an empirical relation [66]

$$\Gamma = C_1 + C_2T, \quad (2.8)$$

where T is the local temperature, and C_1 and C_2 are constants.

30

The temperature can be measured by collecting fluorescence and photoacoustic signals simultaneously at each scanning point. Combining Eqs. (2.6-2.8) leads to

$$T(x, y) = \frac{A}{C_2 B} \frac{\eta}{(1-\eta)} \frac{P(x, y)}{I_f(x, y)} - \frac{C_1}{C_2}. \quad (2.9)$$

In FAPT, a new quantity R is defined as the ratio of the photoacoustic amplitude P to the fluorescence intensity I_f. For a fluorophore whose quantum yield η is insensitive to temperature changes, Eq. (2.9) can be simplified as

$$T(x, y) = D_1 R(x, y) - D_2, \quad (2.10)$$

where the coefficients $D_1 = A\eta / C_2 B(1-\eta)$ and $D_2 = C_1 / C_2$ are independent of μ_a and F and remain constant for the same fluorophore, and $R = P/I_f$. Since D_1 and D_2 can be calibrated for, by measuring the ratio R at each scanning point, the corresponding local temperature can be derived.

Method The FAPT was realized by adding a fluorescence channel to the high-resolution PAM system (described in Section 2.3). The FAPT system setup is shown in Fig. 2.18. A pulsed laser (wavelength: 532 nm, pulse duration: ~5 ns) both excited the fluorescence and generated photoacoustic signals. Two objectives, with NA=0.32 (Leitz Wetzlar Phaco 10×) and NA=1.40 (Olympus PLAPO 60×), focused the excitation laser and collected fluorescence signal. The spatial resolutions corresponding to these two objectives were 0.82 µm and 0.23 µm, respectively. A combination of an excitation filter (central wavelength 532 nm, bandwidth 3 nm), a dichroic beamsplitter (transmission wavelength 400-530 nm, reflection wavelength 575 nm-725 nm), and an emission filter (central wavelength 559 nm, bandwidth 34 nm) separated excitation light from fluorescence. The fluorescent light was detected by a photomultiplier tube (PN: PMM01, Thorlabs), while the PA signal was acquired by a custom-made focused ultrasound transducer with a central frequency of 40 MHz and a numerical aperture of 0.5. In order to obtain a 2D temperature map, the sample was raster scanned across the region of interest.

31
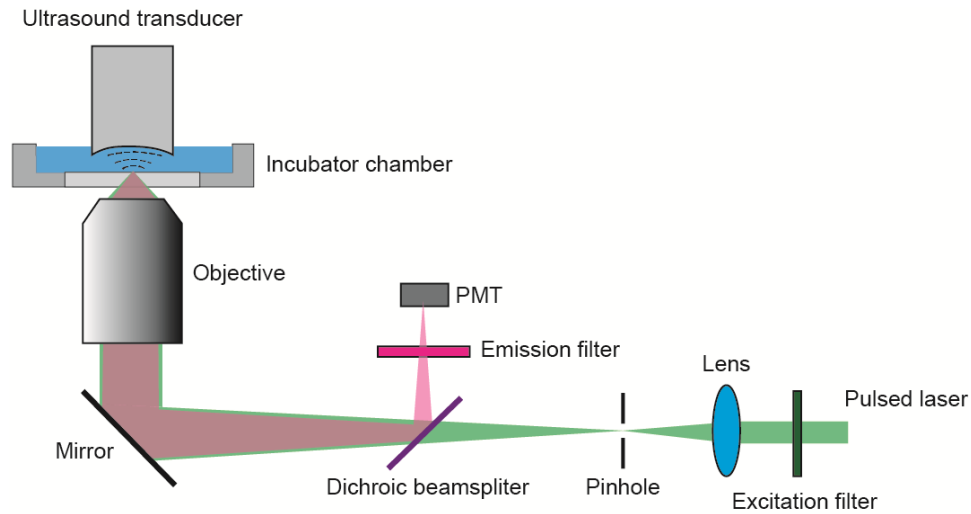
Figure 2.18 FAPT system setup. The fluorescence and PA signals were measured simultaneously at each scanning point. PMT: Photomultiplier tube.

The sample was immersed in phenol-red free medium (PN: 21063-029, Life technologies) in an incubator chamber (PN: CSC-25, Bioscience Tools), whose temperature could be finely adjusted (step: 0.01°C) by the accompanying controller (PN: TC-1-100s, Bioscience Tools). The temperature of the incubator chamber was monitored by a thermocouple (ON-401-PP, Omega) immersed in the bath.

Results   To demonstrate FAPT, we imaged the temperature of a phantom, using a common fluorescent dye, Rhodamine 6G, as the temperature sensor. The excitation and emission maxima of Rhodamine 6G are at 530 nm and 552 nm, respectively, with a stable quantum yield over a wide temperature range [67, 68].

To calibrate the relation between the PA/fluorescence ratio R and temperature for Rhodamine 6G, first we measured the PA and fluorescence signals simultaneously from a thin layer of Rhodamine 6G in aqueous solution (0.5 mM concentration) at different temperatures. The results are shown in Figs. 2.19(a)-(c). Here the PA signals were averaged over a 0.1×0.1 mm^2 area for 10 seconds, and the temperature T was measured by the thermocouple in the bath while it rose from 25 °C to 37 °C [Fig. 2.19(a)]. Fig. 2.19(b) implies that the PA signal generally increased with temperature T. However,

fluctuations in both laser pulse energy and dye concentration caused by photobleaching and diffusion diverted this relation from linearity, and were also revealed by the corresponding fluorescence variations as shown in Fig. 2.19(c). However, the PA/fluorescence ratio, R, had a close linear relationship with the temperature [Fig. 2.19(d)), where the coefficient of determination (R^2) for the linear fit is 0.98. Hence, the influences of laser pulse energy and dye concentration fluctuations were eliminated by taking the ratio. The relative increase of R per degree at 25 $^{\circ}$C was 4 %, which is in good agreement with previous studies [69].
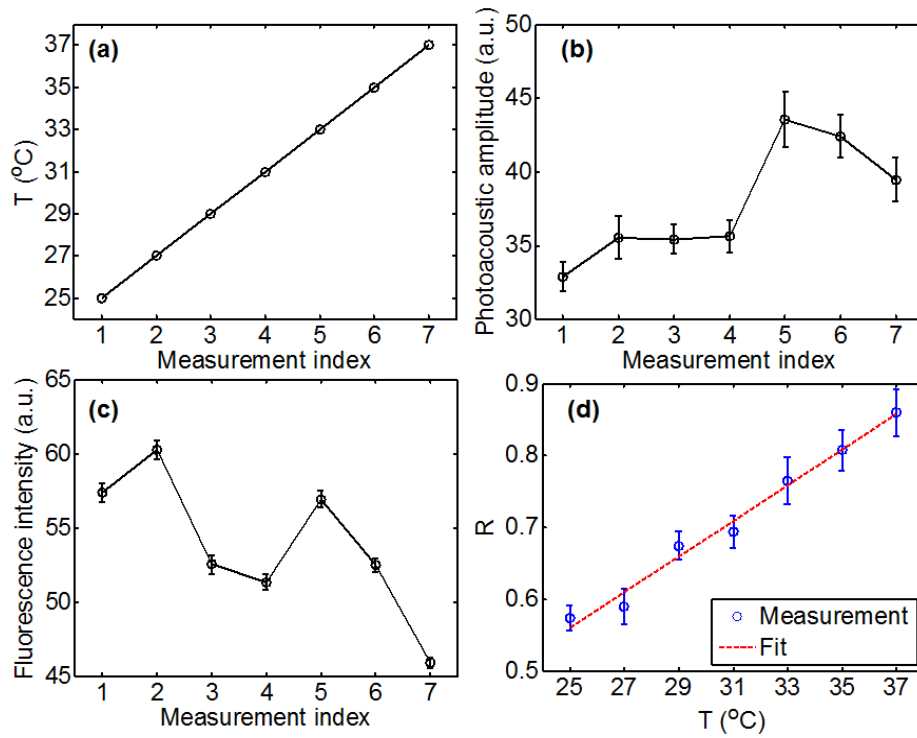
Figure 2.19 Calibration of PA/fluorescence ratio versus temperature. (a) Temperature versus measurement index. (b) PA amplitude versus measurement index. (c) Fluorescence intensity versus measurement index. (d) PA/fluorescence ratio R versus temperature T. The coefficient of determination is 0.98 for the linear fit.

The uncertainty of the derived temperature from Eq. (2.10) was estimated as

$$\frac{|\Delta T|}{T} \approx \frac{|\Delta P|}{P}. \quad (2.11)$$

33

Thus the uncertainty of the derived temperature $|\Delta T|$ approximates $0.08T$. At 25 °C, this value is around 2 °C. The relative low temperature resolution here is due to the weak PA signal generated by the fluorophore. To keep the excitation within the linear excitation range, we used moderate excitation pulse energy, ~70 nJ (laser fluence at the focus: 2.2 J/cm²). Since the quantum yield of Rhodamine 6G is around 95%, the majority of absorbed light energy is converted to fluorescence, resulting in unbalanced signal distribution between the fluorescence and PA channels. However, if higher temperature resolution is desired, PA signals can be averaged over time to improve their SNR.
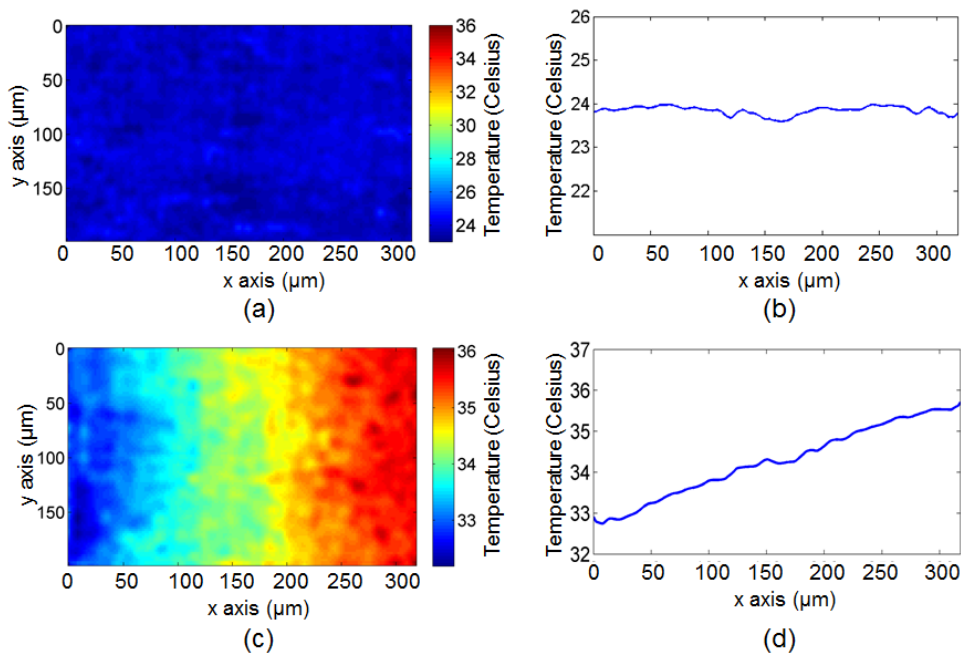
Figure 2.20 2D temperature mapping of a thin layer of Rhodamine 6G dye. The phantom sample was heated at the right end. The FAPT-recovered temperature mapping (a) before and (c) after heating. Vertically averaged temperature profile along the horizontal direction (b) before and (d) after heating.

Next, based on this calibration, we measured the 2D temperature gradient of a heated phantom. A thin layer of Rhodamine 6G aqueous solution (0.5 millimolar concentration) was smeared on a piece of glass slide which was then heated at one end by a metal wire illuminated by a 50 mW near-

34

infrared laser at 1064 nm. The microscope objective (Leitz Wetzlar Phaco 10×) with NA=0.32 focused excitation light and collected fluorescence. The temperature gradients close to the wire, imaged by FAPT before and after heating, are shown in Figs. 2.20(a) and 2.20(c), respectively. As expected, before heating, the temperature was uniform across the field [Fig. 2.20(b)]; after heating, the measured temperature gradually decreased from the heated end (right) to the un-heated end (left) [Fig. 2.20(d)]. The temperature profile shown in Figs. 2.20(b) and 2.20(d) were calculated by averaging over the entire range along the y axis.

We applied FAPT to cellular temperature imaging. A mitochondrion is a cellular organelle that produces energy and heat via oxidization. Temperature imaging of mitochondria would help to understand cellular metabolism [53]. Here we stained HeLa cells (30-40 microns in diameter) with a commercially available fluorescent dye – MitoTracker orange (PN: M-7510, Life technologies, Inc.) and monitored the mitochondria temperature during environmental temperature changes.

The HeLa cells grew in Dulbecco's Modified Eagle Medium with 10% fetal bovine serum and 1% penicillin/streptomycin supplement. The cells were incubated at 37 °C in 5% CO_2 and split every 72 hours. After being dispersed in 0.25% EDTA-trypsin, they were seeded at $2\text{-}4\times10^4$ cells per square centimeter. Culture medium was removed 24 hours after imbedding cells on a cover glass and replaced by staining solution, a fresh culture medium containing 10 μM MitoTracker Orange probes (PN: M-5710, Life technologies). After incubation in staining solution for 60 minutes, the cells were rinsed twice with fresh medium. After staining, cells were trypsinized, collected and suspended in extraction buffer (PN: FNN0011, Life technologies). To inhibit proteolysis, 50 μL of protease inhibitor cocktail (PN: P2714, Sigma-Aldrich) for each milliliter of buffer and 0.5 mM phenylmethanesulfonyl fluoride (PN: P7626, Sigma-Aldrich) were added before the extraction. Cells with the extraction solution ware kept on ice for 40 minutes with occasional vortexing. The lysate was clarified by centrifugation at 13000×g for 15 mins.
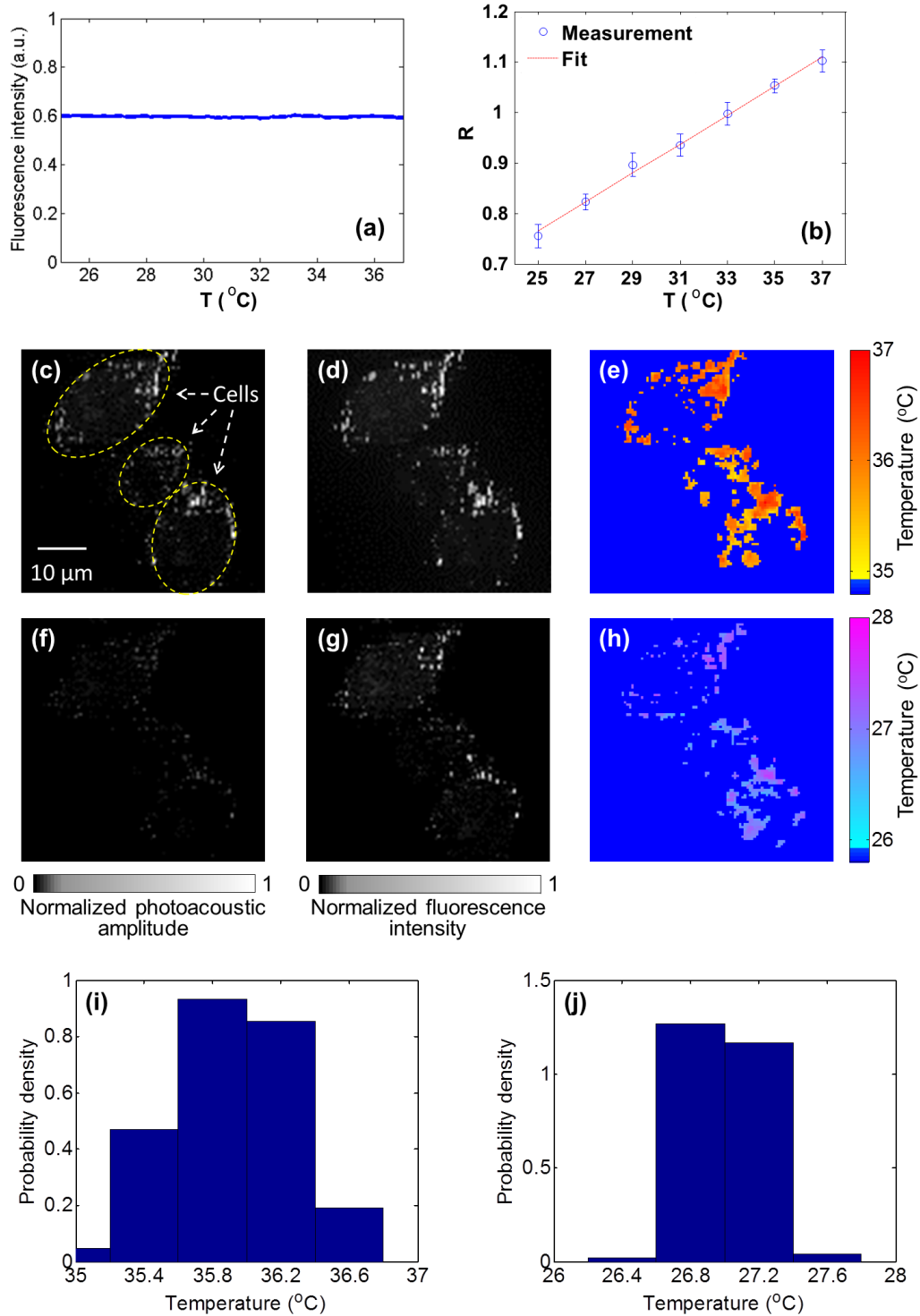
Figure 2.21 Intracellular mitochondrial temperature mapping by FAPT. (a) The temperature dependence of fluorescence intensity for the fluorophore MitoTracker orange. The quantum yield of MitoTracker orange is stable over a temperature range of 25 ºC – 37 ºC. (b) The PA/fluorescence ratio R versus temperature for the

Mito Tracker orange fluorophore. The coefficient of determination is 0.995 for the linear fit. (c)-(e) PA, fluorescence, and FAPT-recovered mitochondrial temperature map at 36 °C. (f)-(h) PA, fluorescence, and FAPT-recovered mitochondrial temperature map at 27 °C. The dark blue background in (e) and (h) denotes unknown temperatures. (i)-(j) The temperature histograms of (e) and (h). The mean values are 35.9 °C and 27.0 °C, respectively.

To be eligible for FAPT imaging, the quantum yield of the chosen fluorescent dye must be temperature-insensitive. Since insensitivity had not been reported for the fluorescent dye MitoTracker orange, we first measured it in aqueous solution. By exciting the fluorophore and collecting the corresponding fluorescence at each temperature, the relation between fluorescence intensity and temperature was acquired [Fig. 2.21(a)]. The result shows that the quantum yield of MitoTracker orange is stable over 25 °C – 37 °C, a temperature range of interest in cellular studies [60, 61].

Then, by following a procedure similar to that in the phantom experiment, we calibrated the relation between the PA/fluorescence ratio R and temperature for MitoTracker orange in cell extract [Fig. 2.21(b)]. The R^2 is 0.995 for the linear fit. The SNR of the measured PA and fluorescence signals were 33 dB and 49 dB, respectively, resulting in ~0.7 °C temperature resolution in the presented experiment. Note that the temperature resolution is higher here than that measured in the phantom experiment, because MitoTracker orange has a lower quantum yield than Rhodamine 6G and thus a more balanced PA signal versus fluorescence.

Next, the HeLa cells stained with MitoTracker orange were imaged by FAPT at environmental temperatures of 36.0 °C and 27.0 °C. The microscope objective (Olympus PLAPO 60×) with NA = 1.4 focused excitation light and collected fluorescence. Figs. 2.21(c)-(e) show the measured PA, fluorescence, and FAPT-recovered mitochondrial temperature map acquired at 36 °C, respectively. Figs. 2.21(f)-(h) show the corresponding images acquired at 27 °C. Since MitoTracker orange was selectively stained on the mitochondria, few photoacoustic and fluorescence signals were measured in other cellular organelles. The unknown temperature outside mitochondria was pseudo-colored as dark blue in Figs. 2.21(e) and 2.21(h). Additionally, the histograms of measured intracellular temperature distribution were also calculated [Figs. 2.21(i)-(j)]. The mean values are 35.9 °C and 27.0

°C, respectively, in good agreement with the corresponding environmental temperatures. Note that the standard deviation of measured cellular temperature (0.4 °C) at 36.0 °C is higher than that (0.2 °C) at 27.0 °C, which may indicate the cells being more active in heat production and consumption at body temperature.

Discussion   We presented a generic technique, FAPT, for intracellular temperature mapping applications. Phantom and cellular experiments demonstrated that FAPT is capable of measuring the 2D temperature distribution of an optically thin sample with sub-micron spatial resolution and sub-degree temperature resolution.

Compared to previous fluorescence-based methods, FAPT features the unique capability of transforming a regular fluorescence dye into a concentration- and excitation- independent temperature sensor, a fact that opens up the possibility of utilizing a large collection of commercially available fluorescent probes for intracellular temperature sensing applications. This advantage should facilitate the conversion of intracellular temperature mapping into a routine lab tool and make it accessible to a much broader research community. Additionally, since environmental temperature can affect cellular activities by changing enzyme activity [70], membrane characteristics [71], or ion channel gating [72], FAPT can be utilized to study the dependence of cellular thermogenesis or reaction on environmental temperature changes, a knowledge that would promote our understanding of cellular metabolism regulation and diagnosis of related diseases.

2.5   Conclusions

We implemented technical advancements to improve the spatial resolution of OR-PAM in 3D. We achieved 220 nm lateral resolution in transmission mode, 0.43 μm lateral resolution in reflection mode, 7.6 μm axial resolution in normal tissue, and 5.8 μm axial resolution with silicone oil immersion/injection. These advancements facilitate the applications of PAM in cellular and subcellular imaging. We demonstrated the application of intracellular temperature imaging, achieved by FAPT, with sub-degree temperature resolution and sub-micron lateral resolution.

Chapter 3

Endogenous Light-absorbing Biomolecules for Photoacoustic Microscopy

This chapter describes the exploration of endogenous light-absorbing biomolecules for PAM. The findings promote PAM to new wavelengths and open up new possibilities for characterizing biological tissue. Parts of this chapter have been published in Journal of Biomedical Optics [73-76].

3.1   Photoacoustic Microscopy of Cytochromes

Background   Label-free PAM has been successfully applied to *in vivo* imaging of hemoglobin and melanin, two major sources of endogenous optical absorption in biological tissue in the visible spectral range. Recently, additional photoacoustic contrasts have been demonstrated by exciting DNA and RNA in nuclei [13] with UV illumination, and water [15] and lipid [14] with near-infrared illumination. In fact, PAM can potentially image any molecule which has sufficient absorption at specific wavelengths.

We have realized OR-PAM with high resolution in 3D to show subcellular structures; however, few endogenous subcellular contrasts, apart from DNA and RNA in cell nuclei, have so far been imaged by PAM. Here we hypothesize that hemeprotein in cytoplasm can be imaged by PAM around the Soret peak (~420 nm). Hemoglobin and myoglobin, two types of hemeprotein, exist mainly in red blood cells and muscle cells, respectively. In other cells, the most common hemeproteins are cytochromes, mainly located in mitochondria, whose main function is electron transport using the heme group. Previous spectrophotometric results have provided evidence that cytochromes are a major source of endogenous subcellular optical absorption at their absorption peaks [77]. Photothermal technologies have been utilized to image mitochondria in cells, where the absorption

source has sometimes been assumed to be mainly cytochrome *c* [78], but the assumption has not been verified [79]. In this study, we analyzed the absorption origins in cells by photoacoustic spectroscopy [80].

Label-free PAM of cytochromes in cytoplasm is expected to be a useful technique for studying live cell functions, such as how the release of cytochrome *c* from mitochondria regulates apoptosis [81]. Label-free PAM avoids concerns about fluorescence microscopy that the fluorescent labeling probes may disturb the function of biomolecules and may have an insufficient density. For example, Mitotracker® labeling has been found to affect mitochondrial permeability and respiration [82]. Moreover, by imaging cytoplasm and nuclei without labeling, PAM can provide higher throughput than standard hematoxylin and eosin (H&E) histology, and even image live tissues in 3D *in situ* without sectioning. Here, by using optical illumination around the Soret peak, we applied PAM to image cytochromes in the cytoplasm of fixed cells and of histological sections.

Methods We built a free-space PAM system for cytochrome imaging, shown in Fig. 3.1. An integrated diode-pumped Q-switched laser and optical parametric oscillator system (NT242-SH, Ekspla) generated laser pulses (5 ns pulse width, 1 KHz repetition rate) with a tunable wavelength range from 210 nm to 2600 nm. The laser pulses were sequentially filtered by an iris (ID25SS, Thorlabs; 2 mm aperture), focused by a condenser lens (LA4380, Thorlabs), filtered by a 50 μm pinhole (P50C, Thorlabs), and focused again by an objective. The objective for visible light (46 07 15, Zeiss) has a 0.60 NA, and the one for UV light (LMU-20X-UVB, Thorlabs) has a 0.40 NA. This free-space system provides both greater tolerance of beam shifting and easier optical alignment than a fiber-based system for tuning the wavelength over a large range. The focused laser pulse generated a spatially and temporally abrupt temperature rise in the focal zone inside the sample and thereby excited photoacoustic waves. The photoacoustic waves were detected by a focused ultrasonic transducer (customized with 40 MHz central frequency, 80% bandwidth, and 0.50 NA) coupled by water, and then amplified, digitized at 1 GS/s (PCI-5152, National Instruments), and finally recorded by a computer. The relative optical absorption at the focal point was calculated by the amplitude of the photoacoustic signals. 3D imaging was realized by 2D raster scanning (PLS-85, MICOS) of the sample while converting the arrival time of each photoacoustic signal to depth. Here, since the sample thickness used in this paper was comparable to or even smaller than the axial

40

resolution (~40 μm, as determined by the acoustic bandwidth), we show only 2D MAP images projected along the depth direction.
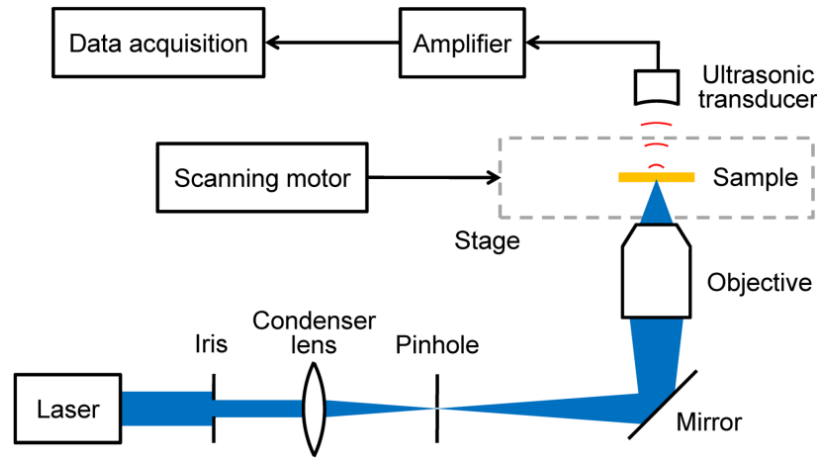
Figure 3.1 Schematic of the spectral PAM system.

Results   We used photoacoustic spectroscopy to analyze the origination of absorption around the Soret peak in fibroblasts (NIH/3T3, ATCC), the most common cells in the connective tissues of animals. Because both hemeproteins and other chromophores in cytoplasm absorb light, we analyzed the difference absorption spectrum between the oxidized and reduced states of cells, where the contributions from the chromophores other than hemeproteins were mostly removed. Most other chromophores do not have oxidized and reduced states like hemeproteins and should have approximately the same spectrum in the two states of cells. Here the hemeproteins consist of mainly cytochromes, including cytochrome c, cytochrome b, and cytochrome a,a_3 (cytochrome c oxidase), whose difference molar extinction spectra are shown in Fig. 3.2(a) (data from Ref. [83] and BORL website http://www.medphys.ucl.ac.uk/research/borl/research/NIR_topics/spectra/spectra.htm). We measured the average photoacoustic signal amplitude (normalized by the laser pulse energy) from air-oxidized and sodium-dithionite-reduced cell lysates [84], respectively, at multiple wavelengths around the Soret peak. The difference photoacoustic spectrum is shown in Fig. 3.2(b). The photoacoustic spectrum was fitted with the spectrum of a mixture of 21±12% (molar ratio, mean ± standard error) cytochrome c, 43±9% cytochrome b, and 36±4% cytochrome a,a_3. The R^2

41

was 0.98. The accuracy of this result, however, is subject to the possible presence of other neglected hemeproteins (such as cytochrome p450, nitric oxide synthases, and myeloperoxidase) with similar spectra. Then the photoacoustic spectra of the oxidized and reduced cell lysates were compared with the spectra of the calculated cytochrome mixture in the oxidized and reduced states, respectively, as shown in Fig. 3.2(c,d). It can be seen that the mixture of three types of cytochromes accounts for more than half of the optical absorption for the oxidized and reduced fibroblasts, respectively, at 420 nm wavelength (the absorption peak). The remaining absorption in the fibroblasts may originate from other sources, such as flavoproteins and nicotinamide adenine dinucleotide, and from hemeproteins that remain in the oxidized/reduced state only, which is expected because the cytochromes may not have been fully oxidized/reduced. Therefore, it is highly probable that even more absorption in the cells is in fact due to the three cytochromes.
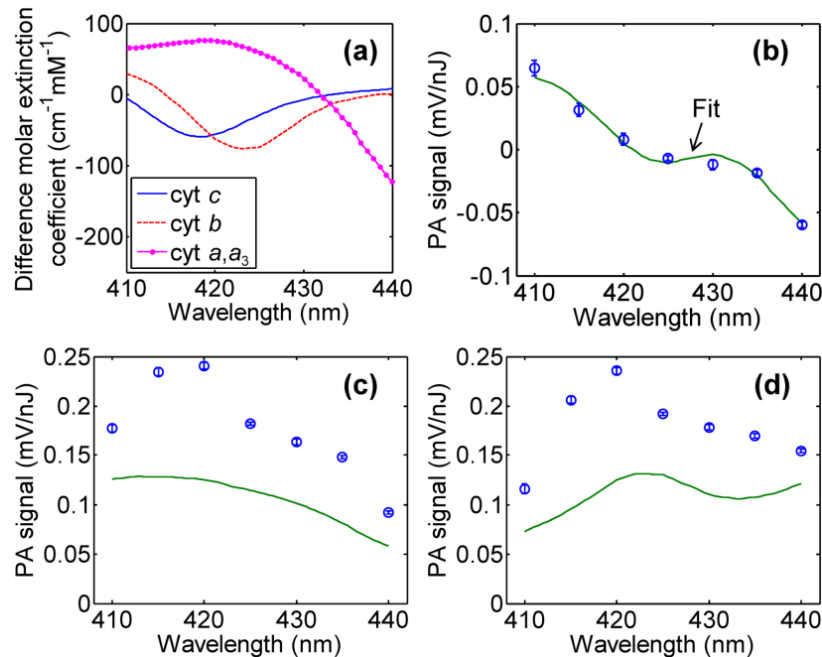
Figure 3.2 Absorption spectra. (a) Difference (oxidized – reduced) molar extinction spectra of cytochrome *c*, cytochrome *b*, and cytochrome *a*,*a₃*. (b) Difference photoacoustic (PA) spectrum of the fibroblast sample between the oxidized and reduced states. The PAM measurement (circles) is fitted with the spectrum of a mixture of 21% cytochrome *c*, 43% cytochrome *b*, and 36% cytochrome *a*,*a₃* (line). (c) PA spectrum of the oxidized fibroblast sample (circles). (d) PA spectrum of the reduced fibroblast sample (circles). The PAM measurements (circles) in (c) and (d) are compared with the spectra of the mixture (lines) in the oxidized and reduced states, respectively, according to the component concentrations calculated from (b).

42
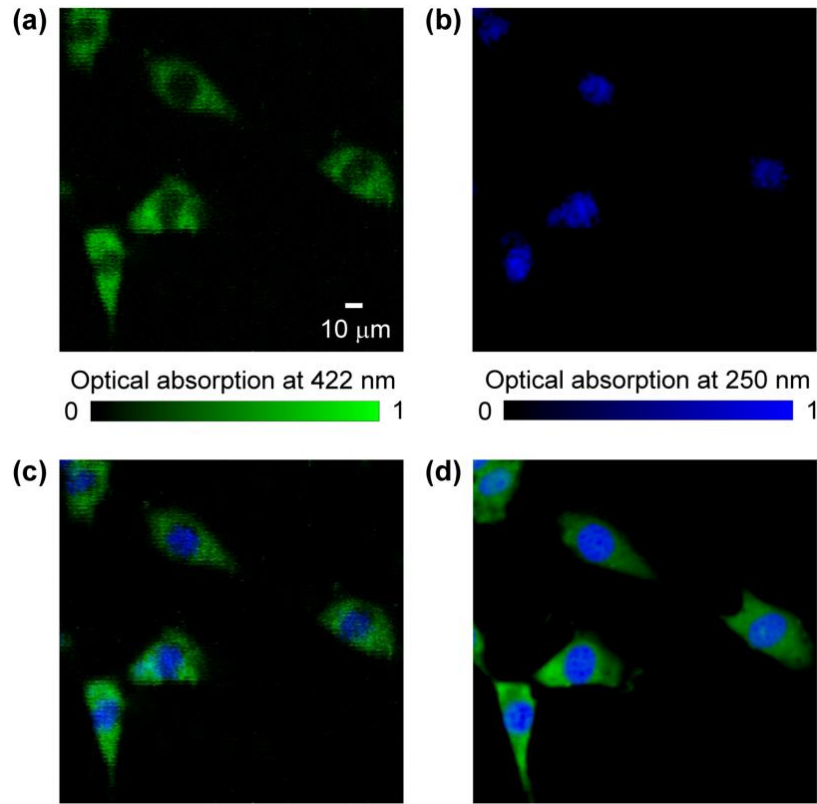
Figure 3.3 PAM and fluorescence microscopy of fibroblasts. (a) Label-free PAM image of fixed but unstained fibroblasts acquired at 422 nm wavelength. (b) Label-free PAM image acquired at 250 nm wavelength. (c) Superimposed image of (a) and (b). (d) Fluorescence microscopy image of the cells with mitochondria stained in green and nuclei stained in blue.

Next, we implemented label-free PAM of fixed fibroblasts. The fibroblasts were first maintained in Dulbecco's Modified Eagle® medium (Invitrogen) supplemented with 10% fetal bovine serum (ATCC) and 1% penicillin-streptomycin (Invitrogen). Then the cells were seeded onto quartz cover glasses (sterilized in 70% ethanol for 2 h and washed with phosphate-buffered saline) at a density of 2×10^4 cells/cm^2 and allowed to attach and spread overnight. At last the cells were fixed in 3.7% formaldehyde for 30 min and gently washed with water for the following imaging experiments. The fibroblast cytoplasms were imaged by PAM at 422 nm wavelength (where the laser provides stronger and more stable pulse energy than at 420 nm) and 200 nJ pulse energy, as shown in green in Fig. 3.3(a). The fibroblast nuclei were also imaged by PAM at 250 nm wavelength, as shown in blue in Fig. 3.3(b). Fig. 3.3(c) is a superimposed image of Figs. 3.3(a) and (b). While most cytochromes are

43

located in mitochondria, some cytochromes and other subcellular chromophores have also been identified in extramitochondrial locations. The low contrast between the mitochondria and the other parts of the cytoplasm, along with the insufficient axial resolution of PAM, caused the entire cytoplasm to be shown without individual mitochondria being resolved. As a comparison, the cells were then stained with MitoTracker® Green FM (Invitrogen) for mitochondria and 4',6-diamidino-2-phenylindole (Invitrogen) for nuclei (according to the manufacturer's instructions). The stained cells were imaged by bright-field fluorescence microscopy. The fluorescence image shown in Fig. 3.3(d) matches well with the PAM image shown in Fig. 3.3(c). Here the mitochondria were not resolved by fluorescence microscopy either, because the bright-field microscopy has insufficient axial resolution. However, individual mitochondria of many of these fibroblasts were resolved by confocal optical microscopy (not shown here) due to its finer axial resolution.

We then imaged a histological frozen section of a mouse ear by label-free PAM. The freshly excised mouse (Hsd:Athymic Nude-Foxn1^{nu}, Harlan Co.) ear was frozen rapidly to -20 ^{o}C, sectioned in parallel to the skin surface at 5 μm thickness, and fixed with acetone for 15 min. A dual-wavelength PAM image of the mouse ear section is shown in Fig. 3.4(a). The cytoplasms (imaged at 422 nm wavelength) are shown in pink, and the nuclei (imaged at 250 nm wavelength) are shown in blue. Myocytes and adipocytes can be clearly identified in the image. An optical microscopy image of the same mouse ear section with H&E staining [Fig. 3.4(b)] matches well with the unstained PAM image. Therefore, PAM has the potential for label-free high-throughput histology by imaging specific substances of interest (e.g., cytochromes, DNA, RNA, lipid, hemoglobin, and melanin) at selected wavelengths.

Discussion   We have realized label-free PAM of cytochromes in cytoplasm, along with other subcellular chromophores. The specificity of PAM to mitochondria can be further studied by imaging cells with specific subcellular mitochondrial locations and by comparing the contrast of concentrated mitochondria with that of residual cytoplasm.

44
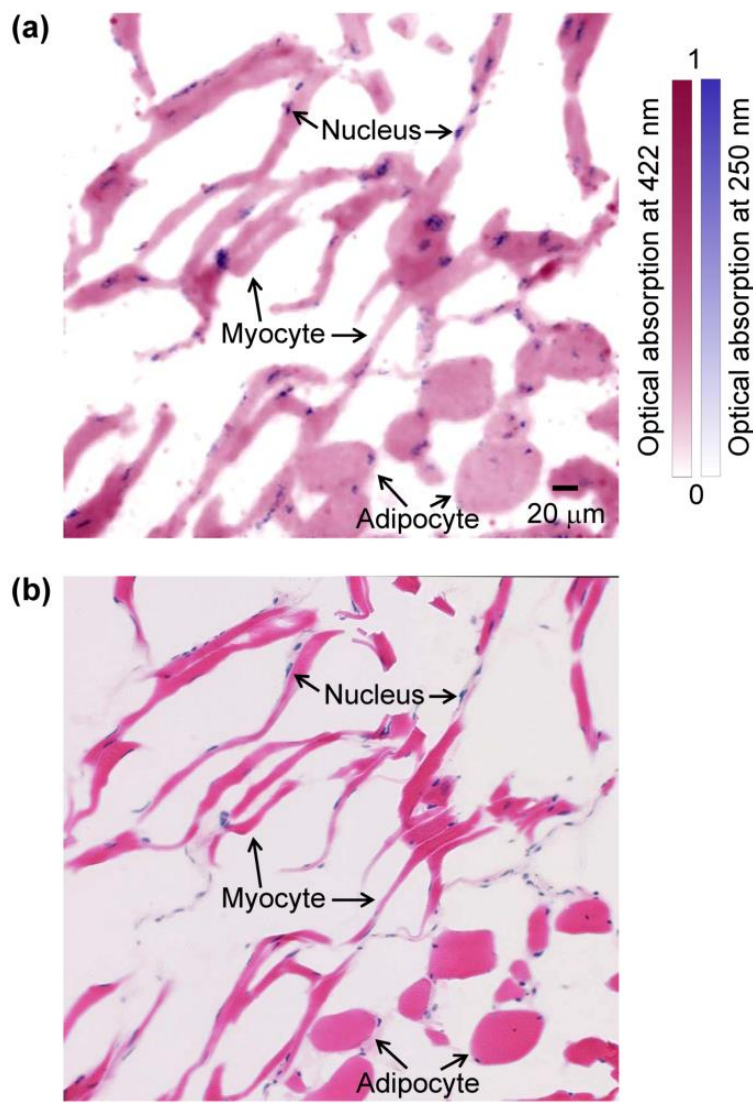
Figure 3.4 Imaging of a mouse ear section. (a) Dual-wavelength label-free PAM image. Absorption at 422 nm is shown in pink, and absorption at 250 nm is shown in blue. (b) Optical microscopy image acquired after H&E staining.

We expect to further develop label-free PAM for real-time functional imaging of live cells. The imaging speed will be increased to satisfy real-time requirements by combining a high-repetition-rate laser with laser scanning or voice-coil scanning. Also, we need to build a culture chamber for live cell imaging. With these technical developments, high-resolution functional imaging of live cells can be realized by multi-wavelength PAM, such as imaging the ratio of reduced to oxidized cytochromes, which is difficult for fluorescence microscopy. Moreover, as in hyperspectral optical imaging, PAM

45

can potentially utilize a broad range of wavelengths for simultaneous imaging of various cytochromes with good specificity.

3.2 Photoacoustic Microscopy of Myocardium

Background The heart comprises a syncytium of cardiomyocytes that are important for optimizing cardiac functions through coordinated excitation-contraction-relaxation [85]. Delineating the exact myocardial architecture is critical to understanding the exact mechanisms of cardiac functions, such as the wall thickening and the ventricular longitudinal shortening. Recently, the myocardial fibers have been found to be organized in branching layers separated by cleavages, referred to as the "sheet architecture" [85-87]. It has been reported that the systolic wall shear aligns along the sheet direction [85], and the myocardial sheet is the major infrastructure contributing to systolic wall thickening for ejection of blood [88, 89]. However, the exact three-dimensional (3-D) complex sheet architecture remains to be defined for a better understanding of cardiac mechanisms [90].

One of the difficulties in studying myocardial sheet architecture is the lack of appropriate imaging technologies. Histology is the traditional method to image the myocardial architectures. However, the fixation and slicing procedures inevitably deform the native sheet architecture, resulting in unnatural morphology. Confocal optical microscopy has been used to image the surface of a block of fixed heart tissue [86]. The deeper part of the tissue can be imaged by repeatedly removing thin layers of the surface. Although the deformation induced by slicing can be avoided by this technique, the tissue still requires fixation and staining, which dehydrate and deform the native sheet architecture. Diffusion-tensor MRI can delineate the sheet architecture nondestructively in viable hearts [88, 91]; however, it cannot provide micrometer-level resolution within applicable scan time (less than a day). Therefore, a fast high-resolution imaging technology is still required for visualizing the myocardial sheets in unfixed and unstained, and thereby undeformed, hearts.

PAM is suitable for imaging myocardial sheet architecture for the following reasons. First, PAM can achieve submicrometer lateral resolution in the optical ballistic regime (~1 mm deep), and can also

46

work in the optical diffusive regime (up to several centimeters deep) at acoustic resolution. PAM with scalable resolution and depth can provide consistent studies of the sheet architecture in hearts on various scales. Second, PAM can detect endogenous optical-absorption contrast with a 100% sensitivity without labeling the tissue [3]. The origins of signals from myocardium are expected to be myoglobin, a new PAM contrast reported here, as well as cytochromes and melanin [92-94]. In this pilot study, we implemented label-free PAM of myocardial sheet architecture.

Methods OR-PAM was applied to image myocardial sheet architecture, as demonstrated in Fig. 3.5. For spectral measurement, we used an integrated diode-pumped Q-switched laser and optical parametric oscillator system (NT242-SH, Ekspla) with a wavelength tunable from 210 nm to 2600 nm and a pulse repetition rate of 1 KHz [73]. For fast imaging, we used a Nd:YVO4 laser (SPOT 10-200-532, Elforlight), which provides a repetition rate up to 50 KHz but a fixed wavelength of 532 nm [18]. The details of the optical parts of the system can be found in the references [18, 73]. The laser pulses were focused by an optical objective (0.32 NA) to the heart muscle. The excited photoacoustic waves, with amplitudes proportional to the optical absorption density at the optical foci, were detected by an ultrasonic transducer (40 MHz central frequency, 80% bandwidth). 3D mapping of optical absorption was achieved by 2D raster scanning while the depth was converted from the arrival time of the photoacoustic signals from each scanning point. Here the lateral resolution was ~0.8 μm (at 532 nm wavelength), and the axial resolution enhanced by deconvolution was ~15 μm.
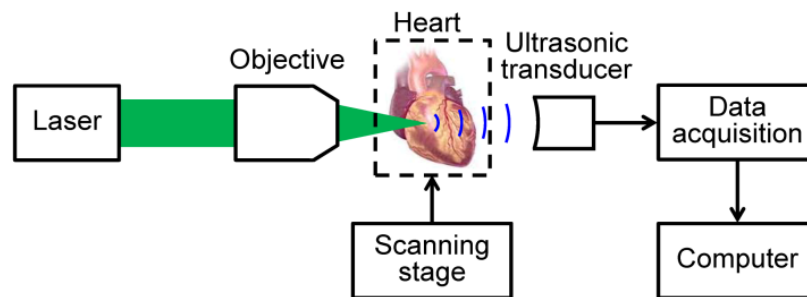
Figure 3.5 Schematic of the PAM system for myocardium imaging.

47
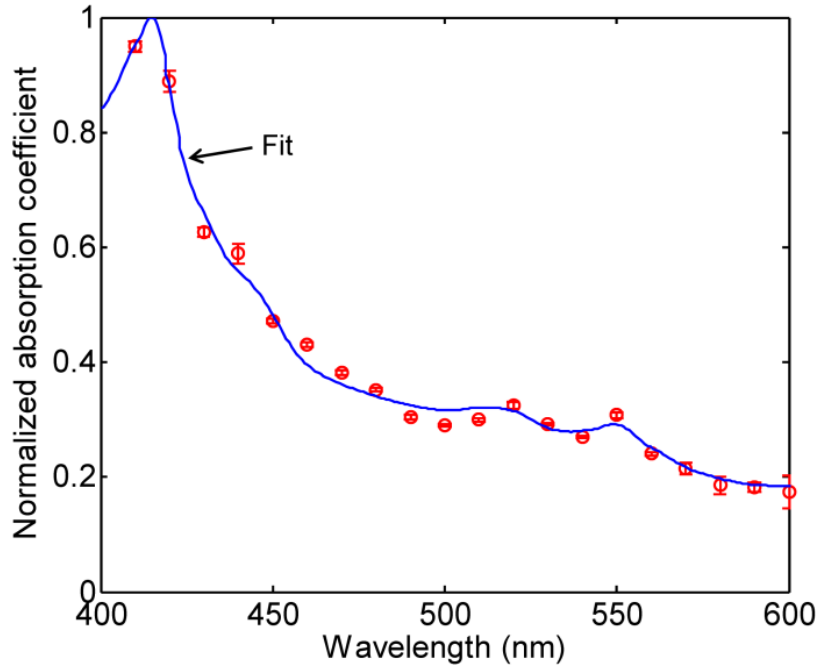
Figure 3.6 **Spectra of the absorption coefficient of the blood-free mouse myocardium. Circle: PAM measurement. Line: fit with reduced cytochrome** *c***, melanin, and metmyoglobin.**

The origins of optical absorption in heart muscles were measured quantitatively by photoacoustic spectroscopy. A mouse (Hsd:ND4, Harlan Co.) heart was saline-perfused (to wash out blood and avoid strong signals from hemoglobin), excised, and formalin-fixed. We used PAM to measure the average signal amplitude (normalized by the laser pulse energy) from the left ventricular myocardium within the wavelength range of 400–600 nm, as shown in Fig. 3.6. In the absence of hemoglobin, the main absorbers in myocardium are expected to be cytochromes (here we used the spectrum of reduced cytochrome *c* because the formalin used in heart preparation would reduce cytochrome *c* [95]), melanin, and metmyoglobin (accumulated in dead muscles) [92-94]. The PAM data can be fitted with the following linear combination of the molar absorption spectra of the main absorbers to quantify the relative concentrations of the constituents (Fig. 3.6) [80]:

$$\phi(\lambda) \propto \varepsilon_{\mathrm{cyt}}(\lambda)C_{\mathrm{cyt}} + \varepsilon_{\mathrm{mel}}(\lambda)C_{\mathrm{mel}} + \varepsilon_{\mathrm{myo}}(\lambda)C_{\mathrm{myo}}, \qquad (3.1)$$

where $\phi(\lambda)$ is the wavelength-dependent photoacoustic signal amplitude; $\varepsilon_{\mathrm{cyt}}(\lambda)$, $\varepsilon_{\mathrm{mel}}(\lambda)$, and $\varepsilon_{\mathrm{myo}}(\lambda)$ are the wavelength-dependent molar extinction coefficients of reduced cytochrome *c*, melanin, and metmyoglobin, respectively; C_{cyt}, C_{mel}, and C_{myo} are the molar concentrations of

48

reduced cytochrome c, melanin, and metmyoglobin, respectively. C_{cyt}, C_{mel}, and C_{myo} can be calculated in relative values by Eq. (3.1). The mass ratio (converted from the molar ratio) of reduced cytochrome c to melanin to metmyoglobin is 6.1 : 3.7 : 1 with a R^2 of 0.993. The accuracy of this result, however, is subject to the possible presence of other neglected absorbers (other cytochromes, oxy-/deoxy-myoglobin, lipofuscin, etc.).

We imaged a histological section of a blood-free paraffin-embedded dog heart. The unstained section (left ventricular wall area) was imaged by PAM (~50 nJ pulse energy). As shown in Fig. 3.7(a), the myocardial sheets and sheet cleavages can be identified clearly with a CNR of 41 dB between the two tissue components. These unstained structures are nearly invisible with bright-field optical microscopy due to the extremely low CNR of 4.6 dB (not shown here). The bright-field image with Masson's trichrome staining is shown in Fig. 3.7(b). The two images match well with a correlation coefficient of 0.91 when both images were thresholded at 3 times of the corresponding noise levels. Therefore, PAM can sensitively detect the endogenous absorption in myocardium with a fine resolution to resolve the sheet architecture. Moreover, it can be seen in Fig. 3.7 that the sheet architecture is deformed (e.g., the cleavage height becomes much larger than usual) due to dehydration and slicing.

With high endogenous contrast, PAM was investigated to image the unstained and unsliced heart without introducing deformation artifacts. A saline-perfused blood-free heart of a mouse (Hsd:ND4, Harlan Co.) was excised and then imaged by PAM *ex vivo* (~80 nJ pulse energy). The heart was split into halves as shown in Fig. 3.8(a); but it was unfixed and unstained and thereby undeformed. The myocardium in the left ventricular free wall, indicated by the square region in Fig. 3.8(a), was imaged by PAM. Fig. 3.8(b) shows the PAM image in MAP along the depth direction from 20 μm to 50 μm. A close-up of the marked region in Fig. 3.8(b) is shown in Fig. 3.8(c), where the branching sheets can be clearly identified with a CNR of 36 dB. Two populations of oppositely signed sheet angles were observed. The boundaries of the sheets were extracted, and the long axis (from the apex to the base of the heart) was marked [Fig. 3.8(c)]. Various morphological parameters can be calculated from this image. The average sheet angle (angle between the sheet and the ventricular short axis) is 30 ± 2 degrees, agreeing with previously reported data [88]. The average sheet thickness is 80 ± 10

49

μm, and the average cleavage height is 11 ± 1 μm, both parameters being reported, to the best of our knowledge, for the first time in an undehydrated heart.
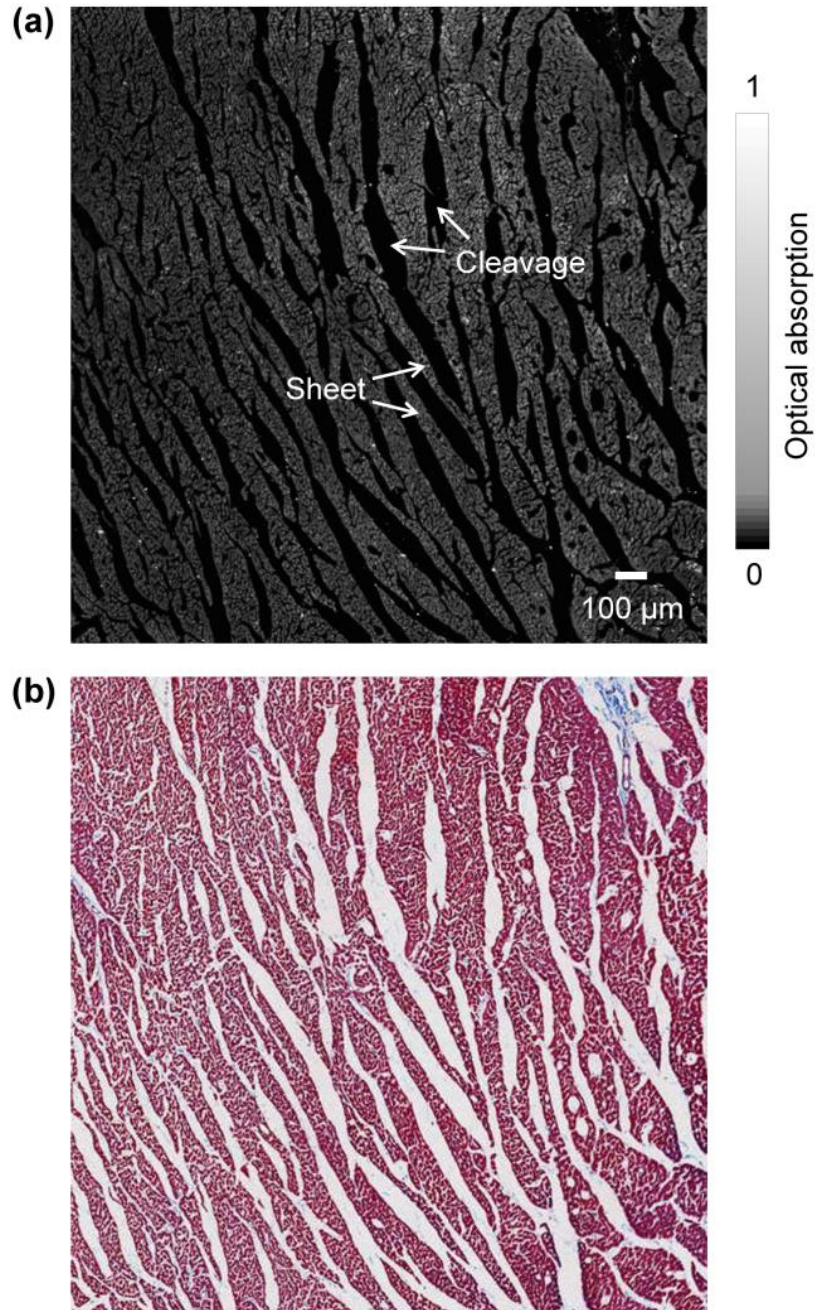
Figure 3.7 Imaging of a histological section of a dog heart in the left ventricular wall region with and without labeling. (a) Label-free PAM image. (b) Bright-field optical microscopy image with Masson's trichrome staining.

50
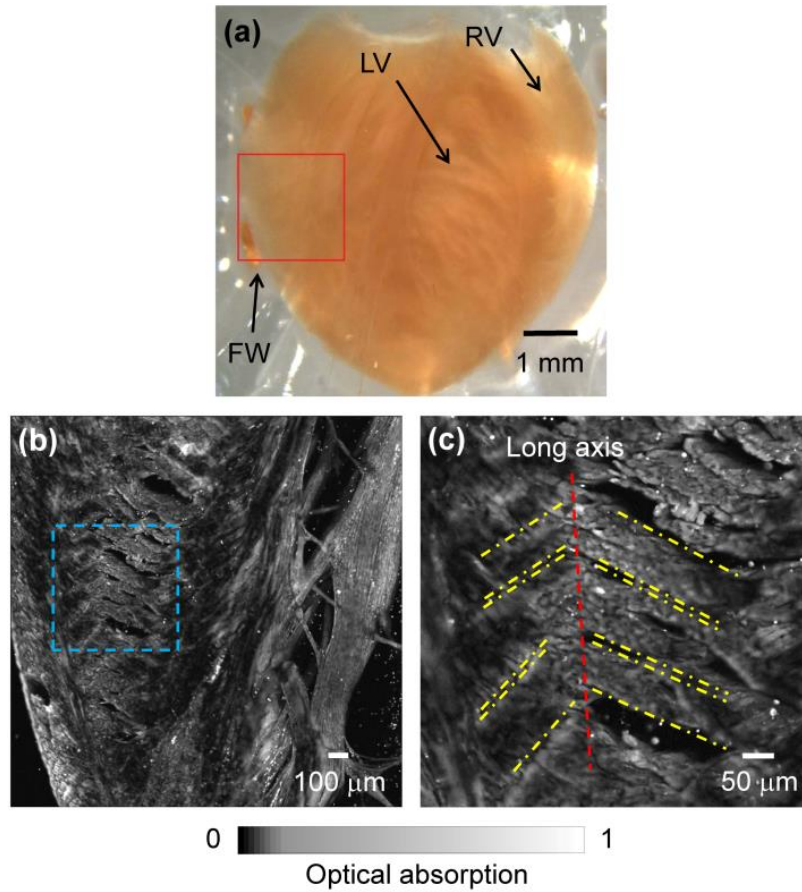
Figure 3.8 Imaging of a blood-free half-split mouse heart (unfixed and unstained). (a) Photograph of the heart. LV, left ventricle; RV, right ventricle; FW, free wall. (b) PAM image of the FW region marked in (a) acquired at 532 nm wavelength. (c) Close-up PAM image of the marked region in (b). The boundaries of the branching sheets are extracted. Red dashed line: long axis. Yellow dashed-dot line: sheet boundary.

The 3-D sheet architecture of the same heart is shown by Fig. 3.9. The heart was scanned twice, focusing at 40 μm and 100 μm depth, respectively. Fig. 3.9 shows 3D image stacks in the same area as Fig. 3.9(b) down to 150 μm in depth. As shown by the results, PAM can delineate the accurate 3D myocardial structure in unfixed and unstained hearts.

51
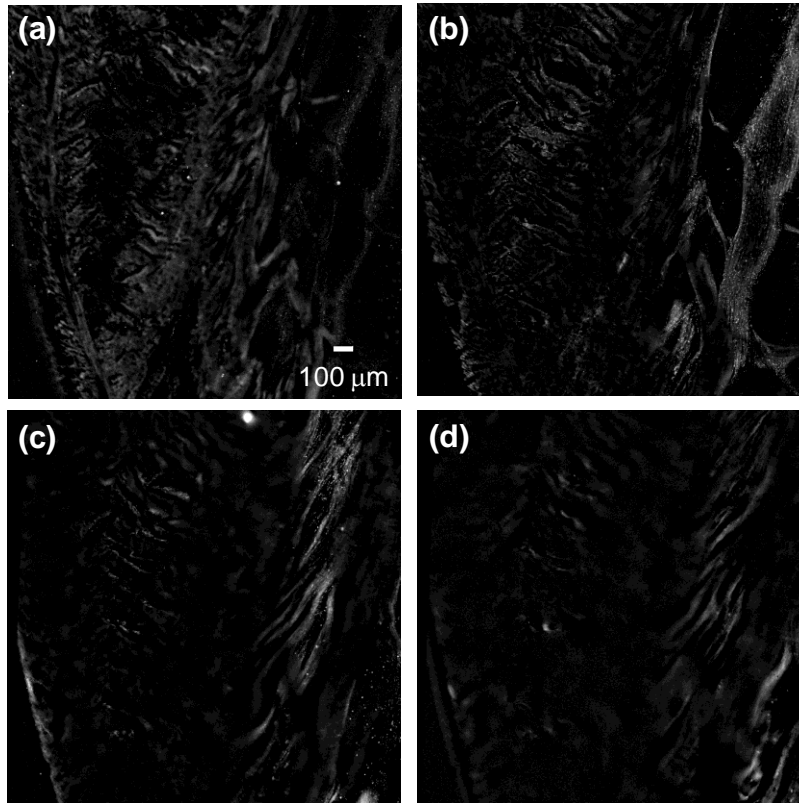
Figure 3.9 3D image stacks in the same area as Fig. 3.8(b) down to 150 μm in depth. PAM images at depths of (a) 0 μm, (b) 50 μm, (c) 100 μm, and (d) 150 μm.

Discussion Here the PAM image of the heart muscle was obscure beyond the depth of 150 μm, so the heart was split into halves in order to reveal the 3D sheet architecture. To show the sheet architecture in an intact mouse heart, we need a penetration depth of ~1 mm, which is nearly the penetration limit of OR-PAM. Near-infrared illumination and acoustic-resolution PAM can be used for the 1 mm or deeper penetration in future studies. Moreover, by further enhancing the imaging speed [35, 96], we expect to develop PAM for accessing dynamic changes of myocardial architectures in *ex vivo* perfused and viable hearts. The heart can be arrested in diastole and systole in sequence, during which the heart is imaged by PAM. The functional role of the myocardial sheets can then be analyzed.

We have realized label-free PAM of the myocardial sheet architecture in the undeformed mouse heart *ex vivo*. The sheet thickness and the cleavage height in an undehydrated heart are reported for

52

the first time. We expect to further develop PAM for the functional imaging of sheet architecture in *ex vivo* perfused and viable hearts.

3.3   Conclusions

We demonstrated cytochromes and myoglobin as new absorption contrasts for PAM, with applications in cell imaging and myocardium characterization. Moreover, although not included in this dissertation, we have shown PAM of bilirubin and myelin, with applications in jaundice diagnosis and peripheral nerve imaging [75, 76]. The exploration of endogenous light-absorbing biomolecules is still going on, in support of potential biomedical applications of multi-wavelength PAM.

By imaging DNA/RNA in cell nuclei around 250 nm wavelength and imaging cytochromes in cytoplasm around 420 nm wavelength, PAM is analogous to H&E histology. However, multi-wavelength PAM can be readily applied to intact tissue without staining. Therefore, this technique can potentially be a high-throughput substitute for H&E histology.

Chapter 4

Label-free Sectioning Photoacoustic Microscopy

This chapter describes the development of a sectioning photoacoustic microscopy system with applications in brain histology. The results are based on the advancements in spatial resolution and new contrasts for PAM, as described in previous chapters.

4.1   Sectioning Photoacoustic Microscopy

Background In biomedical imaging, nearly all techniques face a fundamental trade-off between spatial resolution and tissue penetration depth; hence, obtaining an organelle-level resolution image of a whole organ has remained a great challenge. Over the past decade, optical microscopy assisted by mechanical sectioning or chemical clearing of tissue has been demonstrated as a powerful *ex vivo* technique to overcome this dilemma, with particular interest in the imaging of the brain neural network [97-102]. Thanks to recent advances in computing power, the acquired data, typically terabytes in size, can be automatically processed to visualize the 3D neural network in a whole brain. However, all the variations of this technique need special preparation of the tissue specimen, which is technically quite difficult and hinders their potential broad applications in life sciences. For example, diffusion staining of a whole brain [98] is an extremely slow process due to the scant extracellular space in the central nervous system; electrophoretic removal of lipids in the brain [102], resulting in a transparent brain for easy staining and imaging, causes an unclear loss of biological information. Therefore, finding an imaging method applicable to minimally processed tissue, ideally fresh tissue, will facilitate the transition of whole-organ microscopy into a universal laboratory technique.

54

One potential solution is PAM, a fast developing label-free imaging method. While in an unstained piece of tissue most endogenous biomolecules do not fluoresce, all of them absorb photons at some wavelengths. Label-free PAM has demonstrated broad biomedical applications by imaging hemoglobin, melanin, DNA & RNA in nuclei, cytochromes, lipids, etc. [4, 13, 14, 18, 73] over an optical wavelength range from middle-UV to near-infrared. Moreover, PAM in reflection mode is applicable to large tissue volumes, not requiring preparation of thin tissue sections [100]. Combined with a microtome for serial removal of tissue sections, spectral PAM fits well as a tool in imaging biomolecules of interest in an unstained organ at subcellular resolution. Here, we demonstrate the first label-free sectioning photoacoustic microscopy (SPAM). SPAM uses UV light for cell nuclear imaging without staining in mouse brains, which are formalin fixed and paraffin embedded for minimal morphological deformation.

SPAM System   In SPAM (Fig. 4.1), a formalin-fixed paraffin-embedded tissue block is mounted on a specimen holder immersed in water. The specimen is automatically imaged as controlled by a computer. The x-y-z stages control both the scanning for imaging and the tissue sectioning by the microtome. The specimen is imaged on the surface, then a thin layer is shaved off and the new surface is imaged. This sequence is repeated to obtain a 3D image.

The user interface of the SPAM system is programmed in LabVIEW. After acquiring all the inputs from the user, the computer transfers all the parameters to a central controller (sbRIO-9623, National Instruments), which integrates a real-time processor (400 MHz) and a reconfigurable FPGA (field-programmable gate array). The controller triggers an Nd:YLF Q-switched UV laser (QL266-010-O, Crystalaser) to generate laser pulses at 266 nm wavelength, 7 ns pulse width, and 10 KHz repetition rate. The laser beam is focused onto the specimen immersed in water by a custom-made water-immersion UV objective (consisting of an aspheric lens, a concave lens, and a convex lens (NT49-696, NT48-674, NT46-313, Edmund Optics); Fig. 4.2) with an NA of 0.16. The excited photoacoustic waves from the specimen are detected by a custom-made ring-shaped ultrasonic transducer (42 MHz central frequency, 76% bandwidth), which has a central hole for light delivery. The signals are then amplified, digitized by a data acquisition card (installed on the computer and triggered by the controller; ATS9350, Alazar Technologies Inc.), and recorded on the computer hard disk with real time display on the computer screen. The controller also triggers the scanning stages

55

(*x* and *z* stages: PLS-85, PI miCos; *y* stage: LS-180, PI miCos), in synchronization with the laser, for point-by-point imaging of the specimen surface. By calculating the amplitude of each A-line photoacoustic signal, we obtain a 2D image of the specific optical absorption (J/m^3) of the specimen. After each surface image is acquired, the specimen, controlled by the scanning stages, is automatically sectioned by a microtome blade mounted inside the water tank. The sliced-off thin sections of the specimen float to the water surface and are confined within a specific area. The imaging and sectioning process is repeated as required. Later the serial 2D images are processed for 3D visualization.
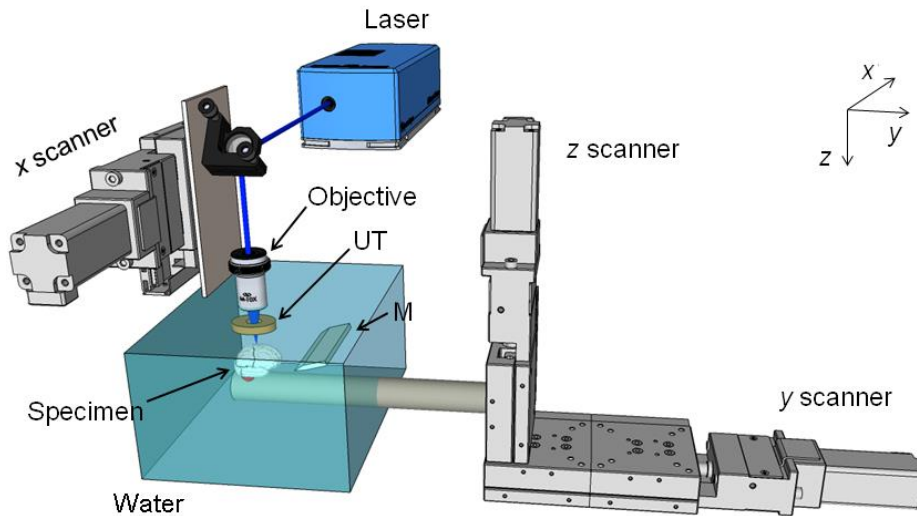
Figure 4.1   Schematic of sectioning photoacoustic microscopy (SPAM). The unstained paraffin block specimen is imaged on the surface and sectioned by the microtome, layer by layer, for 3D visualization. M, microtome; UT, ultrasonic transducer.

The system's lateral resolution is determined by the optical focusing, as in the focal plane only those biomolecules inside the optical focus are excited [18]. According to Zemax simulation, the UV objective can provide a diffraction-limited resolution as fine as 0.34 µm at 0.4 NA. But in practice the optical NA is limited to 0.16 by the size of the central hole of the ring ultrasonic transducer. Accordingly, the lateral resolution is 0.91 µm, as validated by experiments (Fig. 4.2). The axial resolution of a linear photoacoustic system is determined by the bandwidth of the ultrasonic transducer [20] (estimated as 40 µm for SPAM). However, here the signal generation from paraffin-

56

embedded specimens is likely to be highly nonlinear because the strong UV absorption is estimated to cause tens of degrees temperature rise at the optical focus [96]. So the signals are generated much more efficiently within the optical depth of focus of ~20 μm than in other regions, which agrees with the estimation of imaging depth (shown later, Fig. 4.5). Thus the axial resolution of SPAM is about 20 μm. The imaging speed is limited by the laser repetition rate to 10^4 pixels per second, and an additional ~20 seconds is required for each mechanical sectioning.
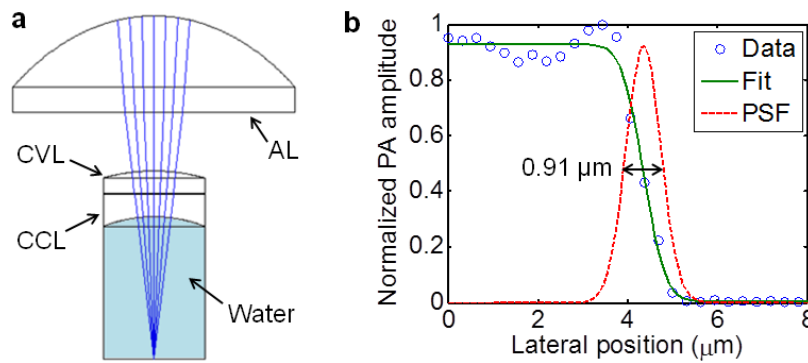
Figure 4.2 Resolution of SPAM. (a) Zemax design of the optical objective for focusing UV light into water. AL, aspheric lens; CCL, concave lens; CVL, convex lens. (b) By imaging a sharp edge and fitting the data to the error function, the system PSF, assumed to be a product of two orthogonal line-spread functions, is obtained. The lateral resolution of SPAM, defined by the FWHM of the PSF, is 0.91 μm.

Tissue preparation   The organs we used were extracted from Swiss Webster mice (Hsd:ND4, Harlan Laboratories). The brains and lungs were harvested immediately after the mice were sacrificed, and then they were fixed in 10% neutral-buffered formalin at room temperature for 5 days. Afterwards, the brains and lungs were embedded in paraffin as block specimens, and then sectioned to thin slices as required.   All experimental animal procedures were carried out in conformity with the laboratory animal protocols approved by the Animal Studies Committee of Washington University in St. Louis.

www.manaraa.com
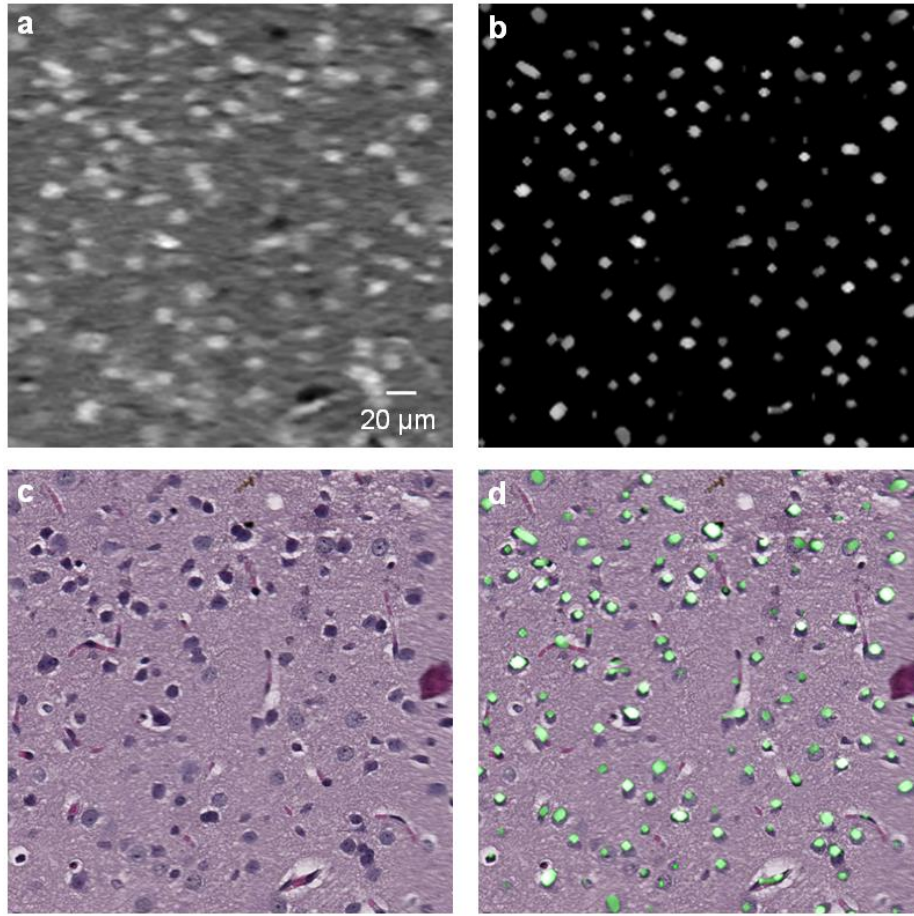
Figure 4.3 Extracting cell nuclei from SPAM images. (a) Label-free SPAM image. (b) Nuclei extracted from (a) by a Hessian filter. (c) Optical microscopy image acquired after H&E staining. (d) Superimposed image of (b) and (c), with (b) pseudo-colored in green.

Image processing   We designed a Hessian filter to extract the cell nuclei from the 2D SPAM images (Fig. 4.3). For a 2D image function $f(x,y)$, a Hessian matrix was constructed for each pixel [103]:

$$H = \begin{bmatrix} \dfrac{\partial^2 f}{\partial x^2} & \dfrac{\partial^2 f}{\partial x \partial y} \\[2mm] \dfrac{\partial^2 f}{\partial x \partial y} & \dfrac{\partial^2 f}{\partial y^2} \end{bmatrix}. \quad (4.1)$$

The two eigenvalues of H were then calculated. Negative and large eigenvalues suggest a bright and round local structure [103], i.e., a cell nucleus in our case. Hence the output image pixel value was set

58

to either the product of the two eigenvalues if both were negative, or simply to zero otherwise. Last, a slight thresholding was applied to the output nuclear image to remove excessive background.

While imaging a paraffin block, the paraffin also generates photoacoustic signals and appears as granular structures in the images. Spurious nuclei were extracted by the Hessian filter in the paraffin areas. Hence we separated tissue from paraffin automatically in the images based on the fact that tissue areas have a larger average pixel value and a smaller variation than paraffin areas. The local average and variation values were calculated for each pixel. The pixel was marked as tissue if the average was larger than an empirical threshold and the variation was smaller than an empirical threshold, or marked as paraffin otherwise. Then the spurious nuclei in the paraffin areas were removed.

The serial 2D images acquired by SPAM were converted to step-through videos by MATLAB for 3D visualization. Image co-registration is not needed because the mechanical scanning is stable and the specimen has no sectioning deformation while being imaged. 3D views of the specimen were also generated by VolVIEW.

Image analysis   To evaluate the nuclear imaging results of SPAM, H&E images were used as the gold standard. We defined nuclear sensitivity as the ratio of the number of true nuclei identified by SPAM to the number of all nuclei identified by H&E staining, defined nuclear specificity as the ratio of the area of true non-nuclear tissue identified by SPAM to the area of all non-nuclear tissue identified by H&E, and defined nuclear positive predictive value as the ratio of the number of nuclei that were true in the SPAM images to the number of all nuclei (including the spurious ones) in the SPAM images.

To generate the nuclear density map, we first generated a nuclear image by using Hessian filtering. Each nucleus in the image was reduced to one pixel with unit amplitude, and the background was set to zero amplitude. Then each pixel of this new image was replaced by the average of the 50×50 μm^2 neighborhood area, creating a nuclear density map where each pixel value equals the relative nuclear density of the 50×50 μm^2 neighborhood area.

59

4.2   Label-free Photoacoustic Brain Histology

First, we validated the system by imaging a thin section of a mouse brain (Fig. 4.4). The unstained paraffin section, fixed on a quartz slide, was imaged by SPAM and then stained with H&E for comparison. The cell nuclei in the SPAM image were enhanced by Hessian filtering and highlighted in blue.
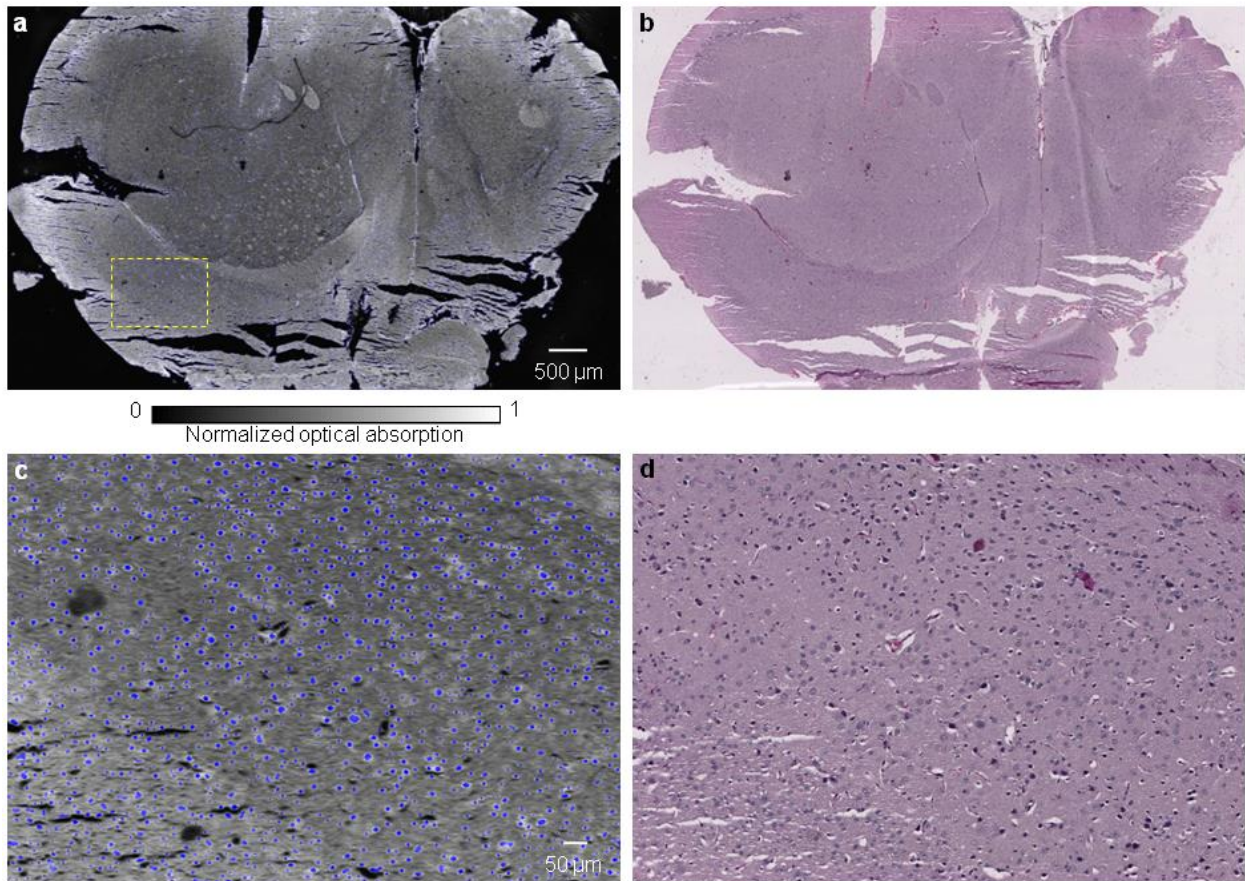
Figure 4.4 Imaging of a paraffin section of a mouse brain. (a) Label-free SPAM image, where the cell nuclei are enhanced by a Hessian filter and marked in blue. (b) Optical microscopy image acquired after H&E staining. (c,d) Close-up images of a and b, respectively, corresponding to the marked region in a. The nuclei are clearly resolved by SPAM.

The grey matter and white matter can be differentiated in the SPAM image because the former has a higher density of nuclei than the latter. The nuclei in the SPAM image matched well with those in

the H&E image. Using the H&E image as the gold standard, SPAM has a sensitivity of 93.2%, a specificity of 99.8%, and a positive predictive value of 96.7% in identifying nuclei. This experiment shows that SPAM could pinpoint cell nuclei sensitively and specifically in the mouse brain section.
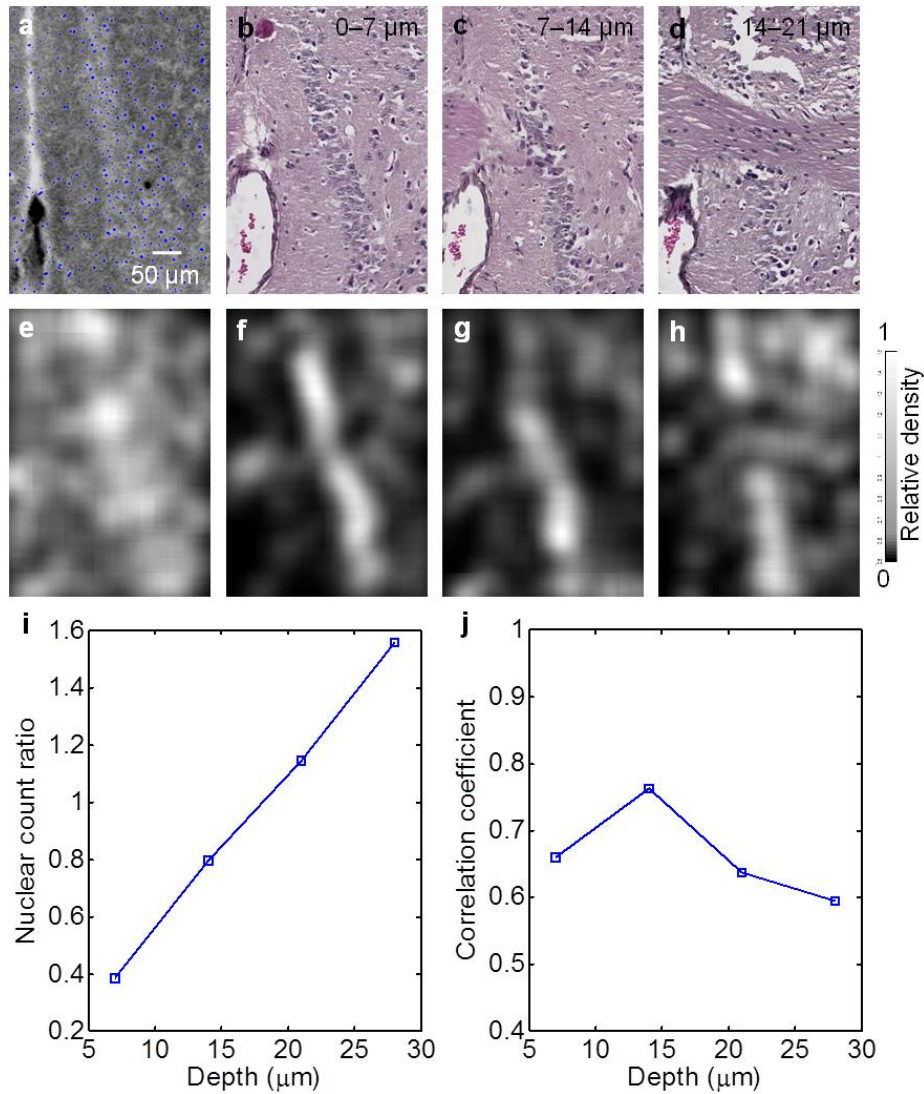
Figure 4.5 Comparison between SPAM images of a paraffin block surface and H&E images of the paraffin sections from the block surface. (a) Label-free SPAM image of the paraffin block surface with nuclei marked in blue. (b–d) H&E images of the paraffin sections that are sliced from the block surface in sequence, each with a 7 μm thickness. (e–h) Nuclear density maps of (a)–(d), respectively. (i) The ratio of the nuclear count in the H&E images within the given depth range to that in the SPAM image. (j) The correlation coefficient between the nuclear density map of the H&E images within the given depth range and that of the SPAM image.

Next, we imaged a formalin-fixed paraffin-embedded mouse brain block at the surface by SPAM (Fig. 4.5). Compared with imaging a thin section, imaging an unstained paraffin block resulted in a stronger background and, thereby, a lower image contrast for nuclei. Due to UV-light attenuation, the nuclear signal was expected to decrease exponentially with depth. To estimate the SPAM imaging depth in the block, which was related to the selection of sectioning thickness in 3D SPAM, the mouse brain block was sectioned at the surface by a standard microtome for quantitative analysis. A series of H&E images of these sections, each 7 μm thick, was obtained. Due to the deformation caused by sectioning, the nuclei in the H&E section images cannot be matched exactly with those in the SPAM block image (as we did in Fig. 4.4). However, the distributions of nuclei in the SPAM and H&E images are strongly correlated. To quantify this correlation, the nuclear count and nuclear density were calculated for these images. The ratio of the nuclear count in the H&E images within a given depth range to that in the SPAM image was calculated to be closest to unity for a depth range of 21 μm. The correlation coefficient was calculated between the nuclear density map of the H&E images within a given depth range and that of the SPAM image, with a maximum of 0.78 with a depth range of 14 μm. Here, in fact, the sensitivity of SPAM to nuclei decreases gradually, depending on both the light attenuation with depth and the absorption coefficients of different nuclei, but this phenomenon is difficult to model accurately and so is not taken into account. Given the values of the nuclear count ratio and the correlation coefficient, we estimated that SPAM images 14–21 μm deep in the paraffin block.

Last, we demonstrated the full capacity of SPAM for 3D high-resolution imaging (Fig. 4.6). The unstained mouse brain block (as used previously) was imaged on the surface and sectioned at 20 μm thickness, repeatedly, by SPAM. The imaged volume was 3.75 mm by 3.00 mm by 2.00 mm and took ~70 hours for data acquisition. The volume covered both the cerebrum and the cerebellum. Since the images were acquired at the block surface, SPAM did not present artifacts of deformed or discontinuous structures, which are common in histology (In Fig. 4.4(b), for example, deformation is especially evident at the bottom). The serial 2D images were combined into a 3D image without the need for image co-registration. Cell nuclei were shown clearly in coronal, horizontal, and sagittal views.
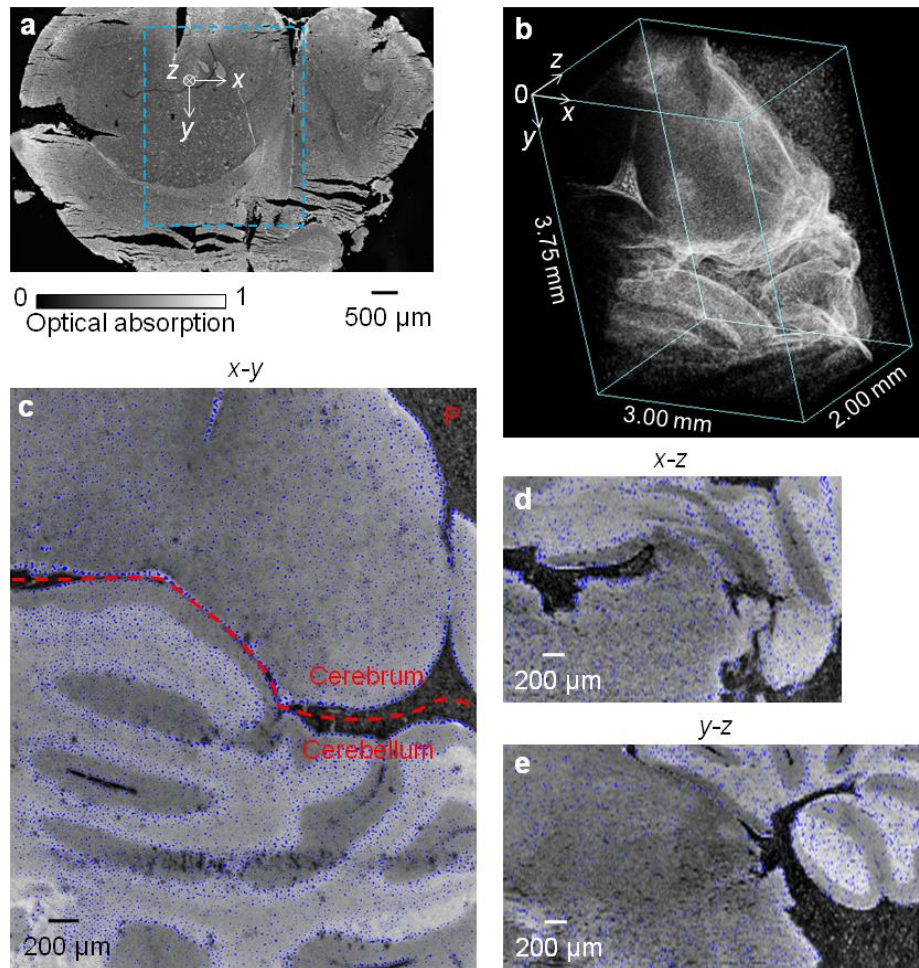
Figure 4.6 3D SPAM image of an unstained mouse brain embedded in a paraffin block. (a) A section of the entire mouse brain image (coronal view). (b) A 3D view of the imaged brain block corresponding to the marked region in a. (c) *x-y* image at *z* = 0.16 mm (coronal view), with the cell nuclei marked in blue. The boundary between the cerebrum and the cerebellum is extracted. P, paraffin. (d) *x-z* image at *y* = 2.31 mm (horizontal view). (e) *y-z* image at *x* = 0.63 mm (sagittal view).

Label-free SPAM of cell nuclei can be a high-throughput and minimal-artifact substitute for histology. Label-free SPAM (preferably with enhanced speed) facilitates rapid 3D imaging of large tissue specimens, which, for example, can be applied to identify and map tumor margins, since tumors have a larger nuclear size and an irregular nuclear shape [104]. In conventional pathology, due to the low throughput, only limited histologic examination of each specimen is performed, which may lead to incomplete information and suboptimal treatment. Moreover, label-free SPAM can be readily applied to most standard paraffin blocks used in histology, e.g., a paraffin block of a

63

mouse lung (Fig. 4.7). This is impossible with any of the current limited choices for whole-organ microscopy.
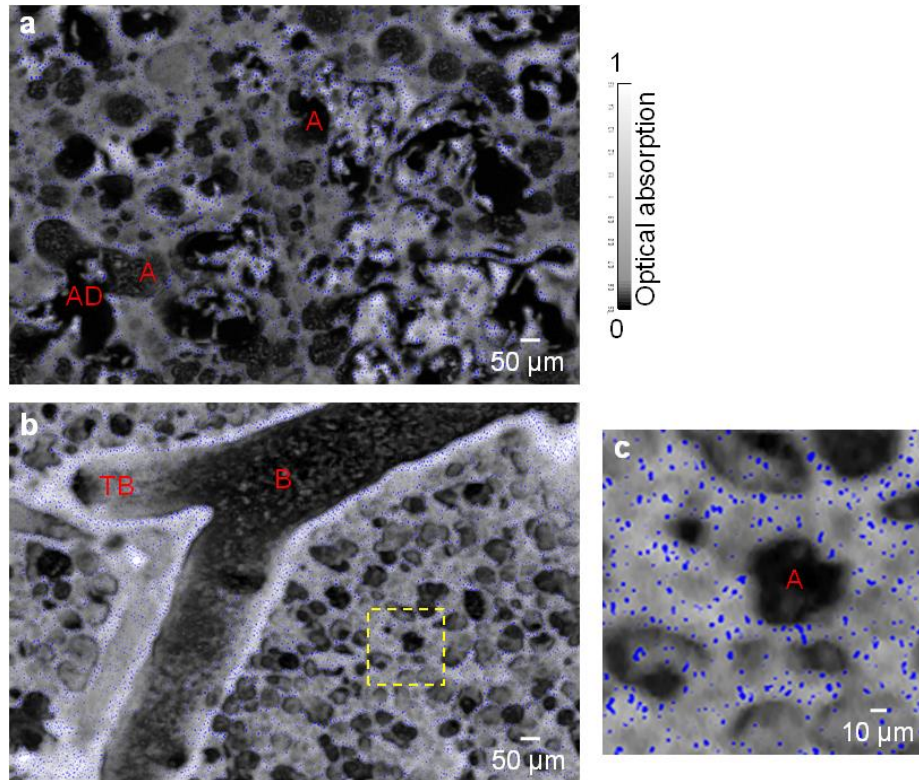
Figure 4.7 3D SPAM image of an unstained mouse lung embedded in a paraffin block. (a,b) Two *x-y* sections of the 3D image, with the nuclei marked in blue. (c) Close-up image of the marked region in b. A, alveoli; AD, alveolar duct; B, bronchiole; TB, terminal bronchiole.

SPAM is currently in the early stages of development, and significant technical improvements will be realized over the coming years. First, we have found that around 266 nm wavelength, images of fresh tissue or its frozen sections have better image contrast for nuclei over proteins than images of formalin-fixed tissue. This is likely because formaldehyde cross-links the amino groups in proteins, a change in molecular structure that may reduce the difference in characteristic UV absorption between proteins and nuclear DNA & RNA. For this reason and also for faster preparation of tissues, we plan to modify SPAM for imaging frozen tissue blocks such as those prepared for cryostats. The imaging system will be redesigned for working in a low-temperature environment, typically around –20 °C. Second, the laser repetition rate of only 10 KHz makes it too slow to image

a whole organ (e.g., a mouse brain). In our experiment, it took ~70 hours to image about one twentieth the volume of a mouse brain. By combining a fast laser [105] and a fast scanning mechanism [35] in the future, the imaging speed is expected to be increased by two orders of magnitude, i.e., achieving subcellular imaging of a whole mouse brain within one day. In addition, by implementing multiple channels using a microlens array [106], the acquisition can be accelerated by orders of magnitude more. Third, by incorporating the capability of wavelength selection in the future, SPAM has the potential to probe many more endogenous biomolecules and specific cells, such as neurons in brains, at their absorption peak wavelengths.

4.3   Conclusions

We demonstrated label-free SPAM, which acquires serial distortion-free images of a specimen on the surface. SPAM has been applied to brain histology, highlighting cell nuclei. SPAM can potentially serve as a high-throughput substitute for histology, probe many other biomolecules and cells, and become a universal tool for animal or human whole-organ microscopy, with diverse applications in life sciences.

Chapter 5

Summary and Outlook

5.1   Summary

This dissertation has described the advance of label-free OR-PAM to the subcellular scale. We realized technical advancements to improve the spatial resolution of PAM in 3D, explored light-absorbing biomolecules as new contrasts for PAM, and demonstrated label-free SPAM as a potential high-throughput substitute for histology.

In Chapter 2, we achieved 220 nm lateral resolution in transmission mode by using a 1.23 NA objective, and 0.43 μm lateral resolution in reflection mode by using a parabolic mirror design. We achieved 7.6 μm axial resolution in normal tissue with a 125 MHz ultrasonic transducer, and 5.8 μm axial resolution with silicone oil immersion/injection. With high-resolution in 3D, PAM was demonstrated to resolve cellular and subcellular structures *in vivo*, such as red blood cells and melanosomes in melanoma cells. Compared with previous PAM systems, our high-resolution PAM could resolve capillaries in mouse ears more clearly. As an example application, we demonstrated intracellular temperature imaging, assisted by fluorescence signal detection, with sub-degree temperature resolution and sub-micron lateral resolution.

In Chapter 3, we demonstrated cytochromes and myoglobin as new absorption contrasts for PAM, with applications in cell imaging and myocardium characterization. Fixed fibroblasts on slides and mouse ear sections were imaged by PAM at 422 nm and 250 nm wavelengths to reveal cytoplasms and nuclei, respectively, as confirmed by standard H&E histology. By imaging a blood-perfused mouse heart at 532 nm down to 150 μm in depth, we derived the myocardial sheet thickness (80 ±

66

10 μm) and the cleavage height (11 ± 1 μm) from an undehydrated heart for the first time. Also, without further description, we briefly introduced PAM of bilirubin and myelin, with applications in jaundice diagnosis and peripheral nerve imaging.

In Chapter 4, we developed label-free SPAM, which, assisted by a microtome, acquires serial distortion-free images of a specimen on the surface. By exciting cell nuclei at 266 nm wavelength with high resolution, SPAM could pinpoint cell nuclei sensitively and specifically in the mouse brain section, as confirmed by H&E histology. SPAM was demonstrated to generate high-resolution 3D images, highlighting cell nuclei, of formalin-fixed paraffin-embedded mouse brains without tissue staining or clearing. SPAM can potentially serve as a high-throughput and minimal-artifact substitute for histology, probe many other biomolecules and cells, and become a universal tool for animal or human whole-organ microscopy, with diverse applications in life sciences.

5.2   Outlook

We developed PAM with 220 nm lateral resolution, which is nearly the theoretical diffraction-limited resolution. However, to observe cell structures and functions on the organelle scale, better resolution is desired. Super-resolution PAM, which breaks the optical diffraction limit, is being actively developed based on nonlinear photoacoustic generation and nonlinear photobleaching, etc. [107]. Super-resolution PAM is expected to improve the lateral resolution of PAM by one order of magnitude.

We achieved 5.8 μm axial resolution for PAM, limited by the ultrasonic transducer. Further broadening the transducer bandwidth is challenging. However, the axial resolution can be potentially improved to submicron level by optical sectioning [108], as realized in confocal microscopy and two photon microscopy. Improving the 3D resolution of PAM is a pressing research interest in the photoacoustic community.

The exploration of endogenous light-absorbing biomolecules is still going on. Potential endogenous absorbers include nicotinamide adenine dinucleotide (reduced form: NADH), flavine adenine

dinucleotide (FAD), glucose, white blood cells, neurons, etc. over a broad wavelength range of absorption. To resolve these absorbers with sufficient contrast, spectral PAM covering their absorption peaks is being developed. Spectral PAM may find broad biomedical applications in life science.

Label-free SPAM may become a high-throughput substitute for histology. To resolve cell nuclei with better contrast and to prepare tissues faster, we plan to modify SPAM for imaging frozen tissue blocks, such as those prepared for cryostats. The laser repetition rate is also expected to be significantly increased for faster imaging. With these technical advancements, label-free SPAM may be applied to identify and map tumor margins, since tumors have a larger nuclear size and an irregular nuclear shape. Also, by exciting neurons with proper wavelengths, SPAM may be applied to visualize the brain neural network in 3D.

Appendix

Fast and Robust Deconvolution-based Image Reconstruction for Photoacoustic Computed Tomography in Circular Geometry

Photoacoustic computed tomography (PACT) is suitable for small animal *in vivo* imaging. In this appendix, we introduce a deconvolution-based PACT reconstruction algorithm that models the imaging process as a linear and shift-invariant system. This work has been published in IEEE Photonics Journal and Journal of the Optical Society of America A [109, 110].

Background In recent years, PACT has been successfully applied to *in vivo* blood vessel imaging and brain structural and functional imaging of small animals [10, 111]. To enable the reconstruction of 3D tissue structures in PACT, spherical, planar, and cylindrical geometries are normally used in PA signal acquisition. In most applications, they are reduced to circular and linear geometries to image a 2D tissue cross section. Linear detection geometry normally provides poorer image quality than circular geometry, because of its limited view of detection. Yet linear geometry is widely used because it is easily applicable to various tissue shapes and can lead to fast, or even real-time, imaging [112, 113] by using a linear transducer array and corresponding fast algorithms [114, 115]. Circular geometry offers full-view detection and hence good image resolution. However, imaging in such geometry is usually very slow for two reasons: the long signal acquisition time (introduced by rotating a single-element transducer around the tissue) and the large time cost of the reconstruction algorithms (either the commonly used exact back-projection algorithm [116] or the simple delay-and-sum algorithm [117]). The former can be overcome by customizing a ring-shaped transducer array [118]. But the latter, to the best of our knowledge, still remains a problem. For example, the 512-element-array-based PAT system reported in [118] can achieve real-time signal acquisition, but not real-time image formation.

A possible solution is to reduce the number of detection angles in circular geometry, which will decrease not only image reconstruction time, but also signal acquisition time or equipment cost. Nevertheless, for most algorithms the quality of the reconstructed image is strongly related to the number of detection angles. In many cases, 128 angles or fewer may result in strong artifacts in the reconstructed image. The compressed sensing algorithm can be utilized to improve image quality [119]. But this algorithm is in essence an optimization approach that requires iterative calculation, and therefore is not suitable for fast or real-time imaging.

Here we propose the deconvolution reconstruction (DR) algorithm for PACT in 3D spherical geometry and 2D circular geometry. The DR algorithm is very fast since its key step is the Fourier-based deconvolution. Moreover, the DR algorithm renders better image quality than other popular algorithms when using a small number of detection angles. Therefore, the DR algorithm promises to enable real-time imaging in circular geometry.

Theory In PACT, the relation between the illuminating light and the excited acoustic wave in an inviscid medium obeys the following wave equation:

$$\nabla^2 p(\mathbf{r},t) - \frac{1}{c^2}\frac{\partial^2}{\partial t^2} p(\mathbf{r},t) = -\frac{\beta}{C_p} A(\mathbf{r})\frac{\partial I(t)}{\partial t}, \quad (A.1)$$

where $A(\mathbf{r})$ is the absorbed energy density, $p(\mathbf{r},t)$ is the excited acoustic pressure, $\mathbf{r}$ is the 3D position vector, t is the time, $I(t)$ is the illumination pulse function, c is the sound speed, β is the coefficient of volumetric thermal expansion, and C_p is the specific heat. $I(t)$ is usually assumed to be a delta function, and c is assumed to be constant. PA signals are detected along a sphere, defined by $\mathbf{r}_d$, whose radius is r_d and whose center is the origin. Then, by using Green's functions, the detected PA signal $p(\mathbf{r}_d,t)$ can be expressed as

$$p(\mathbf{r}_d,t) = \frac{\beta}{4\pi C_p}\frac{\partial}{\partial t}\oiint_{|\mathbf{r}'-\mathbf{r}_d|=ct}\frac{A(\mathbf{r}')}{t}\mathrm{d}^2\mathbf{r}'. \quad (A.2)$$

In practical experiments, each detected signal is convolved by both the illumination pulse and the transducer impulse response. We can get a better estimation of $p(\mathbf{r}_d,t)$ by deconvolving the signal if

70

the impulse response is known and the signal-to-noise ratio is sufficiently high. Then image reconstruction is an inverse problem of calculating $A(\mathbf{r})$ from $p(\mathbf{r}_d, t)$, solved algorithmically.

The basic idea of the DR algorithm is to construct a 3D system. When the system input is $A(\mathbf{r})$, the output will be a 3D space function that is related to $p(\mathbf{r}_d, t)$. By reasonable design, this system can be constructed to be linear and shift-invariant. Then $A(\mathbf{r})$ can be calculated by deconvolution.

Let us define

$$S(\mathbf{r}_d, t) = \left[\int_0^t p(\mathbf{r}_d, t)\mathrm{d}t \right] \cdot t . \quad \text{(A.3)}$$

Substituting Eq. (A.2) into Eq. (A.3) leads to

$$S(\mathbf{r}_d, t) = \eta \oiint_{|\mathbf{r}'-\mathbf{r}_d|=ct} A(\mathbf{r}')\mathrm{d}^2\mathbf{r}', \quad \text{(A.4)}$$

where $\eta = \beta / (4\pi C_p)$.

In order to construct the linear and shift-invariant system, we start by constructing the system output from $p(\mathbf{r}_d, t)$ when the input is $A(\mathbf{r})$. The output function $C(\mathbf{r})$ is constructed as

$$C(\mathbf{r}) = S\left(\frac{\mathbf{r}}{|\mathbf{r}|} \cdot r_d, t_{\max} - \frac{|\mathbf{r}|}{c} \right), \quad \text{(A.5)}$$

where $t_{\max}$ is an adjustable parameter. PA signals during time $0 - t_{\max}$ are used to construct $C(\mathbf{r})$. In order to cover the major information in PA signals, normally it should satisfy that $ct_{\max} \geq 2r_d$. $C(\mathbf{r})$ is zero when $|\mathbf{r}| > ct_{\max}$. Substituting Eq. (A.4) into Eq. (A.5) leads to

$$C(\mathbf{r}) = \eta \oiint_{\Omega} A(\mathbf{r}')\mathrm{d}^2\mathbf{r}', \quad \text{(A.6)}$$

where the integral surface Ω can be expressed as

$$\left| \mathbf{r}' - \frac{\mathbf{r}}{|\mathbf{r}|} \cdot r_d \right| = ct_{\max} - |\mathbf{r}| . \quad \text{(A.7)}$$

Considering that the detected tissue is contained by the sphere $\mathbf{r}_d$, $A(\mathbf{r}')$ has nonzero values only if $|\mathbf{r}'| < r_d$ (which means $A(\mathbf{r}')$ needs to be integrated only over Ω within this region). Further,

71

$2|\mathbf{r}'| < ct_{\max} - r_d$ if $ct_{\max}$ is greater than $3r_d$ or the tissue volume is relatively small. If each ultrasonic detector receives photoacoustic signals within a sufficiently small solid angle, Eq. (A.7) can be approximated to the following surface by using the Taylor series expanded to the first order [110]:

$$|\mathbf{r}' - \mathbf{r}| = ct_{\max} - r_d. \qquad (A.8)$$

The smaller the maximum of $|\mathbf{r}'|$ is, the smaller the ignored higher-order Taylor polynomials. In other words, a smaller tissue volume in comparison to the detection radius results in less error. Thus, Eq. (A.6) can be approximated as

$$C(\mathbf{r}) = \eta \oiint_{|\mathbf{r}'-\mathbf{r}|=ct_{\max}-r_d} A(\mathbf{r}') d^2\mathbf{r}'. \qquad (A.9)$$

The constructed system as described by Eq. (A.9) can be easily shown to be linear and shift-invariant. In other words, if $A(\mathbf{r}')$ is shifted spatially by $\Delta\mathbf{r}$, the response $C(\mathbf{r})$ will be shifted by the same distance in the same direction because $|\mathbf{r}' - \mathbf{r}| = ct_{\max} - r_d$ must hold. Therefore, Eq. (A.9) can be rewritten as

$$C(\mathbf{r}) = A(\mathbf{r}) * h(\mathbf{r}), \qquad (A.10)$$

where $h(\mathbf{r})$ is the system impulse response—the response of the constructed system to a point photoacoustic source located at the origin—and $*$ represents 3D convolution. When the system input is the 3D delta function, $h(\mathbf{r})$ is the system output:

$$h(\mathbf{r}) = \eta \oiint_{|\mathbf{r}'-\mathbf{r}|=ct_{\max}-r_d} \delta^3(\mathbf{r}') d^2\mathbf{r}' \qquad (A.11)$$

or

$$h(\mathbf{r}) = \eta \delta(|\mathbf{r}| - ct_{\max} + r_d). \qquad (A.12)$$

Based on Eq. (A.10), $A(\mathbf{r})$ can be calculated by a simplified Wiener deconvolution method [120]:

$$\tilde{A}(\boldsymbol{\omega}) = \frac{\tilde{C}(\boldsymbol{\omega})}{\tilde{h}(\boldsymbol{\omega}) \cdot \left(1 + \lambda \Big/ \left|\tilde{h}(\boldsymbol{\omega})\right|^2\right)}, \qquad (A.13)$$

where $\tilde{A}(\boldsymbol{\omega})$, $\tilde{h}(\boldsymbol{\omega})$, and $\tilde{C}(\boldsymbol{\omega})$ are the 3D Fourier transforms of $A(\mathbf{r})$, $h(\mathbf{r})$, and $C(\mathbf{r})$, respectively; and λ is a constant (adjustable according to applications).

72

To summarize, the DR algorithm consists of two steps: first, construct $C(\mathbf{r})$ based on Eqs. (A.3) and (A.5); second, calculate $A(\mathbf{r})$ by Eq. (A.13). It is worth noting again that DR is an approximate algorithm because Eq. (A.9) is approximated from Eq. (A.6). Smaller tissue volumes in comparison to the detection radius result in less error. It has also been shown that the optimal value of t_{max} is $2r_d/c$ (as used in the following experiments), where DR provides the fastest calculation while maintaining good image quality [110].

Physical meaning The physical meanings of the key formulas in this DR algorithm are explained here. The function $S(\mathbf{r}_d, t)$, defined in Eq. (A.3), can be understood as the processed time-domain PA signal, which is proportional to the velocity potential multiplied by the time of arrival. It is due to the integration of $A(\mathbf{r})$ over a spherical shell, as shown in Eq. (A.4). Then $S(\mathbf{r}_d, t)$ is transformed to $C(\mathbf{r})$ by Eq. (A.5). The value of $C(\mathbf{r})$ at position $\mathbf{r}$ corresponds to the signal S processed from the pressure p received by the $\mathbf{r}$-direction transducer, located at position $\mathbf{r} \cdot r_d / |\mathbf{r}|$, at time $\left(ct_{max} - |\mathbf{r}|\right)/c$. In other words, the value of $C(\mathbf{r})$ at position $\mathbf{r}$ corresponds to the tissue lying on a spherical surface whose center is $\mathbf{r} \cdot r_d / |\mathbf{r}|$ and whose radius is $ct_{max} - |\mathbf{r}|$, as shown in Fig. A.1. This transformation allows us to merge two variables $\left(\mathbf{r}_d, t\right)$ into a single variable $\mathbf{r}$.

According to Eq. (A.10), $C(\mathbf{r})$ approximates to the convolution of $A(\mathbf{r})$ and $h(\mathbf{r})$ when each acoustic detector receives PA signals within a narrow cone. As shown in Eq. (A.12), $h(\mathbf{r})$ approaches infinity on the sphere whose center is the origin and whose radius is $ct_{max} - r_d$, and equals zero at other places. Based on the characteristics of the delta function and the origin-symmetric shape of $h(\mathbf{r})$, it is easy to derive that $A(\mathbf{r}) * h(\mathbf{r})$ at position $\mathbf{r}$ equals to the integration of $A(\mathbf{r})$ over a sphere whose center is $\mathbf{r}$ and radius is $ct_{max} - r_d$, as shown in Fig. A.1.

73
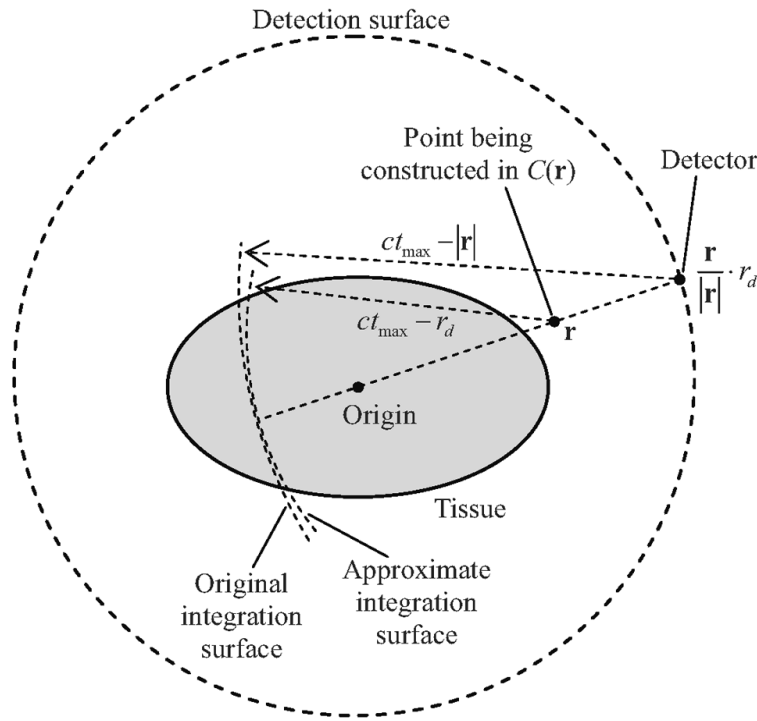
Figure A.1 Illustration of detection geometry and photoacoustic signal integration.

In short, $C(\mathbf{r})$ and $A(\mathbf{r}) * h(\mathbf{r})$ correspond to integrations on two spherical surfaces that do not perfectly overlap, and thereby only approximately equal. This misalignment is the physical origin of the error in the DR algorithm. It is also worth mentioning that these two spheres are tangential on the acoustic axis of each acoustic detector in the direction of $-\mathbf{r}$ (or $\mathbf{r}$). If the tissue volume is relatively small, the mismatch between these two spheres within the tissue will also be small, and so will be the error of this DR algorithm. This explanation is consistent with the conclusion of the previous mathematical derivation.

While the integration spherical surface of $C(\mathbf{r})$ has a radius of curvature dependent on variable $\mathbf{r}$, the integration spherical surface of $A(\mathbf{r}) * h(\mathbf{r})$ has a constant radius of curvature once $t_{\max}$ is set. We can exactly match the approximate spherical surface with the original spherical surface at one position. If the tissue volume is centered within the detection surface, it is reasonable to set the matching position at the origin by choosing $ct_{\max} = 2r_d$.

74

One can further approximate the integration spherical shells to planes orthogonal to the acoustic axis [121], which is tantamount to a zero-order Taylor expansion of the cosine function of the acoustic detection angle. Although such an approximation reduces the spherical Radon transform to the planar counterpart, errors in the reconstructed images can be severe unless the tissue volume is extremely small.

Algorithm implementation   Here we describe how to implement the DR algorithm in the most common 2D applications, where PA signals are detected along a circle. The transducer used here should receive signals from the focal plane and reject out-of-plane signals. In this case, the convolution in Eq. (A.10) will approximately hold true in the 2D case ($\mathbf{r}$ is reduced to a 2D position vector).

During detection, the generated acoustic signal $p(\mathbf{r}_d, t)$, in which $\mathbf{r}_d$ is reduced to follow a circle, is sampled in both the space and time domains. Thus, the detected $p(\mathbf{r}_d, t)$ can be represented by an $N_a \times N_t$ matrix, where N_a is the number of detection angles and N_t is the number of sampled time points at each detection angle. Also, $S(\mathbf{r}_d, t)$ is represented by an $N_a \times N_t$ matrix.

Suppose we want to reconstruct an image with the resolution of $N \times N$ (stored as an $A(\mathbf{r})$ matrix), which represents a spatial size of $a \times a$ (located at the center of the detection circle). $h(\mathbf{r})$ can be represented by a matrix corresponding to the spatial size of $2r_d \times 2r_d$ (here, $ct_{max} = 2r_d$). Since the $A(\mathbf{r})$ matrix and $h(\mathbf{r})$ matrix will be convolved, each of their elements should represent the same discrete space interval. So $h(\mathbf{r})$ should be constructed as a $(N \cdot 2r_d / a) \times (N \cdot 2r_d / a)$ matrix, and $C(\mathbf{r})$, the convolution of $A(\mathbf{r})$ and $h(\mathbf{r})$, should be constructed as a $[N \cdot (2r_d / a + 1) - 1] \times [N \cdot (2r_d / a + 1) - 1]$ matrix. While calculating an element in the $C(\mathbf{r})$ matrix, the spatial coordinate of this element is transformed to the corresponding coordinate in the $S(\mathbf{r}_d, t)$ matrix, and then the value of the nearest $S(\mathbf{r}_d, t)$ element is chosen (bilinear interpolation can be used for better accuracy at the cost of computation time). After all the elements of the $C(\mathbf{r})$ matrix are calculated, the $A(\mathbf{r})$ matrix, namely, the to-be-reconstructed image, can be obtained by using deconvolution.

75

The main steps in the DR algorithm are constructing $C(\mathbf{r})$ and deconvolution. To speed up the algorithm, $h(\mathbf{r})$ and the relationship between the variables of $C(\mathbf{r})$ and $S(\mathbf{r}_d, t)$ can be precalculated. The size of the $C(\mathbf{r})$ matrix is on the order of N^2, so constructing $C(\mathbf{r})$ has a time complexity of $\Theta(N^2)$. The deconvolution step involves fast Fourier transformation (FFT), division in the frequency domain, and inverse fast Fourier transformation (IFFT). The time complexity of the division is $\Theta(N^2)$, and that of both FFT and IFFT is $\Theta(N^2 \log N)$. Thus, in total, the DR algorithm has a time complexity of $\Theta(N^2 \log N)$.

In comparison, back-projection algorithms and the delay-and-sum algorithm, two kinds of commonly used time-domain algorithms, add up all the N_a detected signals (with or without processing in the time domain) at each pixel of reconstructed image. So, they have a time complexity of $\Theta(N_a N^2)$. Considering that N_a is normally of the same order as N for good image quality, the time complexity of these algorithms can be written as $\Theta(N^3)$. Therefore, the DR algorithm is much faster than back-projection algorithms and the delay-and-sum algorithm, especially when reconstructing high-resolution images. Moreover, as far as we know, the available frequency-domain algorithms for circular geometry either use a similar projection strategy [116] as these time-domain algorithms or calculate $\tilde{A}(\omega)$ based on Bessel and Hankel functions [122]. They are even more time-consuming and in fact rarely used in practice.

Results   The DR algorithm was applied to *in vivo* mouse brain imaging. The head of a mouse was depilated and then imaged with intact skull and skin. The experimental setup is shown in Fig. A.2. The Nd:YAG laser (LOTIS II LS-2137/2) generated pulses with a wavelength of 532 nm, a width of 16 ns and a repetition rate of 10 Hz. PA signals were received by a 512-element cylindrically-focused circular transducer array whose diameter was 5 cm. The center frequency of the transducer was 5 MHz, and the bandwidth was greater than 80%. The signals were amplified, sampled at 40 MHz, and transferred to a computer for processing by the signal acquisition system.
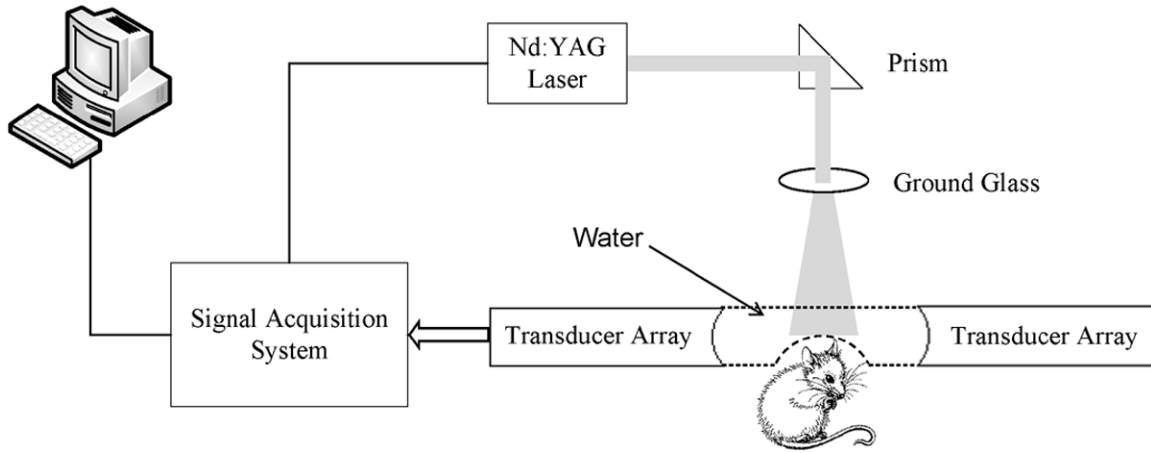
Figure A.2 Experimental setup of PACT.

The received PA signals (after deconvolving the transducer impulse response) are shown in Fig. A.3(a). The two axes denote time and detection angle; the grayscale denotes normalized signal amplitude. The constructed space function $C(\mathbf{r})$ (also normalized) in the DR algorithm is shown in Fig. A.3(b). Here the parameter t_{max} is set to $2r_d/c$, and only the signals during 10–33 μs are used.

Figures A.4(a) and A.4(b) show the images reconstructed by the exact back-projection algorithm [116] and the DR algorithm, respectively, when signals from all 512 detection angles are used. Then we tested the robustness of these two algorithms by reducing the number of angles uniformly around the detection circle. Figures A.4(c) and A.4(d) show the images reconstructed over 128 angles (selected every fourth one from the 512 angles). Figures A.4(e) and A.4(f) show the images reconstructed over 64 angles. For comparison, we opened the skin of the mouse brain after PA imaging and took a photograph of the cerebral cortex [Fig. A.4(g)].

When reconstructed over 512 angles, the results of both algorithms are nearly identical and agree well with the photograph. The DR algorithm outperforms the back-projection algorithm when using signals from fewer angles. It can be seen that the reconstructed image of the DR algorithm over 128 angles is as good as the image reconstructed over 512 angles, while the back-projection algorithm's result suffers from many vessel-like artifacts. When reconstructed over 64 angles, the image from the

77

back-projection algorithm has very strong vessel-like artifacts that obscure real vessels. The image from the DR algorithm is blurred but generally better.
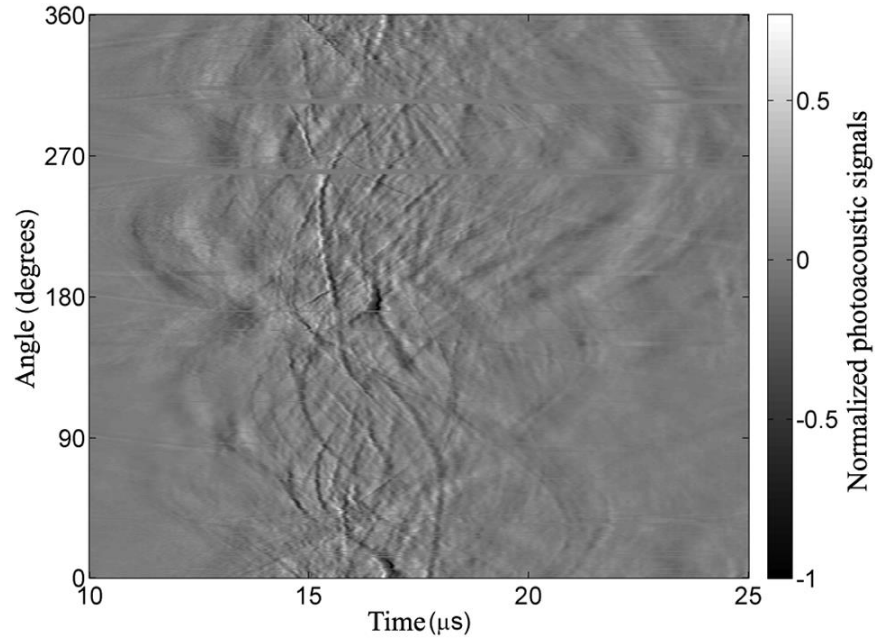
(a)
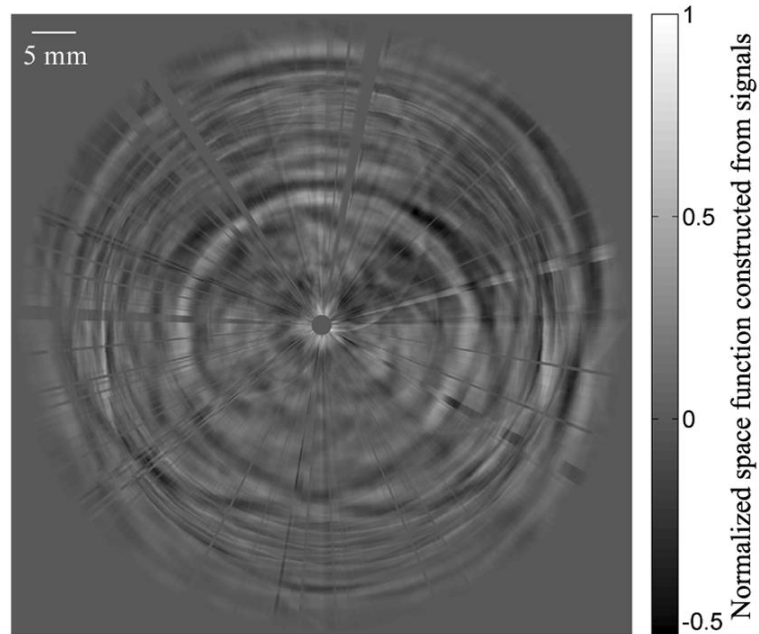
(b)

Figure A.3 Received photoacoustic signals (a) and constructed space function $C(r)$ (b).
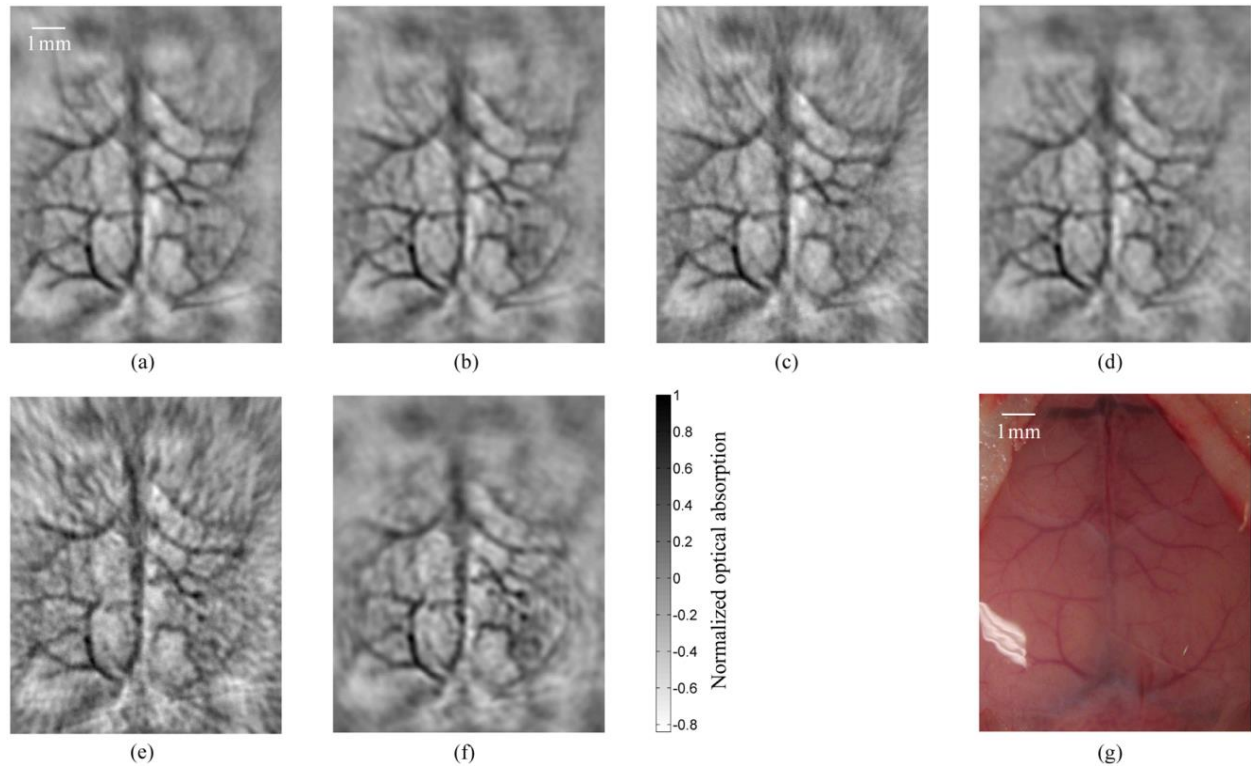
Figure A.4 *In vivo* **and noninvasive reconstructed images using (a) back-projection over 512 angles, (b) deconvolution reconstruction over 512 angles, (c) back-projection over 128 angles, (d) deconvolution reconstruction over 128 angles, (e) back-projection over 64 angles, (f) deconvolution reconstruction over 64 angles. (g) Photograph of the mouse cerebral cortex taken after imaging.**

To compare the speeds of the back-projection and DR algorithms, we reconstructed images of a 2×2 cm^2 region (at the center of the transducer array) with different numbers of pixels. In practical applications, we reconstruct images with more pixels if we can achieve better spatial resolution, otherwise adding pixels is meaningless because the added pixels contain little new spatial information. Moreover, more detection angles are normally required for better spatial resolution. Therefore, in order to investigate the calculation efficiencies of these two algorithms with different requirements of spatial resolution, the number of detection angles and the pixel resolution of reconstructed images in our calculation were varied simultaneously. In other words, we used signals from N detection angles to reconstruct an $N \times N$ image and recorded the time cost of each algorithm (Intel Core2 Duo CPU @ 3.00GHz, Matlab R2009a), where N was chosen to vary from 64, 128, 256, to 512. The results are shown in Fig. A.5.
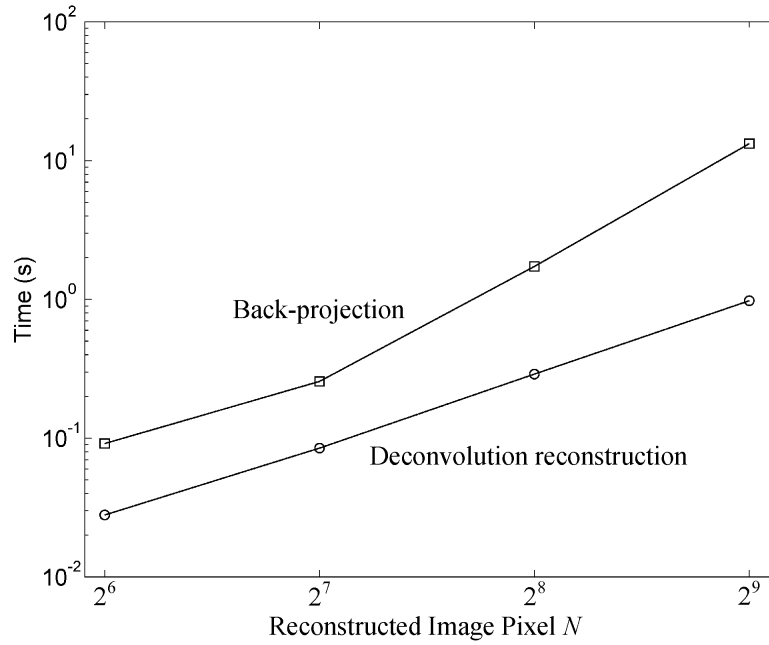
Figure A.5 Time costs of the back-projection algorithm and deconvolution reconstruction algorithm when reconstructing $N \times N$ images using signals from N detection angles.

It can be seen that the time cost of the DR algorithm is much smaller than that of the back-projection algorithm. For each algorithm, the trend of increased time cost with N is consistent with the time complexity analysis. When $N = 512$, the DR algorithm is about ten times faster than the back-projection algorithm. It can be predicted that the speed advantage of the DR algorithm is greater when $N > 512$. Moreover, according to these data, real-time imaging is possible only if $N \leq 256$ (in our system) if the DR algorithm is used. Since the DR algorithm presents stronger robustness for sparse detection angles, it should be preferably considered for real-time PA imaging in circular geometry.

Discussion   The exact back-projection algorithm uses an inverse formula, which ideally requires knowledge of the detected signals at every position of the detection circle. But in practice one can detect signals from only a limited number of angles. The back-projection algorithm does not project the undetected signals by assuming them to be zero. This assumption is in fact not true, and it introduces large errors if detection angles are sparse. In contrast, the DR algorithm is based on a

80

valid forward model given by Eq. (A.10). The effectiveness of this forward model will not be affected by the number of detection angles. In fact, in $C(\mathbf{r})$ only the elements perfectly matching with the measurement points are exactly known. If the detection angles are too sparse, this model will be ill-conditioned and lead to unstable solutions. But it is a better starting point than an invalid inverse formula. Moreover, the DR algorithm's forward model is based on convolution, which can be directly and quickly solved using a deconvolution method without iterative calculations normally included in most forward-model-based methods. In our deconvolution, the unmeasured elements in $C(\mathbf{r})$ are estimated by the detected signals. The solution is not a least-squares one, but is close to.

The DR algorithm assumes, as mentioned above, that the object dimension is relatively small compared to the detection circle. In our experiment, the cross section of the mouse head is approximately elliptically shaped with a major axis of 2 cm, which is not much less than the detection diameter (5 cm). However, most vessels are within a 0.6×0.8 cm^2 region, roughly centered within the detection circle, and are clearly imaged. In practice, if an object is so large that the DR algorithm cannot reconstruct the full cross section clearly, we can limit the region of interest at the detection center for better image quality.

Conclusions We derived the DR algorithm theoretically and validated it experimentally. The DR algorithm uses a convolution-based forward model, which is more effective than the inverse formula for sparse detection angles. Moreover, this model can be quickly solved by using a deconvolution-based method. When designing a real-time PACT system, the number of detection angles cannot be very large, and the image reconstruction algorithm should be fast, so the DR algorithm becomes a good choice. In addition, by utilizing the DR algorithm in PACT systems, we can use fewer measurements for given image quality, thereby reducing experimental cost.

References

1.	Bell, A.G., *On the production and reproduction of sound by light.* Am. J. Sci., 1880. **20**: p. 305-324.

2.	Wang, L.V. and S. Hu, *Photoacoustic Tomography: In Vivo Imaging from Organelles to Organs.* Science, 2012. **335**(6075): p. 1458-1462.

3.	Wang, L.V., *Multiscale photoacoustic microscopy and computed tomography.* Nat. Photon., 2009. **3**: p. 503-509

4.	Zhang, H.F., et al., *Functional photoacoustic microscopy for high-resolution and noninvasive in vivo imaging.* Nat. Biotechnol., 2006. **24**(7): p. 848-51.

5.	Yao, J., et al., *In vivo photoacoustic imaging of transverse blood flow by using Doppler broadening of bandwidth.* Opt. Lett., 2010. **35**(9): p. 1419-1421.

6.	Yao, J., et al., *Label-free oxygen-metabolic photoacoustic microscopy in vivo.* Journal of biomedical optics, 2011. **16**(7): p. 076003-076003-11.

7.	Wang, L., K. Maslov, and L.V. Wang, *Single-cell label-free photoacoustic flowoxigraphy in vivo.* Proceedings of the National Academy of Sciences, 2013. **110**(15): p. 5759-5764.

8.	Maslov, K., et al., *Optical-resolution photoacoustic microscopy for in vivo imaging of single capillaries.* Opt. Lett., 2008. **33**(9): p. 929-31.

9.	Maslov, K., G. Stoica, and L.V. Wang, *In vivo dark-field reflection-mode photoacoustic microscopy.* Opt. Lett., 2005. **30**(6): p. 625-7.

10.	Wang, X., et al., *Noninvasive laser-induced photoacoustic tomography for structural and functional in vivo imaging of the brain.* Nat. Biotechnol., 2003. **21**(7): p. 803-6.

11.	Li, C., et al., *Real-time photoacoustic tomography of cortical hemodynamics in small animals.* J. Biomed. Opt., 2010. **15**(1): p. 010509.

12.	Erpelding, T.N., et al., *Sentinel lymph nodes in the rat: noninvasive photoacoustic and US imaging with a clinical US system.* Radiology, 2010. **256**(1): p. 102-10.

13.	Yao, D.-K., et al., *In vivo label-free photoacoustic microscopy of cell nuclei by excitation of DNA and RNA.* Optics Letters, 2010. **35**(24): p. 4139-4141.

14.	Wang, H.-W., et al., *Label-Free Bond-Selective Imaging by Listening to Vibrationally Excited Molecules.* Physical Review Letters, 2011. **106**(23): p. 238106.

15.	Xu, Z., C. Li, and L.V. Wang, *Photoacoustic tomography of water in phantoms and tissue.* J. Biomed. Opt., 2010. **15**(3): p. 036019.

16.   Razansky, D., et al., *Multispectral opto-acoustic tomography of deep-seated fluorescent proteins in vivo.* Nat. Photon., 2009. **3**: p. 412-417.

17.   Wang, Y., J. Xia, and L.V. Wang, *Deep-tissue photoacoustic tomography of Förster resonance energy transfer.* Journal of biomedical optics, 2013. **18**(10): p. 101316-101316.

18.   Zhang, C., K. Maslov, and L.V. Wang, *Subwavelength-resolution label-free photoacoustic microscopy of optical absorption in vivo.* Opt. Lett., 2010. **35**(19): p. 3195-3197.

19.   Zhang, C., et al., *Reflection-mode submicron-resolution in vivo photoacoustic microscopy.* Journal of Biomedical Optics, 2012. **17**(2): p. 020501-1.

20.   Zhang, C., et al., *In vivo photoacoustic microscopy with 7.6-μm axial resolution using a commercial 125-MHz ultrasonic transducer.* Journal of Biomedical Optics, 2012. **17**(11): p. 116016-116016.

21.   Zhang, C., et al., *Slow-sound photoacoustic microscopy.* Applied Physics Letters, 2013. **102**(16): p. 163702.

22.   Gao, L., et al., *Intracellular temperature mapping with fluorescence-assisted photoacoustic-thermometry.* Applied Physics Letters, 2013. **102**(19): p. 193705-193705-5.

23.   Gray-Schopfer, V., C. Wellbrock, and R. Marais, *Melanoma biology and new targeted therapy.* Nature, 2007. **445**(7130): p. 851-857.

24.   McDonald, D.M. and P.L. Choyke, *Imaging of angiogenesis: from microscope to clinic.* Nat. Med., 2003. **9**(6): p. 713-25.

25.   Wang, L.V. and H. Wu, *Biomedical Optics: Principles and Imaging.* 2007, Hoboken, NJ: Wiley.

26.   Kietzmann, M., D. Lubach, and H.-J. Heeren, *The mouse epidermis as a model in skin pharmacology: influence of age and sex on epidermal metabolic reactions and their circadian rhythms.* Laboratory Animals, 1990. **24**(4): p. 321-327.

27.   Verkruysse, W., et al., *Remittance at a single wavelength of 390nm to quantify epidermal melanin concentration.* Journal of biomedical optics, 2009. **14**(1): p. 014005-014005-4.

28.   Li, L., et al., *Photoacoustic imaging of lacZ gene expression in vivo.* J. Biomed. Opt., 2007. **12**(2): p. 020504.

29.   Song, K.H., et al., *Noninvasive photoacoustic identification of sentinel lymph nodes containing methylene blue in vivo in a rat model.* J. Biomed. Opt., 2008. **13**(5): p. 054033.

30.   Hu, S., K. Maslov, and L.V. Wang, *Second-generation optical-resolution photoacoustic microscopy with improved sensitivity and speed.* Optics letters, 2011. **36**(7): p. 1134-1136.

31.   Rao, B., et al., *Hybrid-scanning optical-resolution photoacoustic microscopy for in vivo vasculature imaging.* Opt. Lett., 2010. **35**(10): p. 1521-3.

32.   Shelton, R.L. and B.E. Applegate, *Off-axis photoacoustic microscopy.* Biomedical Engineering, IEEE Transactions on, 2010. **57**(8): p. 1835-1838.

33.   Ku, G., et al., *Photoacoustic microscopy with 2-μm transverse resolution.* Journal of biomedical optics, 2010. **15**(2): p. 021302-021302-5.

34.   Jensen, J.A., et al., *Deconvolution of in-vivo ultrasound B-mode images.* Ultrasonic Imaging, 1993. **15**(2): p. 122-133.

35.   Wang, L., et al., *Fast voice-coil scanning optical-resolution photoacoustic microscopy.* Opt. Lett., 2011. **36**(2): p. 139-141.

36.   Wang, Y., et al., *Integrated photoacoustic and fluorescence confocal microscopy.* IEEE Trans. Biomed. Eng., 2010. **57**(10): p. 2576-8.

37.   Xie, Z., et al., *Pure optical photoacoustic microscopy.* Optics express, 2011. **19**(10): p. 9027.

38.   Zhang, E.Z., et al., *Multimodal photoacoustic and optical coherence tomography scanner using an all optical detection scheme for 3D morphological skin imaging.* Biomedical optics express, 2011. **2**(8): p. 2202-2215.

39.   Pawley, J.B., *Handbook of biological confocal microscopy.* 1995: Springer.

40.   Federman, J. and H.D. Schubert, *Complications associated with the use of silicone oil in 150 eyes after retina-vitreous surgery.* Ophthalmology, 1988. **95**(7): p. 870-876.

41.   Tognetto, D., et al., *Anatomical and functional outcomes after heavy silicone oil tamponade in vitreoretinal surgery for complicated retinal detachment: a pilot study.* Ophthalmology, 2005. **112**(9): p. 1574. e1-1574. e8.

42.   Rohrich, R.J. and J.K. Potter, *Liquid Injectable Silicone:: Is There a Role as a Cosmetic Soft-Tissue Filler?* Plastic and reconstructive surgery, 2004. **113**(4): p. 1239-1241.

43.   Chasan, P.E., *The history of injectable silicone fluids for soft-tissue augmentation.* Plastic and reconstructive surgery, 2007. **120**(7): p. 2034-2040.

44.   Insana, M.F. and L.T. Cook, *Bioelasticity imaging: System design.* Proc. IEEE, 1999. **3659**: p. 224-235.

45.   Yao, J., et al., *Double-illumination photoacoustic microscopy.* Optics Letters, 2012. **37**(4): p. 659-661.

46.   Wells, P.N.T., *Biomedical ultrasonics.* Vol. 20. 1977: Academic Press London.

47.   Danielli, A., et al., *Picosecond absorption relaxation measured with nanosecond laser photoacoustics.* Appl. Phys. Lett., 2010. **97**(16): p. 163701.

48.   Liu, Y., C. Zhang, and L.V. Wang, *Effects of light scattering on optical-resolution photoacoustic microscopy.* Journal of Biomedical Optics, 2012. **17**(12): p. 126014-126014.

49. Phoong, S.-M. and P. Vaidyanathan, *Time-varying filters and filter banks: some basic principles.* Signal Processing, IEEE Transactions on, 1996. **44**(12): p. 2971-2987.

50. Wang, G., *The most general time-varying filter bank and time-varying lapped transforms.* Signal Processing, IEEE Transactions on, 2006. **54**(10): p. 3775-3789.

51. Yamaoka, Y., M. Nambu, and T. Takamatsu, *Fine depth resolution of two-photon absorption-induced photoacoustic microscopy using low-frequency bandpass filtering.* Opt. Express, 2011. **19**(14): p. 13365-13377.

52. Bahat, A., et al., *Thermotaxis of mammalian sperm cells: A potential navigation mechanism in the female genital tract.* Nature Medicine, 2003. **9**(2): p. 149-150.

53. Lowell, B.B. and B.M. Spiegelman, *Towards a molecular understanding of adaptive thermogenesis.* Nature, 2000. **404**(6778): p. 652-660.

54. Kamei, Y., et al., *Infrared laser-mediated gene induction in targeted single cells in vivo.* Nature Methods, 2009. **6**(1): p. 79-81.

55. Suzuki, M., et al., *Microscopic detection of thermogenesis in a single HeLa cell.* Biophysical Journal, 2007. **92**(6): p. L46-L48.

56. Wang, C.L., et al., *Determining intracellular temperature at single-cell level by a novel thermocouple method.* Cell Research, 2011. **21**(10): p. 1517-1519.

57. Vetrone, F., et al., *Temperature Sensing Using Fluorescent Nanothermometers.* Acs Nano, 2010. **4**(6): p. 3254-3258.

58. Gota, C., et al., *Hydrophilic Fluorescent Nanogel Thermometer for Intracellular Thermometry.* Journal of the American Chemical Society, 2009. **131**(8): p. 2766-2767.

59. Gao, L., et al., *Single-cell photoacoustic thermometry.* Journal of Biomedical Optics, 2013. **18**(2): p. 026003-026003.

60. Okabe, K., et al., *Intracellular temperature mapping with a fluorescent polymeric thermometer and fluorescence lifetime imaging microscopy.* Nat Commun, 2012. **3**: p. 705.

61. Donner, J.S., et al., *Mapping Intracellular Temperature Using Green Fluorescent Protein.* Nano Letters, 2012. **12**(4): p. 2107-2111.

62. Johnson, I. and M.T.Z. Spence, *Molecular Probes Handbook, A Guide to Fluorescent Probes and Labeling Technologies.* 2011: Invitrogen

63. Lakowicz, J.R., *Principles of fluorescence spectroscopy.* 3rd ed. 2006, New York: Springer. xxvi, 954 p.

64. Wang, Y. and L.V. Wang, *Förster resonance energy transfer photoacoustic microscopy.* Journal of Biomedical Optics, 2012. **17**(8): p. 086007-086007.

65. Wang, L.V. and H.-i. Wu, *Biomedical optics : principles and imaging*. 2007, Hoboken, N.J.: Wiley-Interscience. xiv, 362 p.

66. Larina, I.V., K.V. Larin, and R.O. Esenaliev, *Real-time optoacoustic monitoring of temperature in tissues.* Journal of Physics D-Applied Physics, 2005. **38**(15): p. 2633-2639.

67. Ali, M.A., J. Moghaddasi, and S.A. Ahmed, *Examination of Temperature Effects on the Lasing Characteristics of Rhodamine Cw Dye-Lasers.* Applied Optics, 1990. **29**(27): p. 3945-3949.

68. Drexhage, K.H., *Structure and Properties of Laser-Dyes.* Topics in Applied Physics, 1990. **1**: p. 155-200.

69. Ke, H., et al., *Photoacoustic and thermoacoustic tomography of dog prostates*, A.A. Oraevsky and L.V. Wang, Editors. 2011, SPIE: San Francisco, California, USA. p. 789938-6.

70. Peterson, M.E., et al., *The dependence of enzyme activity on temperature: determination and validation of parameters.* Biochemical Journal, 2007. **402**: p. 331-337.

71. Beney, L. and P. Gervais, *Influence of the fluidity of the membrane on the response of microorganisms to environmental stresses.* Applied Microbiology and Biotechnology, 2001. **57**(1-2): p. 34-42.

72. Cesare, P., et al., *Ion channels gated by heat.* Proceedings of the National Academy of Sciences of the United States of America, 1999. **96**(14): p. 7658-7663.

73. Zhang, C., et al., *Label-free photoacoustic microscopy of cytochromes.* Journal of Biomedical Optics, 2013. **18**(2): p. 020504-020504.

74. Zhang, C., et al., *Label-free photoacoustic microscopy of myocardial sheet architecture.* Journal of Biomedical Optics, 2012. **17**(6): p. 060506-1.

75. Zhou, Y., et al., *Photoacoustic microscopy of bilirubin in tissue phantoms.* Journal of Biomedical Optics, 2012. **17**(12): p. 126019-126019.

76. Matthews, T.P., et al., *Label-free photoacoustic microscopy of peripheral nerves.* Journal of biomedical optics, 2014. **19**(1): p. 016004-016004.

77. Thorell, B. and B. Chance, *Microspectrography of respiratory enzymes within the single, mammalian cell under different metabolic conditions.* Experimental Cell Research, 1960. **20**(1): p. 43-55.

78. Brusnichkin, A.V., et al., *Ultrasensitive label-free photothermal imaging, spectral identification, and quantification of cytochrome c in mitochondria, live cells, and solutions.* Journal of biophotonics, 2010. **3**(12): p. 791-806.

79. Lasne, D., et al., *Label-free optical imaging of mitochondria in live cells.* Opt. Express, 2007. **15**(21): p. 14184-14193.

80. Laufer, J., et al., *Quantitative spatially resolved measurement of tissue chromophore concentrations using photoacoustic spectroscopy: application to the measurement of blood oxygenation and haemoglobin concentration.* Phys. Med. Biol., 2007. **52**(1): p. 141-68.

81. Cipolat, S., et al., *Mitochondrial Rhomboid PARL Regulates Cytochrome c Release during Apoptosis via OPA1-Dependent Cristae Remodeling.* Cell, 2006. **126**(1): p. 163-175.

82. Scorrano, L., et al., *Chloromethyltetramethylrosamine (Mitotracker OrangeTM) Induces the Mitochondrial Permeability Transition and Inhibits Respiratory Complex I IMPLICATIONS FOR THE MECHANISM OF CYTOCHROME cRELEASE.* Journal of Biological Chemistry, 1999. **274**(35): p. 24657-24663.

83. Liao, G.-L. and G. Palmer, *The reduced minus oxidized difference spectra of cytochromes a and a3.* Biochimica et Biophysica Acta (BBA)-Bioenergetics, 1996. **1274**(3): p. 109-111.

84. Capaldi, R.A., M.F. Marusich, and J.-W. Taanman, *Mammalian cytochrome-c oxidase: characterization of enzyme and immunological detection of subunits in tissue extracts and whole cells.* Method Enzymol, 1995. **260**: p. 117-132.

85. Costa, K.D., et al., *Laminar fiber architecture and three-dimensional systolic mechanics in canine ventricular myocardium.* American Journal of Physiology-Heart and Circulatory Physiology, 1999. **276**(2): p. H595-H607.

86. Pope, A.J., et al., *Three-dimensional transmural organization of perimysial collagen in the heart.* American Journal of Physiology-Heart and Circulatory Physiology, 2008. **295**(3): p. H1243-H1252.

87. LeGrice, I.J., et al., *Laminar structure of the heart: ventricular myocyte arrangement and connective tissue architecture in the dog.* American Journal of Physiology-Heart and Circulatory Physiology, 1995. **269**(2): p. H571-H582.

88. Chen, J., et al., *Regional ventricular wall thickening reflects changes in cardiac fiber and sheet structure during contraction: quantification with diffusion tensor MRI.* American Journal of Physiology-Heart and Circulatory Physiology, 2005. **289**(5): p. H1898-H1907.

89. LeGrice, I., Y. Takayama, and J. Covell, *Transverse shear along myocardial cleavage planes provides a mechanism for normal systolic wall thickening.* Circulation Research, 1995. **77**(1): p. 182-193.

90. Gilbert, S.H., et al., *Regional localisation of left ventricular sheet structure: integration with current models of cardiac fibre, sheet and band structure.* European journal of cardio-thoracic surgery, 2007. **32**(2): p. 231-249.

91. Scollan, D.F., et al., *Histological validation of myocardial microstructure obtained from diffusion tensor magnetic resonance imaging.* American Journal of Physiology-Heart and Circulatory Physiology, 1998. **275**(6): p. H2308-H2318.

92.   Arai, A.E., et al., *Myocardial oxygenation in vivo: optical spectroscopy of cytoplasmic myoglobin and mitochondrial cytochromes.* American Journal of Physiology-Heart and Circulatory Physiology, 1999. **277**(2): p. H683-H697.

93.   Dolley, D.H. and F.V. Guthrie, *The pigmentation of heart muscle.* The Journal of medical research, 1921. **42**(3): p. 289.

94.   Majno, G. and I. Joris, *Cells, tissues, and disease: principles of general pathology.* 2004: Oxford University Press New York:.

95.   Anthony, C., *Cytochrome c and the oxidation of C1 compounds in Pseudomonas AM1.* Biochemical Journal, 1970. **119**(5): p. 54P.

96.   Rao, B., et al., *Real-time four-dimensional optical-resolution photoacoustic microscopy with Au nanoparticle-assisted subdiffraction-limit resolution.* Optics Letters, 2011. **36**(7): p. 1137-1139.

97.   Lein, E.S., et al., *Genome-wide atlas of gene expression in the adult mouse brain.* Nature, 2007. **445**(7124): p. 168-176.

98.   Li, A., et al., *Micro-Optical Sectioning Tomography to Obtain a High-Resolution Atlas of the Mouse Brain.* Science, 2010. **330**(6009): p. 1404-1408.

99.   Ragan, T., et al., *Serial two-photon tomography for automated ex vivo mouse brain imaging.* Nat Meth, 2012. **9**(3): p. 255-258.

100.   Amunts, K., et al., *BigBrain: An Ultrahigh-Resolution 3D Human Brain Model.* Science, 2013. **340**(6139): p. 1472-1475.

101.   Hama, H., et al., *Scale: a chemical approach for fluorescence imaging and reconstruction of transparent mouse brain.* Nat Neurosci, 2011. **14**(11): p. 1481-1488.

102.   Chung, K., et al., *Structural and molecular interrogation of intact biological systems.* Nature, 2013. **497**(7449): p. 332-337.

103.   Lorenz, C., et al., *A multi-scale line filter with automatic scale selection based on the Hessian matrix for medical image segmentation*, in *Scale-Space Theory in Computer Vision*, B. Haar Romeny, et al., Editors. 1997, Springer Berlin Heidelberg. p. 152-163.

104.   Zink, D., A.H. Fischer, and J.A. Nickerson, *Nuclear structure in cancer cells.* Nat Rev Cancer, 2004. **4**: p. 677-687.

105.   Nedosekin, D.A., et al., *Ultra-fast photoacoustic flow cytometry with a 0.5 MHz pulse repetition rate nanosecond laser.* Optics Express, 2010. **18**(8): p. 8605-8620.

106.   Song, L., K. Maslov, and L.V. Wang, *Multifocal optical-resolution photoacoustic microscopy in vivo.* Optics Letters, 2011. **36**(7): p. 1236-1238.

107. Yao, J., et al., *Photoimprint Photoacoustic Microscopy for Three-Dimensional Label-Free Subdiffraction Imaging.* Physical Review Letters, 2014. **112**(1): p. 014302.

108. Shelton, R.L., S.P. Mattison, and B.E. Applegate, *Volumetric imaging of erythrocytes using label‐free multiphoton photoacoustic microscopy.* Journal of biophotonics, 2013.

109. Zhang, C., C. Li, and L.V. Wang, *Fast and Robust Deconvolution-Based Image Reconstruction for Photoacoustic Tomography in Circular Geometry: Experimental Validation.* Photonics Journal, IEEE, 2010. **2**(1): p. 57-66.

110. Zhang, C. and Y. Wang, *Deconvolution reconstruction of full-view and limited-view photoacoustic tomography: a simulation study.* J. Opt. Soc. Am. A, 2008. **25**(10): p. 2436-2443.

111. Nasiriavanaki, M., et al., *High-resolution photoacoustic tomography of resting-state functional connectivity in the mouse brain.* Proceedings of the National Academy of Sciences, 2014. **111**(1): p. 21-26.

112. Niederhauser, J.J., et al., *Combined ultrasound and optoacoustic system for real-time high-contrast vascular imaging in vivo.* IEEE Trans. Med. Imaging, 2005. **24**(4): p. 436-40.

113. Kolkman, R.G., et al., *Real-time in vivo photoacoustic and ultrasound imaging.* J. Biomed. Opt., 2008. **13**(5): p. 050510.

114. Xu, Y., D. Feng, and L.V. Wang, *Exact frequency-domain reconstruction for thermoacoustic tomography. I. Planar geometry.* Medical Imaging, IEEE Transactions on, 2002. **21**(7): p. 823-828.

115. Köstli, K.P. and P.C. Beard, *Two-dimensional photoacoustic imaging by use of Fourier-transform image reconstruction and a detector with an anisotropic response.* Applied optics, 2003. **42**(10): p. 1899-1908.

116. Xu, M. and L.V. Wang, *Universal back-projection algorithm for photoacoustic computed tomography.* Phys. Rev. E, 2005. **71**(1 Pt 2): p. 016706.

117. Hoelen, C.G. and F.F. de Mul, *Image reconstruction for photoacoustic scanning of tissue structures.* Applied Optics, 2000. **39**(31): p. 5872-5883.

118. Gamelin, J., et al., *A real-time photoacoustic tomography system for small animals.* Opt. Express, 2009. **17**(13): p. 10489-98.

119. Provost, J. and F. Lesage, *The application of compressed sensing for photo-acoustic tomography.* Medical Imaging, IEEE Transactions on, 2009. **28**(4): p. 585-594.

120. Riad, S.M., *The deconvolution problem: an overview.* Proceedings of the IEEE, 1986. **74**(1): p. 82-85.

121. Kruger, R.A., P. Liu, and C.R. Appledorn, *Photoacoustic ultrasound (PAUS)—reconstruction tomography.* Medical physics, 1995. **22**: p. 1605.

122.   Xu, Y., M. Xu, and L.V. Wang, *Exact frequency-domain reconstruction for thermoacoustic tomography. II. Cylindrical geometry*. Medical Imaging, IEEE Transactions on, 2002. **21**(7): p. 829-833.

Vita

Chi Zhang

Degrees	Ph.D., Biomedical Engineering Washington University in St. Louis May 2014

Degrees

Ph.D., Biomedical Engineering
Washington University in St. Louis
May 2014

M.S., Electrical Engineering
Fudan University
June 2009

B.S., Electrical Engineering
Fudan University
June 2006

**Professional
Societies**

The International Society for Optics and Photonics (SPIE)

Publications

D. Yao, **C. Zhang**, K. Maslov, and L. V. Wang, "Photoacoustic measurement of the Gruneisen parameter of tissue," *Journal of Biomedical Optics* 19, 017007, 2014.

[T. P. Matthews, **C. Zhang**], and L. V. Wang, "Label-free photoacoustic microscopy of peripheral nerves," *Journal of Biomedical Optics* 19, 016004, 2014.

([ ] denotes equal contribution.)

J. Yao, L. Wang, C. Li, **C. Zhang**, and L. V. Wang, "Photoimprint photoacoustic microscopy for three-dimensional label-free subdiffraction imaging," *Physical Review Letters* 112, 014302, 2014.

[C. Li, **C. Zhang**, L. Gao], A. Garcia-Uribe, and L. V. Wang, "Photoacoustic recovery after photothermal bleaching in living cells," *Journal of Biomedical Optics* 18, 106004, 2013.

91

[L. Gao, **C. Zhang**, C. Li], and L. V. Wang, "Intracellular temperature mapping with fluorescence-assisted photoacoustic-thermometry," *Applied Physics Letters* 102, 193705, 2013.

[**C. Zhang**, Y. Zhou], C. Li, and L. V. Wang, "Slow-sound photoacoustic microscopy," *Applied Physics Letters* 102, 163702, 2013.

Y. Zhang, Y. Wang, L. Wang, Y. Wang, X. Cai, **C. Zhang**, L. V. Wang, and Y. Xia, "Labeling human mesenchymal stem cells with Au nanocages for *in vitro* and *in vivo* tracking by two-photon microscopy and photoacoustic microscopy," *Theranostics* 3, 532–543, 2013.

L. Gao, L. Wang, C. Li, Y. Liu, H. Ke, **C. Zhang**, L. V. Wang, "Single-cell photoacoustic thermometry," *Journal of Biomedical Optics* 18, 026003, 2013.

C. Zhang, Y. S. Zhang, D.-K. Yao, Y. Xia, and L. V. Wang, "Label-free photoacoustic microscopy of cytochromes," *Journal of Biomedical Optics* 18, 020504, 2013.

[Y. Zhou, **C. Zhang**], D.-K. Yao, and L. V. Wang, "Photoacoustic microscopy of bilirubin in tissue phantoms," *Journal of Biomedical Optics* 17, 126019, 2012.

Y. Liu, **C. Zhang**, and L. V. Wang, "Effects of light scattering on optical-resolution photoacoustic microscopy," *Journal of Biomedical Optics* 17, 126014, 2012.

C. Zhang, K. Maslov, J. Yao, and L. V. Wang, "*In vivo* photoacoustic microscopy with 7.6-μm axial resolution using a commercial 125-MHz ultrasonic transducer," *Journal of Biomedical Optics* 17, 116016, 2012.

X. Cai, L. Li, A. Krumholz, Z. Guo, T. N. Erpelding, **C. Zhang**, Y. Zhang, Y. Xia, and L. V. Wang, "Multi-scale molecular photoacoustic tomography of gene expression," *PLoS ONE* 7, e43999, 2012.

C. Zhang, Y.-J. Cheng, J. Chen, S. Wickline, and L. V. Wang, "Label-free photoacoustic microscopy of myocardial sheet architecture," *Journal of Biomedical Optics* 17, 060506, 2012.

C. Zhang, K. Maslov, S. Hu, R. Chen, Q. Zhou, K. K. Shung, and L. V. Wang, "Reflection-mode submicron-resolution *in vivo* photoacoustic microscopy," *Journal of Biomedical Optics* 17, 020501, 2012.

Y. Zhang, X. Cai, Y. Wang, **C. Zhang**, L. Li, S.-W. Choi, L. V. Wang and Y. Xia, "Noninvasive photoacoustic microscopy of living cells in two and three

dimensions through enhancement by a metabolite dye," *Angewandte Chemie International Edition* 50, 7359–7363, 2011.

C. Zhang, K. Maslov and L. V. Wang, "Subwavelength-resolution label-free photoacoustic microscopy of optical absorption *in vivo*," *Optics Letters* 35, 3195–3197, 2010.

C. Zhang, C. Li and L. V. Wang, "Fast and robust deconvolution-based image reconstruction for photoacoustic tomography in circular geometry: experimental validation," *IEEE Photonics Journal* 2, 57–66, 2010.

C. Zhang and Y. Wang, "Deconvolution reconstruction of full-view and limited-view photoacoustic tomography: a simulation study," *Journal of the Optical Society of America A* 25, 2436–2443, 2008.

C. Zhang and Y. Wang, "A reconstruction algorithm for thermoacoustic tomography with compensation for acoustic speed heterogeneity," *Physics in Medicine and Biology* 53, 4971–4982, 2008.

May 2014